AZAPROPAZONE

AND

DERIVATIZED EDTA AND DTPA COMPLEXES

AS MRI CONTRAST AGENTS

By

THERESA K. FAUCONNIER, B.Sc.

A Thesis

Submitted to the School of Graduate Studies

in Partial Fulfilment of the Requirements

for the Degree

Doctor of Philosophy

McMaster University

AZAPROPAZONE AND MRI CONTRAST AGENTS

To My Parents

AND

To the Memory of

Colin James Lyne Lock

DOCTOR OF PHILOSOPHY (1996)

(Chemistry)

McMASTER UNIVERSITY

Hamilton, Ontario

TITLE: AZAPROPAZONE AND DERIVATIZED EDTA AND
           DTPA COMPLEXES AS MRI CONTRAST AGENTS

AUTHOR: Theresa K. Fauconnier, B.Sc. (Lakehead University)

SUPERVISOR: Professor Colin James Lyne Lock

NUMBER OF PAGES: xx, 181

Abstract

Azapropazone is a non-steroidal anti-inflammatory drug (NSAID), that had not been structurally characterized before this work began. The X-ray crystal structure of azapropazone is presented here. The synthesis of several derivatives of azapropazone is outlined. The X-ray crystal structures of the derivatives are presented and described and compared to the structure of azapropazone. The discrepancies in the literature on the previously proposed structures of azapropazone and its derivatives are also discussed.

Contrast agents for MRI are necessary for site-specific image enhancement. Potential new agents are presented in this work. The synthesis and characterization of amino acid derivatives of ethylenediaminetetracetic acid (EDTA) and diethylenetriaminepentaacetic acid (DTPA) is described. The amino acids used are the benzyl esters of glycine, phenylalanine, and tyrosine. The relaxivities of the ligands with Gd(III) were determined and compared to the relaxivities of similar complexes in the current literature.

The synthesis and characterization of azapropazone derivatives of EDTA and DTPA is described. The possibility of inflammation-site imaging is discussed. The relaxivities of these ligands with Gd(III) was determined and compared to the relaxivities of similar complexes in the current literature.

The results of biodistribution studies and single photon emitted computed tomography (SPECT) images of rats injected with the glycine or azapropazone DTPA derivative complexed with ^{111}In(III) are described.

Acknowledgements

I wish to express my gratitude to the following people for their contributions to this work, and my time at McMaster University:

Professor Colin J.L. Lock for his guidance and supervision. He passed away before I started to write this thesis, but his enthusiastic presence was felt in every word. He shared his enjoyment of chemistry with us, and his enjoyment of writing about chemistry. Outside of the lab, he invited his research group to any "conviviality" that he could. He told off-colour jokes well, and loudly. He had many friends. He will be remembered long after this thesis is forgotten.

Professors Russell A. Bell, Alex D. Bain, and Lijuan Li, the members of my supervisory committee, for their helpful advice and suggestions. Dr. Bell and Dr. Bain contributed much time and knowledge to my project, and helped to keep it moving forward. A special thanks to Lijuan for joining my committee at the last minute.

Dr. Alan Guest for his friendship, helpful advice, and leadership in the lab. An extra special thanks for proof-reading my thesis so quickly and so well.

Dr. Jim F. Britten for teaching me everything I know about X-ray crystallography. He is a knowledgeable, and very patient, teacher. Thanks also to

Table of Contents

List of Tables

List of Figures

List of Abbreviations and Symbols

β	Bohr magneton
γ	magnetogyric ratio
η	viscosity of medium
λ	wavelength
μL	microlitre(s)
τ_c	correlation time
τ_D	relative translational diffusion time
τ_e	correlation time
τ_M	residence lifetime of bound water
τ_R	rotational tumbling time of the metal-water unit
AA	arachidonic acid
ACQ	acquire
AZAP	azapropazone
B_o	magnetic field
C	celsius
CA	collision activation
CCD	charge coupled device
CH_3OH	methanol

CI	chemical ionization
cm^{-1}	wavenumber(s)
COSY	correlation spectroscopy
COX	cyclooxygenase
CSF	cerebral spinal fluid
d	day
DDW	distilled/deionized water
D_m	measured density
DMF	dimethylformamide
DMSO	dimethylsulfoxide
DSS	2,2-dimethyl-2-silapentane-5-sulfonate
DTPA	diethylenediaminepentaacetic acid
D_x	calculated density
EDTA	ethylenediaminetetraacetic acid
EI	electron impact
ESMS	electrospray mass spectrometry
eV	electron volt
FID	free induction decay
f_{Larmor}	Larmor resonance frequency
g	electronic g-factor
GB	glycine benzyl ester
h	hour

HMBC	heteronuclear multiple bond correlation
HSQC	heteronuclear single quantum correlation
Hz	Hertz
m/z	mass to charge ratio
mp	melting point
Mr	formula weight
MRI	magnetic resonance imaging
$N_{avog.}$	Avogadro's number
NMR	nuclear magnetic resonance
NOE	nuclear Overhauser effect
NSAID	non-steroidal anti-inflammatory drug
PB	phenylalanine benzyl ester
PG	prostaglandin
PM	mole fraction of metal ion
ppm	parts per million
q	number of water molecules bound per metal ion
r	proton-metal ion distance
R_1	relaxivity based on T_1
RF	radiofrequency
s	second
S	total electron spin
SPECT	single photon emission computed tomography
T	Tesla

T_1	spin-lattice or longitudinal relaxation time
T_{1e}	longitudinal electron spin relaxation time
T_{1M}	relaxation rate of protons of water molecules coordinated to metal
T_2	spin-spin or transverse relaxation time
TB	tyrosine benzyl ester
TMS	tetramethylsilane
Z	number of formula units per cell
Å	angstrom(s)
°	degree

Chapter 1

Introduction

A pharmaceutical on the market today represents a decade or more of toxicity evaluations and clinical trials. And yet, there are still drugs in therapeutic use that are not fully characterized or purified. Caldwell estimates that a quarter of all therapeutic agents are marketed and administered to humans as mixtures of isomeric substances,[1] even though the pharmacologically less active isomer may well contribute to the adverse effects of the drugs.[2] It is the job of the chemist to determine the correct structures of drugs, their purity, their chirality, and whether or not they are administered as mixtures.

The determination of a drug's structure is invaluable for its characterization, but it can also be used to investigate the action of the drug at the molecular level. The increasing developments in structural biology and computational chemistry have helped to determine what a drug molecule recognizes as a receptor in the body. Further, crystallographic structure data are used to look at the interaction of drugs and their molecular targets in three dimensions. The fundamental insights into drug structure and molecular recognition are increasingly becoming available for exploitation in drug design.

The chemist has taken pharmaceutical characterization and design one step

further in an effort to produce site-specific imaging agents. The theory is that a drug or a biomolecule can be used as a diagnostic tool by interacting with certain receptors in the body. The molecule is derivatized with a chelating moiety which will bind either a paramagnetic metal in the case of magnetic resonance imaging, or a radioactive metal in the case of radioimaging.

The following work is an example of how spectroscopic and single crystal X-ray diffraction techniques can characterize a known pharmaceutical, and aid in evaluating new ones. In this chapter the objectives of this thesis are introduced, and some general background material concerning each of the projects is presented. The more detailed information, specific for each project, can be found at the beginning of the relevant chapter.

1.1 Research Objectives

The research presented here had two major objectives. The first was to investigate the structure of azapropazone, a non-steroidal anti-inflammatory drug (NSAID). Some controversy existed in the literature about the nature of the drug, and the technique of single crystal X-ray diffractometry was used to solve the problem. Various derivatives of azapropazone were also synthesized, and their structures analyzed. In addition, variable temperature ^{1}H NMR was used to determine and compare the energy barriers of the dimethylamino group rotation for azapropazone and a derivative.

The second objective was to synthesize some ethylenediaminetetraacetic acid (EDTA) and diethylenetriaminepentaacetic acid (DTPA) amino acid derivative complexes of paramagnetic gadolinium and evaluate them as potential contrast

agents for magnetic resonance imaging (MRI). The metal complexes were designed to be stable, neutral, and slightly lipophilic, so that they may cross the blood-brain barrier, or be used to image the hepatobiliary route. The change in longitudinal proton relaxation enhancement per mole of the metal complex, or the relaxivity (R_1), was evaluated by measuring the T_1 relaxation time of each complex.

The two research paths converged with the study of EDTA and DTPA azapropazone derivative complexes with gadolinium as potential contrast agents for inflammation site MR imaging. A derivative of azapropazone presented in this thesis was complexed with both EDTA and DTPA, and the relaxivity was measured for each of the ligands with Gd(III).

Finally, in an effort to evaluate the biodistribution of the ligands when complexed to a tripositive metal, animal tests were performed for some of the ligands with ^{111}In(III). The location of the complex *in vivo* was determined by counting the gamma rays of specific isolated organs of the animals, and by single photon emission computed tomography (SPECT) imaging.

1.2 Azapropazone

Azapropazone is one of many drugs that is prescribed to patients even though its structure is not clearly known. In fact, the determination of the X-ray crystal structure of azapropazone, as presented in this work (*vide infra*), showed that the previously proposed structure of the drug was wrong. The wrong structure is shown below as it appears in the Merck Index.[3] Incorrect structure determination is also true with some azapropazone derivatives. The solution of the correct structures of these molecules is the first step in learning more about the drug's

interactions with the human body.

The incomplete knowledge available about azapropazone has not prevented it from gaining some popularity, especially with rheumatoid arthritis patients. It is used commercially in most countries of
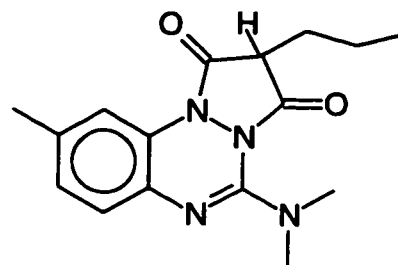
Azapropazone
(as seen in the Merck Index)

Europe, and parts of Asia, Africa, and South America, but has not yet been approved for use in North America. This is, in part, because of studies that showed that the drug can be toxic to the gastrointestinal (GI) tract in purebred dogs.[4] When the gastric tolerance of the drug was tested in rats, however, azapropazone showed less gastric toxicity than most other NSAIDs.[5] This is a significant result because the pharmacokinetics of azapropazone in humans has been shown to be more similar to that of rats than dogs.[6,7]

The lower gastric toxicity implies a relatively unique mode of action for azapropazone compared with some other NSAIDs which give patients stomach ulcers. The possibility that NSAIDs with fewer side effects may be designed has spurred an intense investigation into the target sites of NSAIDS. The search has led to two enzymes, called COX-1 and COX-2.

Mode of Action: COX-1 or COX-2

The process by which NSAIDs reduce inflammation is currently a subject of interest to pharmaceutical companies. Inflammation is the process of response to tissue injury, regardless of cause, and is precursory in tissue healing. The system
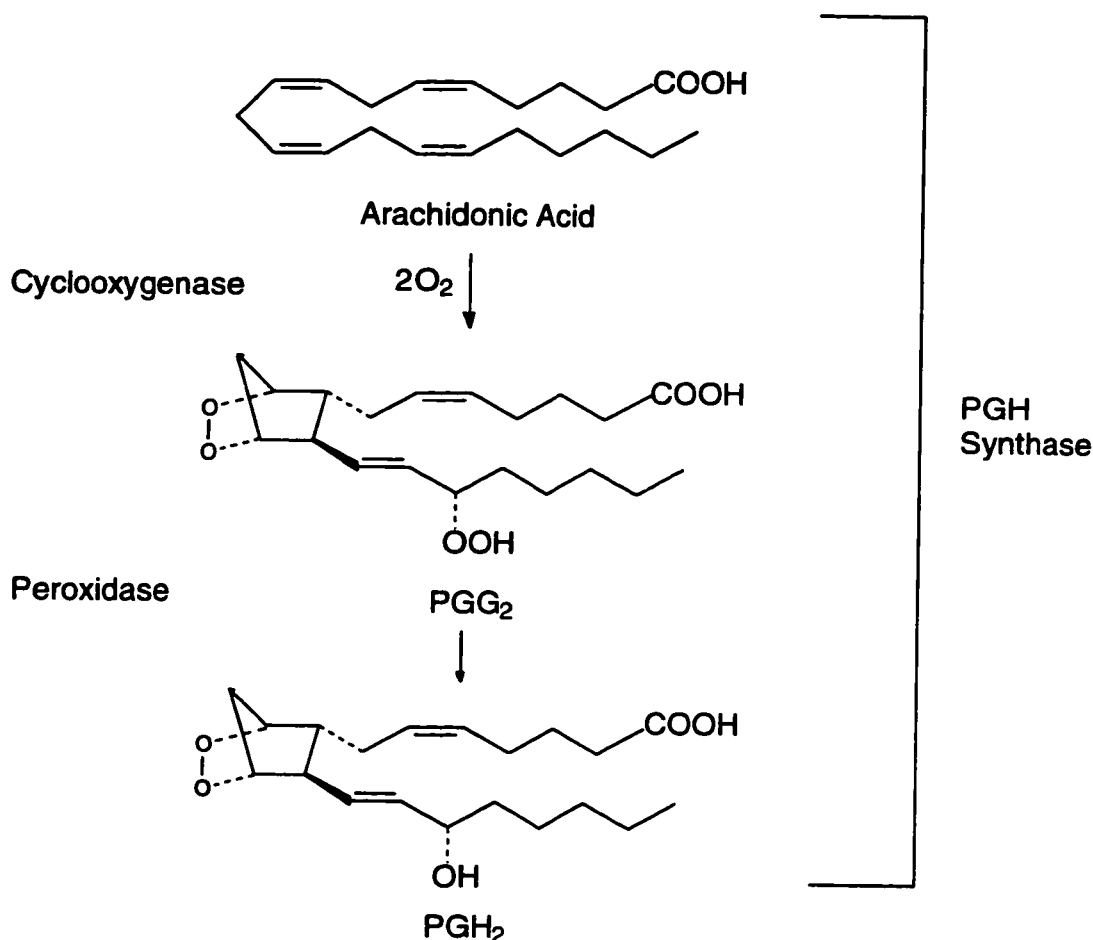
Figure 1.1 Pathway of prostaglandin biosynthesis by COX-1 and COX-2.

that is related to NSAID action is the synthesis of prostaglandin H_2 (PGH_2) from arachidonic acid (AA) through the actions of prostaglandin H (PGH) synthase, as seen in **Figure 1.1**. The enzyme PGHS consists of two components: cyclooxygenase (COX) and peroxidase. The COX component of PGH synthase introduces four oxygen atoms to AA and forms a cyclopentane ring to give PGG_2. The peroxidase component of PGH synthase catalyzes a two-electron reduction of the 15-hydroperoxy group to a 15-hydroxyl group.[8] The PGH_2 is then converted by cell-specific synthases to various prostaglandins, which are short-lived hormones

that can stimulate inflammation. Although NSAIDs influence a wide range of different biochemical and physiological systems, it is generally believed that it is their ability to decrease the production of these PGs through the inhibition of COX that underlies their anti-inflammatory effect.

There are two COX enzymes, referred to as COX-1 and COX-2. The second of these isozymes was discovered relatively recently. The similarity of COX-2 to COX-1 has stimulated research directed at determining the biological rationale for the apparent redundancy. COX-1 and COX-2 are encoded by separate genes and appear to have different biological roles, but the enzymes are stucturally homologous, and both enzymes catalyze the formation of PGH_2 from AA with similar kinetic properties.[9]

The COX-1 enzyme is expressed in most tissues, but at different levels in various cell types.[10] Prostaglandins produced by COX-1 are thought to mediate physiological responses to circulating hormones that require constant or rapid modulation, the so-called housekeeping functions. These events include the regulation of renal H_2O and Na^+, and gastroprotection of the stomach. It follows that the enzyme is expressed at higher concentrations in the tissues of the kidney and stomach.

In contrast with COX-1, COX-2 is an inducible enzyme that is normally absent from cells. It can be expressed at high levels in certain cell types after induction with a variety of substances.[9] The COX-2 pathway produces prostaglandins that likely are only employed in the secondary step of physiological events such as inflammation. However, despite intense investigation of

prostaglandin synthesis and function, exact models for the individual roles of COX-1 and COX-2 remain elusive.

The implication that inflammation may be mediated primarily through prostaglandins produced by COX-2 has been well appreciated by pharmaceutical companies. Two major side effects of long-term use of anti-inflammatory doses of NSAIDs are stomach ulceration and nephrotoxicity. Since COX-1 is the major source of prostaglandins in the stomach and kidney, it seems likely that NSAIDs that inhibit only COX-2 would have reduced gastric toxicity and possibly better anti-inflammatory properties. In fact, this has proven to be the case in preliminary studies with some NSAIDs and the isozymes.[9]

Azapropazone is a weak PG inhibitor,[11] which probably accounts for the low GI ulceration. What is not known is if it is solely a COX-2 inhibitor, which would also explain the low GI damage and anti-inflammatory activity. The crystal structure data found in **Chapters 3** and **4** of this thesis are being used by another research group for drug-active site modelling with the crystal structure data of the COX-1 and COX-2 sites to provide information about the mode of action of azapropazone.[12,13]

1.3 Magnetic Resonance Imaging

The principles behind magnetic resonance imaging (MRI) are an extension of those used for nuclear magnetic resonance (NMR) in the single dimension. The theory is based on the fact that protons, and other nuclei with nonzero nuclear spin, possess a nuclear magnetic moment, and therefore interact with an external field (B_0) to produce several nuclear spin energy states. For protons, two states

exist; one corresponding to the proton nuclear moment aligned with the field, and the other antiparallel to it. Usually, alignment with the field is more stable, and this is the position of more of the protons at equilibrium. The energy required to produce transitions between the two states depends on the strength of B_o. For MRI, the magnetic fields are on the order of 0.002 to 2 Tesla, so the energy needed is in the radio frequency region, 0.08 to 80 MHz. The condition where the magnetic field produces an energy separation between nuclear spin levels that exactly matches the applied radio frequency radiation is called resonance. This relationship is summarized in the Larmor equation:

$$f_{Larmor} = \gamma B_o \qquad (1\text{-}1)$$

where f_{Larmor} is the resonance frequency in MHz, B_o is in Tesla, and γ is the magnetogyric ratio which is particular for each nucleus and is defined with the units MHz/Tesla.

The proton nuclei of tissue water molecules are responsible for the signal imaged by MRI. To produce an image based on the magnetic resonance signal, a linear magnetic field gradient is applied, perpendicular to the static magnetic field, to "spatially encode" the nuclei with different resonant frequencies. For instance, if a linear variation of the field occurs along the x coordinate of a Cartesian coordinate system, the resonance frequency will be dependent on the location of the volume of interest with respect to x. The gradient system results in the selection of a resonant slice approximately 1 centimeter thick in the subject (**Figure 1.2**)[14]. Within the slice, applied pulses of radiation separated by time intervals produce a
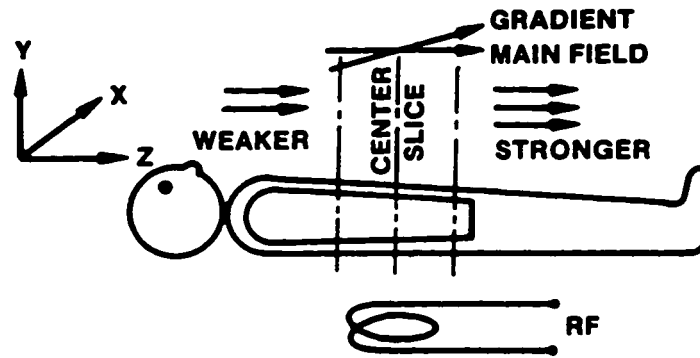
Figure 1.2 MR images of slices are obtained by imposing a magnetic field gradient in addition to the main field. (Ref. 14, p. 645)

signal that may be either an "echo" or a "free induction decay", depending upon the details of the pulse sequence. This signal, which is monitored by a receiver coil, is Fourier transformed by a computer to produce a one dimensional projection of signal amplitude along a line across the slice of subject. When this process is repeated several times for different gradient strengths, and with the aid of computer algorithms, an image may be constructed. A more detailed description of MRI techniques is available in books by Morris[15], and Leach[16].

Magnetization and Relaxation

In order to understand the dependence of the MRI signal intensity upon
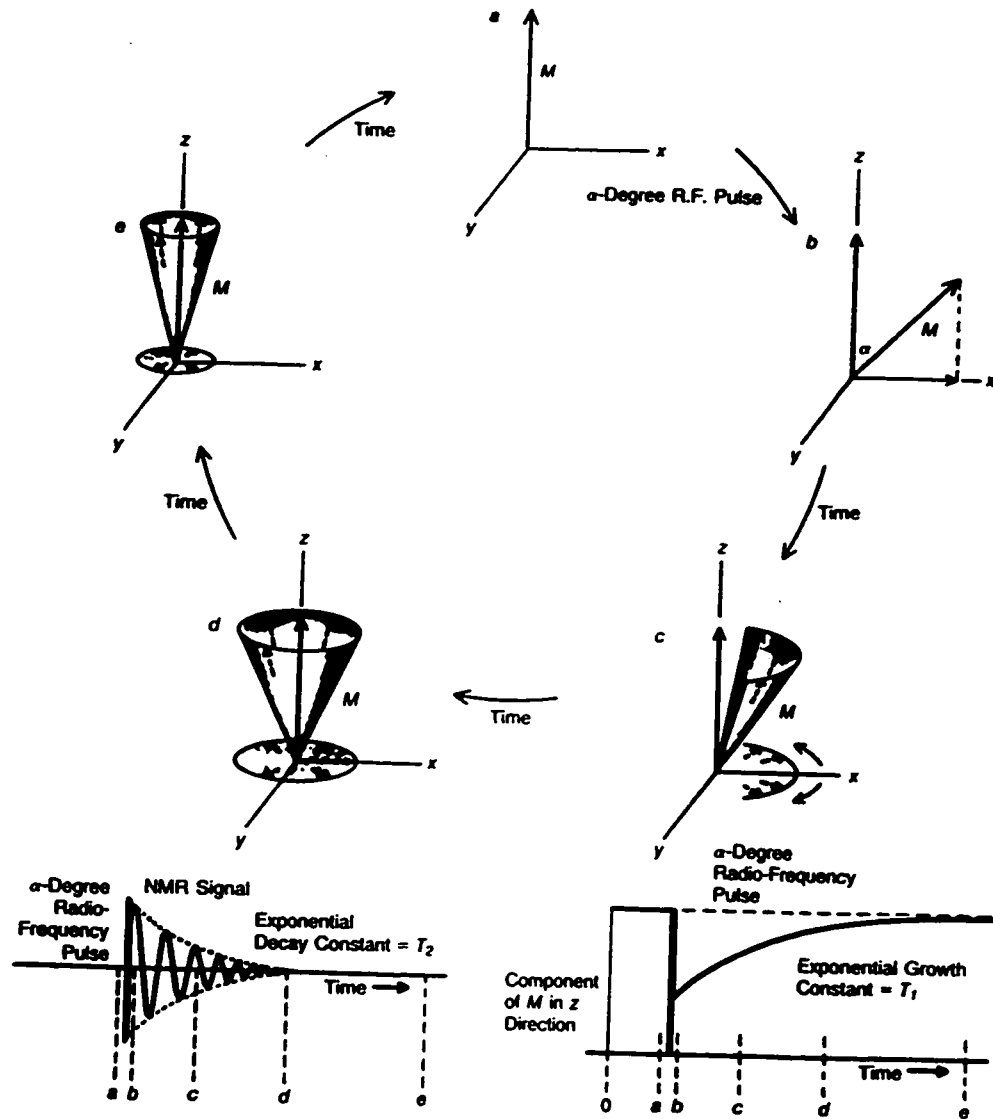
Figure 1.3 Perturbation and relaxation of the magnetization vector M in a magnetic field. See text for details. (Reference 14, p. 647).

the properties of tissue proton nuclei, the effects of radio frequency pulses upon the slight magnetization produced in the subject by the static magnetic field must be visualized. In a pulsed NMR experiment the emitted signal is observed after the radio frequency energy is turned off. Magnetization in the static field can be represented by a vector that points in the direction of the applied magnetic field, defined as the z axis, and shown as M in **Figure 1.3(a)**. The diagrams in **Figure 1.3**

assume that the frame of reference is rotating at the RF of the pulse. Whenever this magnetization vector is perturbed by radio frequency (RF) radiation directed at the subject along the x axis, for example, the direction of magnetization is "tipped" through an angle α and there will be a component of **M** in the x-y plane **(b)**. For a brief instant the NMR signal is at a maximum (curve at bottom left of **Figure 1.3**). After the RF radiation is turned off, however, the magnetization soon returns to its equilibrium orientation along the z axis. The nuclei precess at slightly different rates because of magnetic interaction between nuclei and slight nonuniformities in the magnetic field. The regrowth of the z component of **M** is approximately exponential and is characterized by the time constant T_1 (see curve at bottom right of **Figure 1.3**). Similarly, the net component of **M** in the x-y plane diminishes, and the signal amplitude decays approximately exponentially with a time constant T_2 (see curve at bottom left of **Figure 1.3**). The constant T_1 is referred to as the spin-lattice or longitudinal relaxation time, and T_2 is called the spin-spin or transverse relaxation time. T_2 can be equal to $2(T_1)$, but never longer, because field inhomogeneity may shorten T_2. The relaxation behaviour is also represented as the longitudinal relaxation rate, $1/T_1$, or the tranverse relaxation rate, $1/T_2$.

Signal Intensity in Tissue

The signal intensity in an MR image depends upon the details of the pulse sequence used to generate the image. Pulse sequences can be selected that yield images with signal intensity proportional to T_1, T_2, or proton density. Tissues with short T_1 values generally yield greater image intensity than those with longer values

since the steady-state magnetization along the z axis is greater in the tissue with the fastest relaxation. Conversely, short T_2 values are always associated with lower signal intensity since this diminishes the net transverse magnetization available for detection. Protons in nonstationary tissue such as blood or cerebral spinal fluid (CSF) also influence signal intensity. Proton concentration is always a multiplicative factor in the signal intensity of MR images. Bone is invisible in MR images because it contains few mobile protons. Fat tissue, though containing less water than other tissues, has a high concentration of methylenic hydrogens that contribute to signal intensity because of their closeness in resonant frequency to water hydrogen and their very short T_1. Blood and CSF often appear dark in MR images because of their long T_1.[14]

1.4 Contrast Agents in MRI

Magnetic resonance imaging as a diagnostic imaging tool is advantageous because it uses nonionizing radiation and modest magnetic fields, and is noninvasive in nature. Primary disadvantages include the expensive instrumentation,[17] relatively lengthy data collection,[17] and the occasional lack of diagnostic specificity, in spite of excellent anatomical detail (spatial resolution $\approx$ 1-3 mm)[15]. An example of the latter disadvantage is that most pathological lesions produce regions of lengthened T_1 regardless of their nature. Thus, a region visualized on MRI with long T_1 times may represent either tumour, edema, hemorrhage, or inflammation. It is hoped that MR contrast agents which selectively alter T_1 values between tissues will provide a means of obtaining images of greater diagnostic specificity and enhanced anatomical detail. Also, MRI contrast agents

have the potential to lower T_1 values of tissues, enabling image acquisition over shorter periods of time, with an additional potential improvement in cost effectiveness. More important for the future, MR contrast agents permit extensions of imaging conditions into regions that currently have poor tissue contrast. Dynamic imaging with contrast agents should even allow organ function to be assessed.

General Requirements for MRI Contrast Agents

MR imaging contrast agents must be biocompatable pharmaceuticals in addition to nuclear relaxation probes, as well as have the standard pharmaceutical features such as water solubility and shelf stability. Stable complexes of paramagnetic transition and lanthanide ions, which can decrease the relaxation times of nearby nuclei via dipolar interactions, have received the most attention as potential contrast agents. The efficiency with which the complex enhances the proton relaxation rates of water, referred to as relaxivity (R_1, units: $mM^{-1}s^{-1}$), must be sufficient to significantly increase the relaxation rates of the target tissue. The dose of the complex at which alteration of tissue relaxation rates occurs (0.2 mmol/kg, *ca.* 10 g for an adult) must be water soluble and nontoxic to the patient. As small as 10-20% increases in $1/T_1$ can be detected by MR imaging. Methods to optimize the relaxivity of a complex are found in the next section.

The acute and chronic toxicity of an intravenously administered metal complex is related to its stability *in vivo* and its tissue clearance behaviour.[18] While the circulatory system tends to be maintained at pH 7.4 at 37°C by a complex background medium including enzymes, whole cells, and proteins such as albumin, the local pHs of the stomach or bile, for example, are much lower. The body may

also contain relatively high local concentrations of certain metal ions, such as Ca^{2+} and Zn^{2+}. Thus, the metal complex must be thermodynamically and kinetically stable enough to endure these conditions. The transition metal and lanthanide ions are relatively toxic, as is the free ligand, at the doses required for NMR relaxation rate changes. Thus, the dissociation of the complex cannot occur to any significant degree. Additionally, a diagnostic agent should be excreted within hours of administration.

Relaxation Enhancement by Paramagnetic Complexes

The agents presented in this thesis are intended to be T_1 relaxation agents. The longitudinal relaxation time of water proton nuclei T_1 is shortened by dissolving a relaxation-enhancement paramagnetic complex in the water. The observed relaxation rate is a combination of both diamagnetic and paramagnetic relaxation rates. A plot of the relaxation rate $1/T_1$ versus concentration gives a straight line with a slope equal to the relaxation rate enhancement per unit concentration, and is called the relaxivity, R_1 (in $mM^{-1}s^{-1}$), of the complex. The intercept of the line is the relaxation rate of pure water. Relaxivities are also dependent on frequency and temperature.

There are two mechanisms by which an ion can affect the relaxation rate of water molecules; the first is labelled inner-sphere relaxation and the second is outer-sphere relaxation. Inner-sphere relaxation occurs when a water molecule is coordinated to a paramagnetic ion or hydrogen bonded to the complexed ion species. The T_1 relaxation stems from the chemical exchange of the bulk water molecules with the primary coordination sphere of the water molecules coordinated

to the paramagnetic ion. The outer-sphere contribution to relaxation is not as well understood as the inner-sphere contribution. It occurs when a water molecule diffuses by a paramagnetic species without binding to the paramagnetic ion. The residence time of the water in the vicinity of the ion is quite low, and consequently the relaxation enhancement of the bulk water protons is small.

The inner-sphere contribution to longitudinal relaxation is expressed in Equation 1-2:

$$[\frac{1}{T_1}] \ inner \ sphere = \frac{P_M q}{T_{1M} + \tau_M} \qquad \text{1-2}$$

where q is the number of water molecules bound per metal ion, T_{1M} represents the relaxation rate of protons in water molecules coordinated to the metal ion M, P_M is the mole fraction of metal ion ([M]/55.5), and τ_M is the residence lifetime of the bound water.

The relaxation rate of protons in a water molecule coordinated to a paramagnetic ion, $1/T_{1M}$, is given by the Solomon-Bloembergen equation[19] that expresses the rate as a sum of dipolar (through space) and scalar (through bonds) contributions (eq. 1-3):

$$\frac{1}{T_{1M}} = \frac{2}{15} \frac{(\gamma_I^2 g^2 S(S+1)\beta^2)}{(r^6)}(\frac{7\tau_c}{1+\omega_s^2\tau_s^2}+\frac{3\tau_c}{1+\omega_I^2\tau_c^2}) + (\frac{2}{3})S(S+1)(\frac{A}{\hbar})^2(\frac{\tau_e}{1+\omega_s^2\tau_c^2})$$

where γ_I is the proton magnetogyric ratio, g is the electronic g-factor, S is the total electron spin of the metal ion, β is the Bohr Magneton, r is the proton-metal ion distance, ω_s and ω_I are the electronic and proton Larmor frequencies, and A/ℏ is the electron-nuclear hyperfine constant. Both terms consist of the magnitude of the interaction (dipole-dipole or scalar) multiplied by a function of the correlation time (τ), which expresses the intensity of modulation of the interaction of the Larmor frequency. The correlation times τ_c and τ_e are given by equations 1-4 and 1-5:

$$1/\tau_c = 1/T_{1e} + 1/\tau_M + 1/\tau_R \qquad \text{(1-4)}$$

$$1/\tau_e = 1/T_{1e} + 1/\tau_M \qquad \text{(1-5)}$$

where T_{1e} is the longitudinal electron spin relaxation time, and τ_R is the rotational tumbling time of the entire metal-water unit. Each component of the correlation times helps to determine how to optimize the relaxivity of a contrast agent, and are examined in the next section.

Parameters For Relaxivity Optimization

There are physical and chemical parameters that may be optimized to increase the relaxivity of paramagnetic agents. Such an optimization may minimize the required effective dose. This discussion is most relevant to contrast agents that include paramagnetic metals such as Gd(III), Mn(II), and Fe(III). These ions generally exhibit the higher relaxivity because of large magnetic moments and long electron spin relaxation times (T_{1e}'s).

Lauffer has outlined the parameters for relaxivity optimization in his landmark review on MRI contrast agents.[20] The first two parameters discussed, r, the distance

between the water protons and the unpaired electron spin, and q, the number of water molecules coordinated to the metal, are important in governing the strength of the electron-nuclear dipolar interaction. The parameters τ_R and T_e in part determine the time scale of the fluctuations in the unpaired electron's magnetic field at the nucleus. Finally, τ_M is important in modulating the chemical exchange of water between chelate-bound and bulk environments.

Number of Coordinated Water Molecules, q

There is a trade-off between relaxivity on one hand and stability and toxicity on the other. This is because chelation of a metal ion with a multidentate ligand, while forming a stable and preferably nontoxic complex, leads to an enormous decrease in relaxivity largely due to the loss of some of the directly coordinated water molecules. The higher doses of such a chelate necessary to alter tissue relaxation rates may partially offset its increased safety.

The presence of at least one water molecule coordinated to the paramagnetic metal, or the inner sphere, can lead to high relaxivities on the order of 20-200 $mM^{-1}s^{-1}$ if other relaxivity parameters are optimized. Relaxivity may also be increased, by a factor of two or so, by encouraging second sphere water molecule coordination and subsequent relaxation by increasing the number of hydrogen bonding sites in the second sphere.

Distance between the Water Protons and the Unpaired Electron Spin, r

There is a $1/r^6$ dependence in dipolar interactions that has presented the opportunity to increase relaxivity by chemically inducing an orientation of bound

water molecules such that the protons are closer to the metal center. In one case, for Mn(II), the reduction of the metal-proton distance by roughly 0.2 Å (of 3 to 5Å) generated 50% greater relaxivity.[21] This parameter can be optimized by structurally designing a system where the proton is brought closer to the unpaired spin density, or conversely, the unpaired spin density is delocalized towards the proton.

Rotational Correlation Time, τ_R

For metal ions with long T_{1e}'s, alteration of the rotational tumbling time τ_R ($\approx 10^{-11}$s for a moderate molecular weight complex) is the most important source of relaxivity enhancement. The degree of relaxivity enhancement possible, which is limited by T_{1e} and τ_M according to equation 1-3, exceeds that which is realistically available from optimizing any of the other parameters. Basic strategies to reduce the rotational mobility of metal complexes *in vivo* include the distribution of the agent into a tissue or tissue compartment with high microviscosity, and attachment of the complex to a larger molecule such as a protein.

The first of these ideas is important for understanding the relaxivity of metal chelates in tissue. Debye-Stokes theory predicts that for a spherical molecule of radius a, τ_R is directly proportional to the viscosity of the medium, η, and the third power of the radius, as given in equation 1-6, where k is the Boltzmann constant and T is the absolute temperature. The relaxivity of a complex should be directly

$$\tau_R = 4\pi a^3 \eta / 3kT \qquad (1\text{-}6)$$

proportional to η, until τ_R approaches the value of T_{1e} and/or τ_M.

Large gains in relaxivity are possible through covalent or noncovalent attachment of a chelate to a macromolecule. Protein molecules, for example, generally have τ_R's of 10 ns or longer. Rigidly attached chelates experiencing this tumbling behaviour would exhibit the highest possible relaxivity.

Electron Spin Relaxation Time, T_{1e}

The choice of Gd(III), Mn(II), and Fe(III) as optimal relaxation agents stem from their long T_{1e}'s (10^{-9} to 10^{-11} s) and large magnetic moments. In these ions with stable half-filled d or f shells, the pathways for electronic relaxation are relatively inefficient compared with other electronic configurations. In general, increasing T_{1e} will yield higher relaxivity, limited by the values of τ_M and τ_R.

Residence Lifetime of Coordinated Waters, τ_M

The residence lifetime, τ_M, which is on the order of 10^{-6} to 10^{-9} s for a labile metal ion, has a dual importance in relaxivity: it can contribute to the overall correlation time, τ_c (eq **1-3**), and it modulates the efficiency of the chemical exchange of water molecules sampling the paramagnetic center. The lability of monodentate metal-ligand bonds in complexes of ions with no ligand field stabilization energy, such as those of Gd(III), Mn(II), and Fe(III), results in the short τ_M values.

It is clear that $1/\tau_c$ is dominated by the fastest of the processes, $1/\tau_R$, $1/\tau_M$, or $1/T_{1e}$ to which it is related. For the metal ions most suitable for MR contrast agents, τ_c is dominated by the rotational contribution because water exchange and electron

spin relaxation are slower processes.

For a more detailed look at contrast agents, Lauffer,[20] and also Tweedle,[22] have prepared excellent reviews on the subject. For a literature review of the current contrast agents related to the agents presented in this work, see **Section 5.1.**

1.5 *In Vivo* Targeting

Targeting a paramagnetic agent to a particular site within the body is one of the most challenging aspects of NMR contrast agent design. The diagnostic utility of a contrast-enhanced NMR image will depend on the absolute concentration of the agent in the desired tissue and the selectivity of the distribution relative to other tissues. The biodistribution of a metal complex is principally determined by its shape, charge, redox properties and lipophilicity. Alternatively, the complex may be conjugated to a different targeting molecule, in which case the properties of the targeting molecule should determine the biodistribution of the complex.

The schematic diagram shown in **Figure 1.4** illustrates potential distribution sites and excretion pathways relevant for soluble metal complexes. An intravenously administered chelate rapidly equilibrates in the intravascular and interstitial (space between cells) fluid compartments; these collectively are referred to as the extracellular compartment. Depending on its structure, the complex may also distribute into various intracellular environments (including that of the liver and kidney) by passive diffusion or specific uptake processes. If the complex has a neutral charge, sufficient lipophilicity and a low molecular weight, it may even
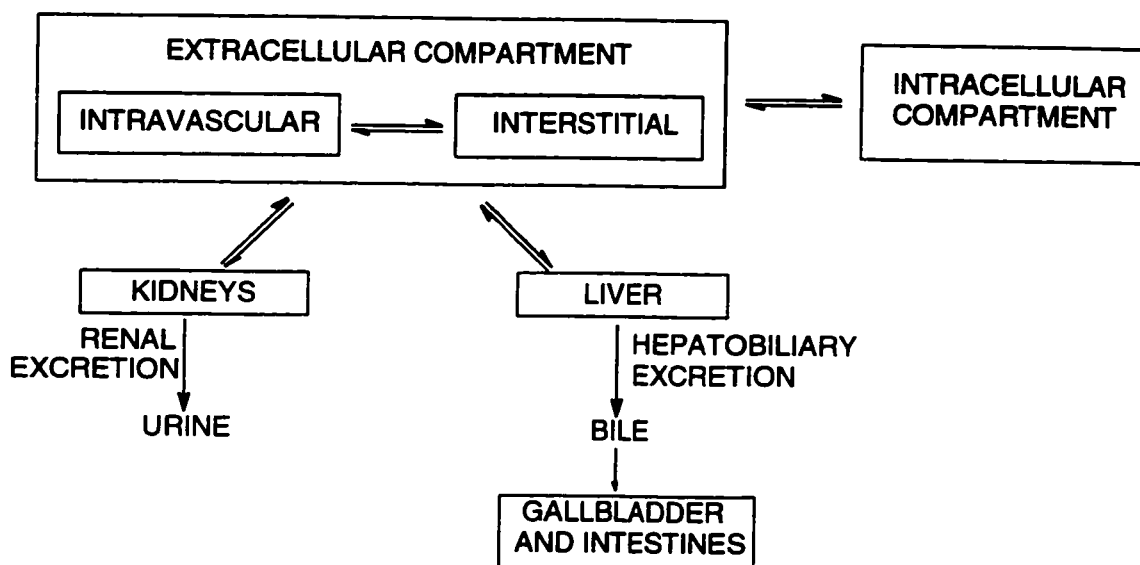
Figure 1.4 Principal distribution sites and excretion pathways for intravenously administered soluble metal complexes (ref.22, 919).

penetrate the blood-brain barrier.

The structure of the complex determines its excretion pathway.[18] Generally, small molecular weight hydrophilic chelates that do not bind to plasma proteins are nonspecifically filtered out in the kidneys (renal excretion).[23] If the molecule possesses a balance between hydrophobic and hydrophilic character, particularly if it contains aromatic rings, some fraction of the complex is taken up by liver cells and excreted into the bile (hepatobiliary excretion).[24] The hepatobiliary and renal pathways can therefore be competitive. Commonly, the greater degree of lipophilicity a molecule possesses, the greater the hepatobiliary excretion. The complete clearance of the agent from the body by either route is desirable to minimize toxicity. If, however, the complex is very lipophilic, it may distribute into

fat storage sites or membranes or precipitate in blood and be taken up by reticuloendothelial cells in the liver and spleen. Both possibilities lead to long-term retention of the agent, which may be associated with chronic toxicity.

This thesis presents ligands that were designed to achieve some site specificity. The work with amino acid derivatives of EDTA and DTPA can be found in **Chapter 6**, and the work with azapropazone derivatives of EDTA and DTPA can be found in **Chapter 7**.

1.6 Single Photon Emission Computed Tomography (SPECT)

NMR imaging agents are similar to radiopharmaceuticals in that the image enhancement of both depends on the concentration of a metal complex. The principles of distribution govern both classes of imaging agents. In addition, the Gd(III), Fe(III), and Mn(II) metal ions prefer oxygen and nitrogen donor atoms, as do the metals In(III) and Ga(III), which possess isotopes commonly used in radiopharmaceuticals. Because of the similarities between these imaging agents, some of the ligands presented in this thesis were able to be evaluated for their biodistribution properties with ^{111}In(III) as the γ-emitter in single photon emission computed tomography, known as SPECT imaging.

The γ-rays emitted from certain radioisotopes are a form of electromagnetic radiation that is highly penetrating and travels at the speed of light. The γ-rays originate within the nuclei as a result of transitions between nuclear energy levels and therefore have one or a few discrete energies. The rays emitted from a decaying radioisotope can be detected by using a scintillation camera. A collimater

is used to localize radiation on a detector as the radiation is randomly emitted. The detector consists of a thallium doped NaI crystal which emits a flash of light when struck by a γ-ray. The light flashes are amplified using photomultipliers and are counted as electrical pulses. The spatial resolution is about 1-2 cm, which is an order of magnitude lower than for MR imaging. A three dimensional image is obtained by mounting the scintillation camera on a rotating gantry, recording multiple images at different angles of the patient, and reconstructing the activity distribution through a back projection process.

It was found that SPECT imaging was useful in determining biodistribution patterns for some of the ligands presented in this work. SPECT imaging required much lower doses of the imaging agent, so potential solubility problems could be avoided. Further details on the animal experiments that were performed with SPECT imaging can be found in **Chapter 8**.

Chapter 2

General Experimental Methods

2.1 Chemical Reagents

Azapropazone was provided by Siegfried Pharma (Zofingen, CH). The free acids and salts of EDTA, DTPA, and the p-toluenesulfonate salts of glycine benzyl ester, phenylalanine benzyl ester, and tyrosine benzyl ester, were purchased from Sigma (Mississauga, Ontario) and used without further purification. Bulk organic solvents were obtained from Caledon Laboratories (Georgetown, Ontario). Inorganic acids were obtained from Fisher Scientific (Fairlawn, New Jersey). The following chemicals were obtained from BDH Chemicals (Toronto, Ontario): potassium hydroxide, sodium bicarbonate, and sodium hydroxide. The NMR solvents DMSO-d_6 and CD_3OD were from Cambridge Isotope Laboratories, and D_2O (99.9%) was from Isotec. Sodium 2,2-dimethyl-2-silapentane-5-sulfonate (DSS) was obtained from MDS Isotopes. The hexahydrates of $LaCl_3$ and $GdCl_3$ and all other chemicals were obtained from Aldrich Chemical Company (Milwaukee, USA).

Dry Solvents

When dry solvents were required, they were distilled by standard methods. Dimethylformamide (DMF) (1 L) was stirred overnight with benzene (50 mL) which had been dried over calcium hydride. The benzene was distilled off, and the

24

remaining DMF was distilled from calcium hydride at reduced pressure. The dry DMF was stored over molecular sieves (Linde Molecular Sieves, 4A) in a glove bag filled with dry nitrogen. Pyridine was stored over calcium hydride for 12 h and then distilled onto molecular sieves. This was also stored in a glove bag.

Distilled/Deionized Water (DDW)

A Milli-Q purification system (Waters Associates, Millford, Massachusetts) was used to deionize and further purify distilled water.

2.2 Compound Characterization

2.2.1 Vibrational Spectroscopy

Infrared spectra were recorded on a Bio Rad FTS-40 Fourier transform spectrometer. Solid samples were prepared as KBr pellets (1-5% w/w) in the 4000-400 cm^{-1} region. Spectra were calibrated against polystyrene.

2.2.2 Nuclear Magnetic Resonance Spectroscopy

Samples for NMR spectroscopy were prepared by dissolving the compounds in the appropriate deuterated solvents at a concentration of about 20mg/mL and transferred to 5 mm thin-walled NMR tubes. Chemical shifts are reported in ppm relative to tetramethylsilane (TMS). The residual solvent signals at 2.49 ppm (DMSO-d$_6$) or 3.30 ppm (CD$_3$OD) were used as internal references for the ^{1}H NMR spectra. The ^{13}C NMR spectra for samples in DMSO-d$_6$ and CD$_3$ OD used the residual sovent signals at 49.0 and 39.5 ppm, respectively, as internal references. For samples dissolved in D$_2$O, ^{1}H chemical shifts were referenced relative to internal DSS at 0.0 ppm while the ^{13}C chemical shifts were referenced using external

dioxane in D_2O at 66.6 ppm.

Bruker AC-200 NMR Spectra:

Proton NMR spectra recorded on the Bruker AC-200 spectrometer were acquired at 200.13 MHz using a 5 mm dual frequency probe. Spectra were obtained in 32 scans in 16K data points over a 2.4 kHz spectral width (3.413 s acquisition time). Sample temperature was ambient. The free induction decays (FID) were processed using exponential multiplication (line broadening: 0.2 Hz) and were zero-filled to 32 K before Fourier transformation.

Carbon-13 NMR spectra were recorded at 50.33 MHz using a 5 mm dual frequency probe. The spectra were acquired over a 12.0 kHz spectral width in 16 K data points (0.672 s acquisition time). The ^{13}C pulse width was 3.2 μs (35° flip angle). A 0.5 s relaxation delay was used. The FIDs were processed using exponential multiplication (line broadening: 4.0 Hz) and zero-filled to 32 K before Fourier transformation.

Bruker AC-300 NMR Spectra:

Proton NMR spectra recorded on the Bruker AC-300 specttrometer were acquired at 300.135 MHz using a 5 mm QNP probe (Bruker, Milton, Ontario). The spectra were obtained in 8 scans in 16 K data points over a 3.145 KHz spectral width (2.605 s acquisition time). Sample temperature was maintained at 27° C by a Bruker Eurotherm B-VT 2000 variable temperature unit. The free induction decay (FID) was processed using exponential multiplication (line broadening: 0.2 Hz) and was zero-filled to 32K before Fourier transformation.

Carbon-13 spectra were recorded at 75.469 MHz using a 5 mm QNP probe.

The spectra were acquired over a 17.857 kHz spectral width in 16 K data points (0.459 s acquisition time). The ^{13}C pulse width was 3 μs (42° flip angle). A 0.5 s relaxation delay was used. The FIDs were processed using exponential multiplication (line broadening: 4.0 Hz) and zero-filled to 32 K before Fourier transformation.

T_1 data were collected at 7.05 T on a Bruker AC-300 Fourier transform spectrometer at 27°C. The longitudinal relaxation times were measured by the inversion -recovery method. The ^{1}H 90° pulse width was determined independently for each sample and was often in the range of 7-9 μs. There were 10 variable delay times used for each sample. The relaxation delay ranged from 5 to 40 s, and depended on the anticipated T_1 time (relaxation delay $\geq$ 5(T_1)). Each FID was acquired in 4 scans. Each spectrum was processed with a line broadening value of 20 Hz.

The ^{13}C nuclear Overhauser effect (NOE) was determined for the methylene carbons of some of the ligands presented in this thesis. Data were collected in 2048 scans at a ^{13}C 90° pulse width of 4.8 μs. The 4K of data collected with a spectral width of 0.3 kHz resulted in an acquisition time of 6.83 s. The relaxation delay was 10 s.

Bruker DRX-500 NMR Spectra:

Proton NMR spectra were acquired at 500.130 MHz using a 5 mm broadband inverse probe with triple axis gradient capability. Spectra were obtained in 8 scans in 32K data points over a 4.006 kHz spectral width (4.096 s acquisition time). Sample temperature was maintained at 30° C by a Bruker Eurotherm variable

temperature unit. The free induction decay (FID) was processed using Gaussian multiplication (line broadening: -1.5 Hz, Gaussian broadening: 0.2) and was zero-filled to 64K before Fourier transformation.

Proton COSY 2-D NMR spectra were recorded in the absolute value mode using the pulse sequence 90° - t_1 - 45° - ACQ and including pulsed field gradients for coherence selection. Spectra were acquired in 1 scan for each of the 256 FIDs that contained 2K data points in F2 over the previously mentioned spectral width. The ^{1}H 90° pulse width was 6.6 μs. A 1.0 s relaxation delay was employed between acquisitions. Zero-filling in F1 produced a 1K x 1K data matrix with a digital resolution of 2.85 Hz/point in both dimensions. During 2-D Fourier transformation a sine-bell squared window function was applied to both dimensions. The transformed data were then symmetrized.

Carbon-13 NMR spectra were recorded at 125.758 MHz using the 5 mm broadband inverse probe with triple axis gradient capability. The spectra were acquired over a 28.986 kHz spectral width in 32K data points (0.557 s acquisition time). The ^{13}C pulse width was 4.0 μs (30° flip angle) and a relaxation delay of 1.0 s was used. The FID was processed using exponential multiplication (line broadening: 4.0 Hz) and zero-filled to 64K before Fourier transformation.

Inverse detected ^{1}H - ^{13}C 2-D chemical shift correlation spectra were acquired in the phase sensitive mode using the pulsed field gradient version of the HSQC pulse sequence. The FID's in the F2 (^{1}H) dimension were recorded over a 3.655 KHz spectral width in 1K data points. The 128 FID's in the F1 (^{13}C) dimension were obtained over a 21.368 KHz spectral width. Each FID was acquired in 2 scans.

The fixed delays during the pulse sequence were a 1.0 s relaxation delay and 0.0018 s for polarization transfer. The 90° ^{1}H pulse was 6.6 μs while the ^{13}C 90° pulse was 11.6 μs. The data were processed using a sine-bell squared window function shifted by π/2 in both dimensions and linear prediction to 256 data points in F1 followed by zero-filling to 1K.

Inverse detected ^{1}H - ^{13}C 2-D chemical shift correlation spectra through two- and three-bond coupling interactions were acquired in the absolute value mode using the pulsed field gradient version of the HMBC pulse sequence. The FID's in the F2 (^{1}H) dimension were recorded over a 3.655 KHz spectral width in 1K data points. The 128 FID's in the F1 (^{13}C) dimension were obtained over a 21.368 KHz spectral width. Each FID was acquired in 2 scans. The fixed delays during the pulse sequence were a 1.0 s relaxation delay, a 0.0033 s delay for the low pass J-filter and 0.08 s delay to allow evolution of the long-range coupling. The 90° ^{1}H pulse was 6.6 μs while the ^{13}C 90° pulse was 11.6 μs. The data were processed using a sine-bell squared window function shifted by π/2 in both dimensions and linear prediction to 256 data points in F1 followed by zero-filling to 1K.

2.2.3 Mass Spectrometry

Chemical Ionization and Electron Impact

Chemical ionization (CI), with ammonia as the reagent gas (NH_3-CI), and electron impact (EI) mass spectra were recorded on a VG Analytical ZAB-E double focusing mass spectrometer. Low resolution spectra were recorded for routine sample analysis of non-polar samples where appropriate. Typical experimental

conditions were: mass resolution 1000, electron energy 70 eV, source temperature 200°C, source pressure 2×10^{-6} mbar for EI and 4×10^{-5} mbar for CI. Mass spectra were reported as percent intensity (%) *versus* mass/charge (m/z) ratio.

Electrospray Ionization Mass Spectrometry

The techniques of electrospray mass spectrometry (ESMS) can produce stable gas phase ions for a broad range of involatile and thermally labile analytes which previously could not be easily studied by mass spectrometry. It has been shown to be very useful for mass spectrometric analysis of compounds which are ionic in solution; it has been applied successfully to species with molecular weights ranging from 100 to more than 100 000 and is particularly well suited to the characterization of biomolecules.[25] The system could analyze samples for positively charged species (+ve mode) or for negatively charged species (-ve mode). In this work, ESMS was used for characterization of the EDTA and DTPA derivatives, and gave an indication of the purity of the sample.

Pneumatically assisted ESMS was performed with 50/50 CH_3CN/H_2O as the mobile phase at a flow rate of 15 µL/minute, with use of a Brownlee Microgradient syringe pump. Samples were dissolved in 50/50 CH_3CN/H_2O with an addition of 1 drop of 0.1% NH_4OH for samples that were to be analyzed in the -ve mode, or 1 drop of 0.1% HCl for samples that were to be analyzed in the +ve mode. The samples were introduced to the system by flow injection. Full scan ESMS experiments were performed with a Fisons Platform quadrupole instrument and the MS/MS data were generated with a Fisons Quattro II triple quadrupole instrument. Collision activation (CA) was performed with argon as the collision gas at a main

beam attenuation of 25% and a collision energy of 35 eV. All data were acquired in multi-channel analysis (MCA) mode (typically with 5-15 scans). A cone voltage was employed in all ESMS experiments.

2.2.4 Melting Point Determination

Melting points were measured on a Gallenkamp capillary tube melting point apparatus and were uncorrected.

2.2.5 X-ray Crystallography

Computer Programs

The SHELXTL PLUS™ family of programs[26] were used for the solution and refinement of the structures presented in this thesis. Programs included in SHELXTL PLUS are: XPREP (Data Preparation and Reciprocal Space Exploration), XS (Crystal Structure Solution), XL (Crystal Structure Refinement), XP (Interactive Molecular Graphics), and XCIF (Preparation of Tables). Atomic scattering factors, with anomalous dispersion corrections, were used automatically by the programs. Calculations were performed on a Dell Dimension XPS P120c computer.

Crystal Preparation

Crystals suitable for X-ray diffraction experiments were prepared by standard crystal growing methods such as slow solvent evaporation and vapour diffusion.[27] Crystal growing details for the respective compounds will be presented in subsequent chapters.

The crystal dimensions ranged from 0.5 mm to 0.2 mm. Crystals larger than 0.5 mm were cut with a scalpel. Clusters of crystals that needed to be separated

to isolate a single crystal were cut with the tip of a syringe needle. Crystal quality was judged according to cleanliness, uniformity, transparency, and light extinction; sharp, complete extinction upon each 90° rotation of the crystal under crossed polarizers should be observed for those crystals which do not have a three fold axis as a symmetry element.

Crystals which were relatively stable were glued onto 0.05 to 0.2 mm diameter glass fibres with epoxy cement. Crystals which were subject to decomposition upon removal from the mother liquor were immersed in paraffin oil and transferred to 0.2 to 0.5 mm diameter Lindemann glass capillaries which were then sealed with epoxy cement. The capillaries were glued into tapered brass holders. The glass fibres or brass holders/capillaries were secured onto a goniometer head which was then transferred to the diffractometer.

Crystal densities were measured by suspension in a homogenous mixture of two solvents, one more and the other less dense than the crystal. The density of the solvent mixture was determined by accurately weighing in a 2 mL picnometer. Densities were measured in triplicate and reported with an esd calculated from the three measurements. The measured density, D_m, was compared to the calculated density, D_x;

$$D_x = \frac{M_r \cdot Z}{V \cdot N_{Avog.}}$$

(2-1)

where M_r is the formula weight, V is the volume of the unit cell in Å^3, Z is the number of formula units per unit cell, and $N_{Avog.}$ is Avogadro's number. If, after

several determinations, D_m was not reasonably close to D_x, the proposed formula of the compound was assumed to be incorrect. In some cases, disagreement between D_m and D_x could be accounted for by the solvent of crystallization.

Data Collection

Unit cell determination and intensity data collection were performed, with graphite monochromatized radiation and coupled ω(crystal)-2θ(counter) scans on either a Siemens P3 diffractometer (AgKα, λ=0.56086 Å), a Siemens P4 diffractometer equipped with a rotating anode using graphite-monochromated radiation (MoKα, λ= 0.71073 Å), a Rigaku AFC6 diffractometer (CuKα, λ= 1.54180 Å), or, more recently, a P4 Siemens diffractometer equipped with a rotating anode using graphite-monochromated radiation (MoKα, λ= 0.71073 Å) and a Siemens SMART 1K Charge-Coupled Device (CCD) Area Detector (see description below). Crystals were centered optically and, if possible, the longest axis was aligned close to the ω-2θ axis on the diffractometer, in order to minimize absorption. An upper value of 2θ was selected that depended on the scattering power of the crystal. Scan widths were selected based upon the broadness of the peaks collected for unit cell determination. The scan rate for each reflection was determined by the diffractometer computer. Three standard reflections, chosen either manually or automatically, were measured every 97 reflections to monitor the crystal and instrument stability. In most cases, after the initial data collection was completed, a ψ-scan data collection was performed and used for absorption correction.

The CCD Area Detector had a crystal-to-detector distance of 3.991 cm, and

the data collection was carried out in 512 x 512 pixel mode, utilizing 2 x 2 pixel binning. The initial unit cell determination was carried out by scanning 4.5 degrees in 15 frames over three different parts of reciprocal space (45 frames). The strong reflections were chosen and used in the determination of the unit cell. One complete hemisphere was collected, to better than 0.8 Å resolution. Upon completion of the data collection, the first 50 frames were recollected in order to improve the decay corrections analysis (if required).

The intensities, $I(hkl)$, of the Bragg reflections and the corresponding standard deviations, $\sigma[I(hkl)]$ were calculated as follows:

$$I(hkl) = N_p - N_b \tag{2-2}$$

$$\sigma[I(hkl)] = \sqrt{N_p + N_b} \tag{2-3}$$

where N_p is the peak count and N_b is the background count.

Data Reduction

Intensities, $I(hkl)$, and their corresponding standard deviations, $\sigma[I(hkl)]$, were reduced to observed structure factor amplitudes squared, $F_o(hkl)^2$, and their corresponding standard deviations, $\sigma[F_o(hkl)]^2$, as follows:

$$F_o(hkl)^2 = \frac{K \cdot I(hkl) \cdot Abs}{L \cdot p} \tag{2-4}$$

$$\sigma[F_o(hkl)]^2 = \frac{\sigma[I(hkl)] \cdot Abs}{4|\sqrt{|F_o(hkl)^2|}| \cdot L \cdot p}$$ (2-5)

where K is the scaling factor, L is the Lorentz correction factor (a geometric correction which accounts for the relative time each reflection is in the diffracting position), p is the polarization correction factor which accounts for the polarization of the X-ray beam after diffraction, and *Abs* is an absorption correction factor which accounts for the absorption of each diffracted beam as it travels through the crystal. The Lorentz and polarization corrections were performed with the use of the operating software for the particular diffractometer. The absorption corrections, with one exception, were performed by the empirical psi-scan method,[28] and applied by use of the XPREP program. The exception is structure I; the absorption correction for it was done by use of the DIFABS program.[29] However, the validity of the DIFABS absorption correction method has since been called into question.[30]

The processing for data from the CCD Area Detector was carried out by use of the program SAINT[31], which applied the Lorentz and polarization corrections to three-dimensionally integrated diffraction spots. The program SADABS[32] was utilized for the scaling of diffraction data, the application of a decay correction , and the empirical absorption correction based on redundant reflections.

Symmetry equivalent reflections were averaged and an $R_{internal}$ (R_i) value and a R_σ value were calculated to evaluate the internal consistency of the data set. R_i and R_σ are defined as follows:

$$R_i = \frac{\Sigma |F_o(hkl)^2 - \langle F_o(hkl)^2 \rangle|}{\Sigma F_o(hkl)^2}$$

(2-6)

$$R_\sigma = \frac{\Sigma \sigma [F_o(hkl)^2]}{\Sigma F_o(hkl)^2}$$

(2-7)

where the summations involve all input reflections for which more than one symmetry equivalent is averaged, but not the remaining reflections, and $\langle F_o(hkl)^2 \rangle$ is the averaged mean in the merged list. It should be noted that $F_o(hkl)^2$ is the experimentally measured quantity (after application of the appropriate scaling and correction factors (Eq. 2-4)) and, therefore, despite the square, $F_o(hkl)^2$ can sometimes be slightly negative which would indicate that the background in higher than the peak as a result of statistical fluctuations. Also, because these R-indices are based on F^2, they tend to be about twice as large as the corresponding, more traditional, indices based on F.

Structure Solution

The solution of the structures presented in this thesis was accomplished by "direct methods". Atoms which were missing from the initial model were located by performing difference Fourier syntheses and by analyzing the resultant difference electron-density maps. In most cases, hydrogen atom positions were calculated and fixed.

Structure Refinement

Refinement of atomic position and displacement parameters was performed by the method of full matrix least-squares. Because the structures presented in this thesis were refined with use of the Siemen's XL program, there is a significant difference between these refinements and most structure refinements in the less recent literature; refinement by XL is based upon F^2 rather than F, for several reasons.

For a well-behaved structure, the geometrical parameters and their estimated standard deviations (esd's) are almost identical for refinement based upon all F^2 values (*i.e.* all the data) and for a refinement against F, in which data with F's less than, for example, $3\sigma(F_o)$, are ignored. For weakly diffracting crystals and for pseudosymmetry problems, however, the refinement against all data is considerably superior. For refinement based upon F, it is usually impossible to use all of the data because that involves taking the square root of a negative number for reflections of negative intensity (*i.e.* background higher than the peak as a result of statistical fluctuations). For refinement based upon F^2, the esd's are reduced because more experimental information is used and the chance of the refinement falling into a local minimum is reduced. In addition, the use of a threshold for ignoring weak reflections may introduce a bias which can seriously affect the atomic displacement parameters. Though omitting weak reflections is justified (as a time saver) in the early stages of refinement, all data, except for reflections known to suffer from systematic error, should be used for the final refinement. The R-indices based upon F^2 refinement are larger than (often about double) those based upon F, and

are increased further when all the data are used. The considerably more important quantities, such as bond angles and distances, can be determined more accurately by F^2 refinement, with use of all the data.

The quality of the structure refinements of XL are judged according to the 'weighted R2' (wR_2) and 'goodness of fit' (GooF or S) indices based upon F^2:

$$wR_2 = \sqrt{\frac{\sum w[F_o(hkl)^2 - F_c(hkl)^2]^2}{\sum w[F_o(hkl)^2]^2}} \qquad (2\text{-}8)$$

$$GooF = S = \sqrt{\frac{\sum w[F_o(hkl)^2 - F_c(hkl)^2]^2}{(n-p)}} \qquad (2\text{-}9)$$

where n is the number of reflections and p is the total number of parameters refined. The weighting scheme, w, has the general form,

$$w = \frac{1}{\sigma^2[F_o(hkl)]^2 + (a \cdot P)^2]} \qquad (2\text{-}10)$$

where $P = [\text{Max}(F_o, 0) + 2F_c^2]/3$ and a is a weighting factor which is dependent upon the progress of the particular refinement. The weighting factor, a, was given a value of 0.1 for the early stages of the refinements. After all the non-hydrogen atoms had been found and the heavier atoms were refined anisotropically, a was given the value suggested by XL after the previous refinement job.

During the refinements, R indices, atomic position and displacement parameters, and an overall scaling factor were varied. A difference Fourier synthesis was performed after each refinement. Peaks from the difference map were used to assemble a new model for phase calculation. The process was repeated until variations in all the parameters had stabilized and the difference map was showing no unaccounted for electron density. For comparison purposes, a conventional R_1 index, based upon F values of all the data, or F values larger than $4\sigma(F_o)$, was also calculated and displayed by XL.

$$R_1 = \frac{\Sigma ||F_o(hkl)| - |F_c(hkl)||}{\Sigma |F_o(hkl)|} \qquad (2\text{-}11)$$

2.2.6 Labelling Experiments

The labelling experiments were performed at Resolution Pharmaceuticals, Inc.[33] The[111] In(111) ($t_{1/2}$=2.806 d) was received from Mallinckrodt (Vancouver, British Columbia) the same day of the experiment. The spots on the Whatman No. 1 paper used for the paper chromatography were analyzed with a Phosphorimager (445 SI, Molecular Dynamics).

2.2.7 Biodistribution Studies

The biodistribution experiments were performed at Resolution Pharmaceuticals Inc.[33] The radioactivity of the excised organs was counted in a Cobra II Auto-Gamma gamma counter (Canberra-Packard Co.; Mississauga, Ontario). The syringes and needles were measured for radioactivity before and after

the injection in the capintec (Capintec Inc., C11; Model CRC-4; Mount Vernon, NY, USA).

Animals

Male Sprague-Dawley rats (weighing approx. 250-300 g, Bausch & Lomb, Charles River, St. Constant, Quebec) were used for the experiments. The animals were allowed to acclimate for at least one week in the animal facility prior to use. They were housed in opaque polycarbonate cages (48 x 27 x 20 cm) with stainless steel lids equipped with hoppers and a water bottle. Each cage contained 3-4 rats. All animals were cared for in accordance with the recommendations of the Canadian Council on Animal Care. The rats were allowed free access to a pelleted, constant formula rodent diet (Rodent Laboratory Chow #5001; Ralston Purina Co.; Leis Feed, Guelph, Ontario). This formula contained 1.0% Ca, 0.61% P, 1.1% K, 0.21% Mg, 0.4% Na, and 0.56% Cl. Fresh water was available *ad libitum*. The bedding supplied was 1/4" corn cob bedding (Leis Feed) and was changed according to the Government of Ontario Animals For Research Act and Canadian Council On Animal Care.

Animal Preparation

The procedures for the inflammation model followed Allelix Animal Care Committee Protocol #28-93. The anesthetic used on the rats was sodium pentobarbital, also known as "Somnotol" supplied by MTC Pharmaceuticals (65 mg/kg, Cambridge, Ontario). Zymosan A was used to inflame the right thigh muscle of each rat. Zymosan A is a cell wall extract from the yeast species *Saccharomyces*

cerevisae (Sigma Chemical Co., St. Louis, MO, USA).

2.2.8 SPECT Imaging

The images were acquired using a Siemens/Searle Digitrac system for the scintillation cameras. The software used was Siemens MicroDelta with a RT-11 operating system. The images were printed using a Mitsubishi Color Video Copy Processor.

Chapter 3

Azapropazone

3.1 Overview of The Chemistry of Azapropazone

Chemical Classification

Azapropazone is one of many anti-inflammatory drugs to emerge from decades of research on substituted 1,2,4-benzotriazine compounds, but is the only drug of its class to become commercially available as a safe and active anti-inflammatory analgesic compound for clinical use.[34] It was developed in the 1960's by the chemist Georg Mixich, who designed azapropazone based on the structure of phenylbutazone, a pyrazolone with anti-inflammatory properties. It was this strategy that lead to the original misclassification of azapropazone itself as a pyrazolone. A re-evaluation of its chemical properties, however, revealed that both oxidation and hydrolysis destroy the pyrazolinedione part of azapropazone without destroying the benzotriazine ring.[35] Azapropazone was therefore officially recategorized as a benzotriazine.

Structural Discrepancies

The structure of azapropazone, or 5-(dimethylamino)-9-methyl-2-propyl-1H-pyrazolo[1,2a][1,2,4]-benzotriazine-1,3(2H)-dione, as found in the Merck Index is shown as **A**.[36] By use of NMR evidence, Fenner and Mixich determined that, in

solution, there is no hydrogen atom at C(2) of the pyrazolone ring, and suggested, therefore, that azapropazone is a zwitterion with the negative charge delocalized

A

B

C

D
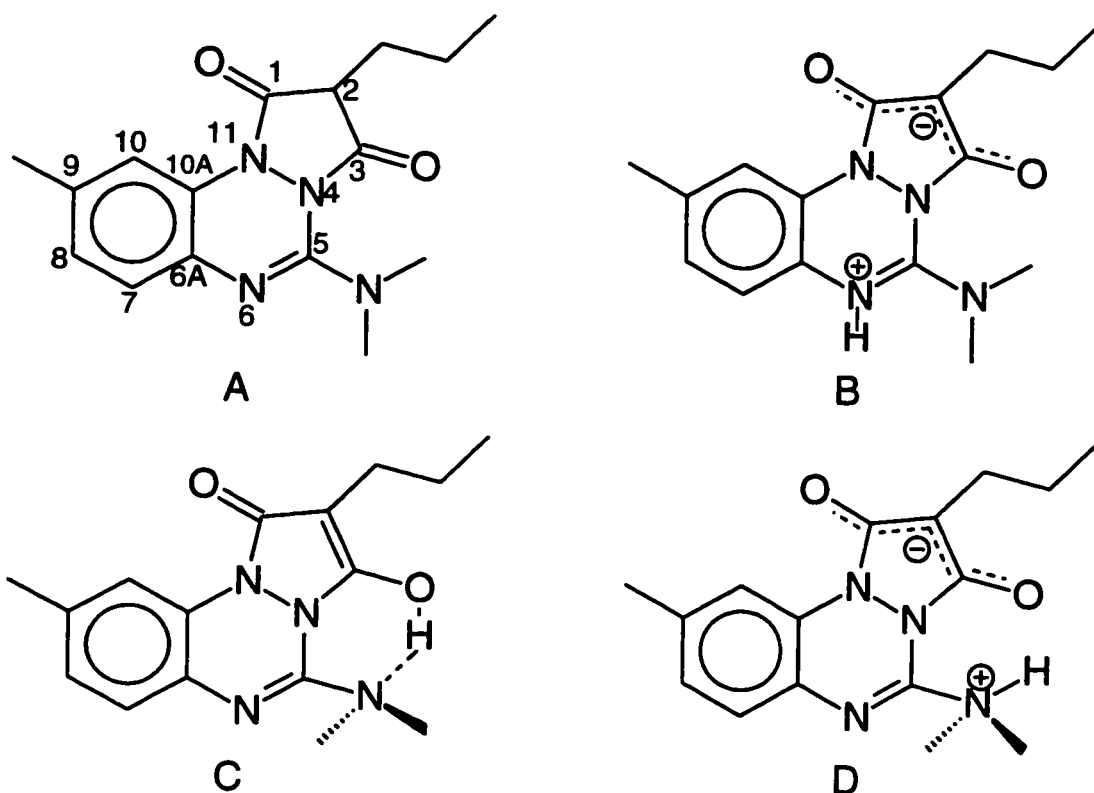
between the two ketone groups and with the proton on N(6) of the benzotriazine group, structure B.[37] Because the proton which is absent from the C(2) position cannot be located directly, since there is rapid exchange, there has been some debate in the literature as to its exact location. Despite references to the work by Fenner and Mixich, Dean interpreted the NMR results as giving evidence of a keto-enol structure with strong hydrogen bonding between the hydroxy proton and the exocyclic dimethylamino group, as seen in structure C.[35] Such an interpretation

seems unlikely since exocyclic amine groups adjacent to ring double bonds tend to show considerable conjugation between the amine and the double bond, with consequent removal of the "lone pair" electron density and shortening of the C(ring)-N distance. In addition, the amine group is then usually nearly coplanar with the double bond system. Despite Dean's argument that there will be a repulsive steric interaction between the methyl group on the amine and the hydroxy group we do not think this would be sufficient to completely overcome the conjugation and thus Dean's postulated structure seems doubtful. Another postulated structure is that shown as structure D, where the hydrogen atom is directly bonded to the nitrogen atom of the dimethylamino group.[35] For reasons already given, this structure also seems unlikely.

The NMR spectra show that the peak from the aromatic proton at C(10) is pushed downfield about 1 ppm from the other aromatic protons because of the interaction of the proton with the deshielding cone of the carbonyl group at C(1). For this reason, and because of the delocalization in the molecule, Fenner and Mixich stated that the three rings of azapropazone form a completely planar tricyclic system.[37] We were not convinced of this because, while there is considerable delocalization in the benzotriazine system and the pyrazolidine ring, it does not extend to the N-N region and thus there seems to be no reason for the tricyclic system to be planar. Further, Walker assumed that, despite the solution results, the solid compound existed in the diketone form, although no rationale was given.[34]

The conflicting views have led us to solve the crystal structure of azapropazone.[38] The structure is presented here in its anhydrous and dihydrate

form.

3.2 Results and Discussion

The molecule of azapropazone is a zwitterion and, as postulated by Fenner and Mixich, the proton from C(2) appears at the N(6) position. As can be seen from **Figure 3.2**, the tricyclic part of the molecule is *not* planar, which renders the molecule chiral in the solid state. The nonplanarity of the tricyclic system is best exemplified by the dihedral angles between the best planes through each of the rings, where the benzene ring is ring 1, the triazine ring is ring 2, and the pyrazolidine ring is ring 3. These values are as follows: rings 1-2, 11.7(7)°; rings 2-3, 32.9(7)°; rings 1-3, 44.5(7)°. The nonplanarity at N(11) is almost certainly caused by the repulsive interaction of the methyl groups on the exocyclic amine with O(3). The effects of this repulsion, which is illustrated by the nonzero dihedral angle between the atoms of the amine group (C(51)N(5)C(52)) and N(4)C(5)N(6), 24.1(8)°), are transmitted through the rigid parts of the molecule where there is significant π bonding. Normally in systems such as this, N(11) would be nearly coplanar with the three atoms attached to it, but N(11) is 0.395 Å out of the C(10A)C(1)N(4) plane. The nonplanarity is further reflected on two of the bond angles of 112.0(3)° for C(10A)N(11)N(4) and 104.8(3)° for C(1)N(11)N(4), which are substantially reduced from the normal 120°.

The downfield shift of the aromatic proton at C(10) relative to the other aromatic protons, mentioned above, does not present a problem. The solid state structure shows that the proton is still close enough to the deshielding cone of the
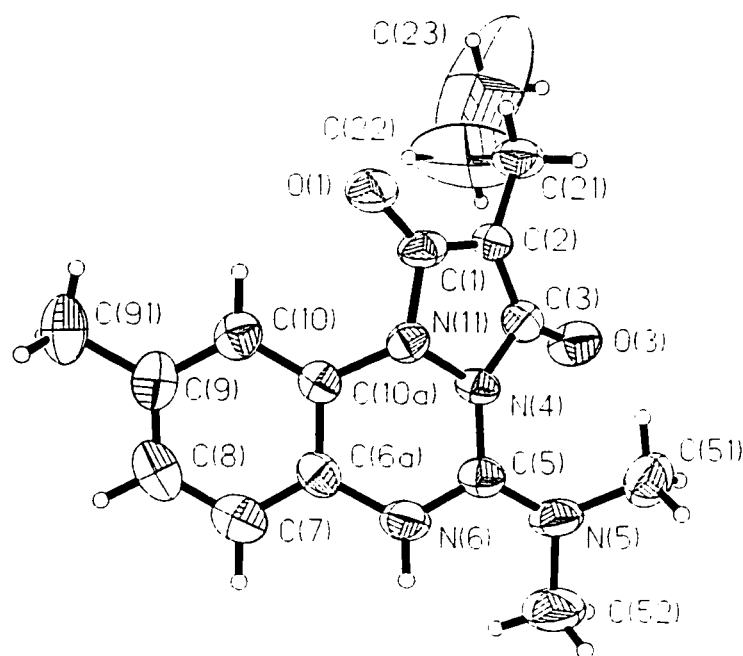
Figure 3.1 The molecule of azapropazone (I) with atom numbering. Displacement ellipsoids are drawn at 50% probability level.
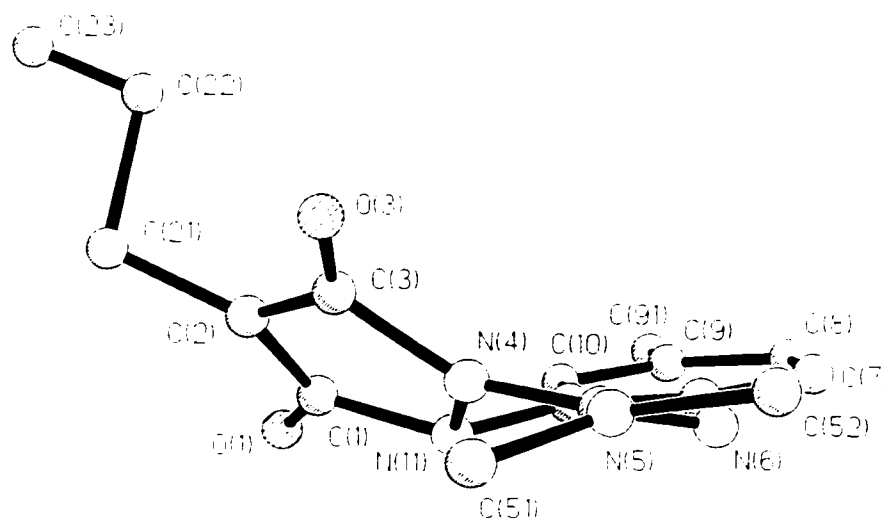
Figure 3.2 The atoms in **I** viewed along N(5)C(5) and showing the nonplanarity of the tricyclic system. The atoms are drawn as rigid spheres and the hydrogen atoms have been omitted for clarity.
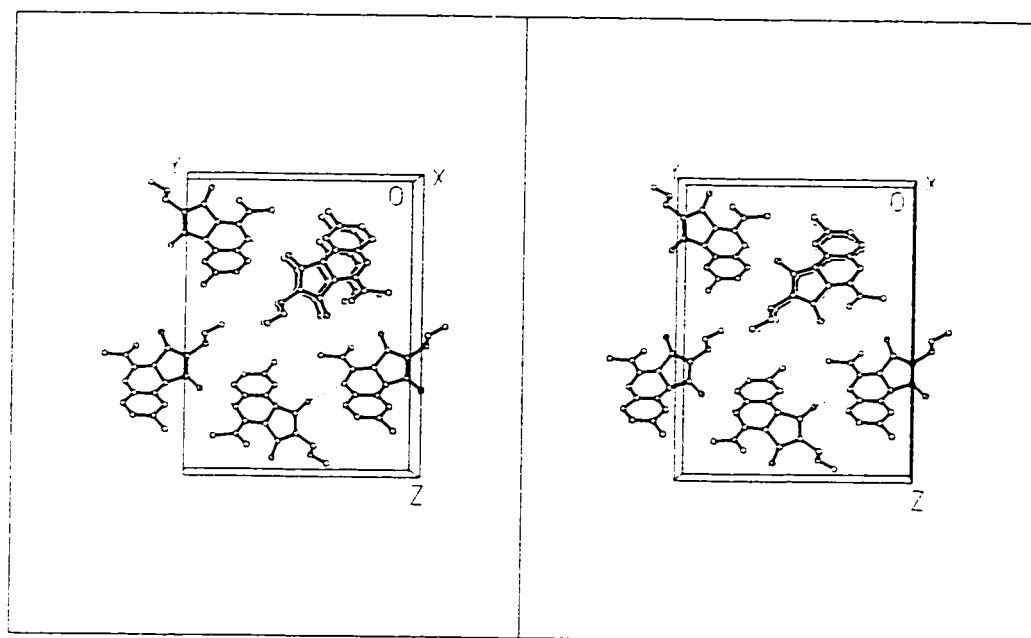
Figure 3.3 A stereoview of the packing of azapropazone within the unit cell. Hydrogen bonds are given as broken lines.

carbonyl group C(1)O(1) to allow for the downfield shift effect observed in the NMR spectra, and the relative positions of these two atoms do not shift significantly as inversion about N(11) takes place.

A legitimate question is whether the solid state structure is relevant to solution conditions, since the NMR spectra show that the methyl groups of the exocyclic dimethylamino group are equivalent, whereas the structure shows that this should not be so. In addition, one cannot locate the proton in solution because of exchange, so there may some doubt as to whether it is still attached to N(6). The packing of the unit cell (**Figure 3.3**) addresses the second question. The proton attached to N(6) (which was located from the difference map) forms quite a strong hydrogen bond to O(1) of an adjacent molecule (N(6)...O(1), 2.759(6)Å). Thus, the proton could easily transfer to the oxygen atom if this was energetically preferable and the proton is not kept at N(6) because of steric hindrance. The crystal packing consists of spiral chains of molecules in the *b* direction, each molecule bound to the next by the N(6)--H(6)...O(1) hydrogen bond. In the *a* direction translationally equivalent molecules are adjacent and stacked so that there may be some weak π-π interactions* but in the *c* direction the interactions are of a van der Waals type.

The equivalence of the methyl protons in the NMR spectrum could be because the ring system is rigidly planar with the dimethylamino group at right angles to this plane or the structure shown is the limiting structure in solution and

* D.P. Santry has calculated (personal communication) that interactions between the π systems of aryl rings will be 6-9 kcal mol^{-1} if there is complete overlap of the rings and they are 3.4 Å apart. The variation of the values is caused by varying the orientation of the rings.

the equivalence is caused by a rapid inversion of the molecule to the other enantiomer, with a consequent rotation of the dimethylamino group about C(5)N(5) by 310° when C(51) will be swapped with C(52).

The latter model was tested by measuring the NMR spectra at various temperatures and found to be correct. As can be seen in **Figure 3.4**, the peak caused by the dimethylamino group is still a singlet at -40°C, but by -85°C it has been resolved into two peaks, corresponding to the two inequivalent methyl groups seen in the crystal structure. The variable temperature studies showed that the coalescence temperature for the two peaks was -54 ± 1°C and calculation showed that this corresponded to $\Delta G^{\ddagger}= 44.9$ kJ mol^{-1} for the exchange of the dimethylamino methyl groups. This barrier was later retested with a better line-fitting technique, and was found to be 40 kJ mol^{-1}.[39]

The structure of azapropazone dihydrate (**I·2H₂O**) is shown in **Figure 3.5**. The drug observed here is a zwitterion, with the proton on N(6) and the negative charge delocalized over the diketone system. The conformation is very similar to that observed for the anhydrous molecule; bond lengths are very similar, as are the corresponding angles. The only significant differences in bond lengths are in C(8)-C(9) (1.363(8) Å vs. 1.396(3) Å, 3.9σ), N(4)-C(3) (1.435(2) Å vs. 1.467(6) Å, 5.1σ) and in the exocyclic propyl group. This last is because, in the compound reported here, the propyl group does not show the marked disorder observed in **I**. The associated angles are also significantly different. Within the tricyclic fragment the only angle that is significantly different is C(5)-N(6)-C(6A) (120.1(2)° vs. 121.9(4)°,
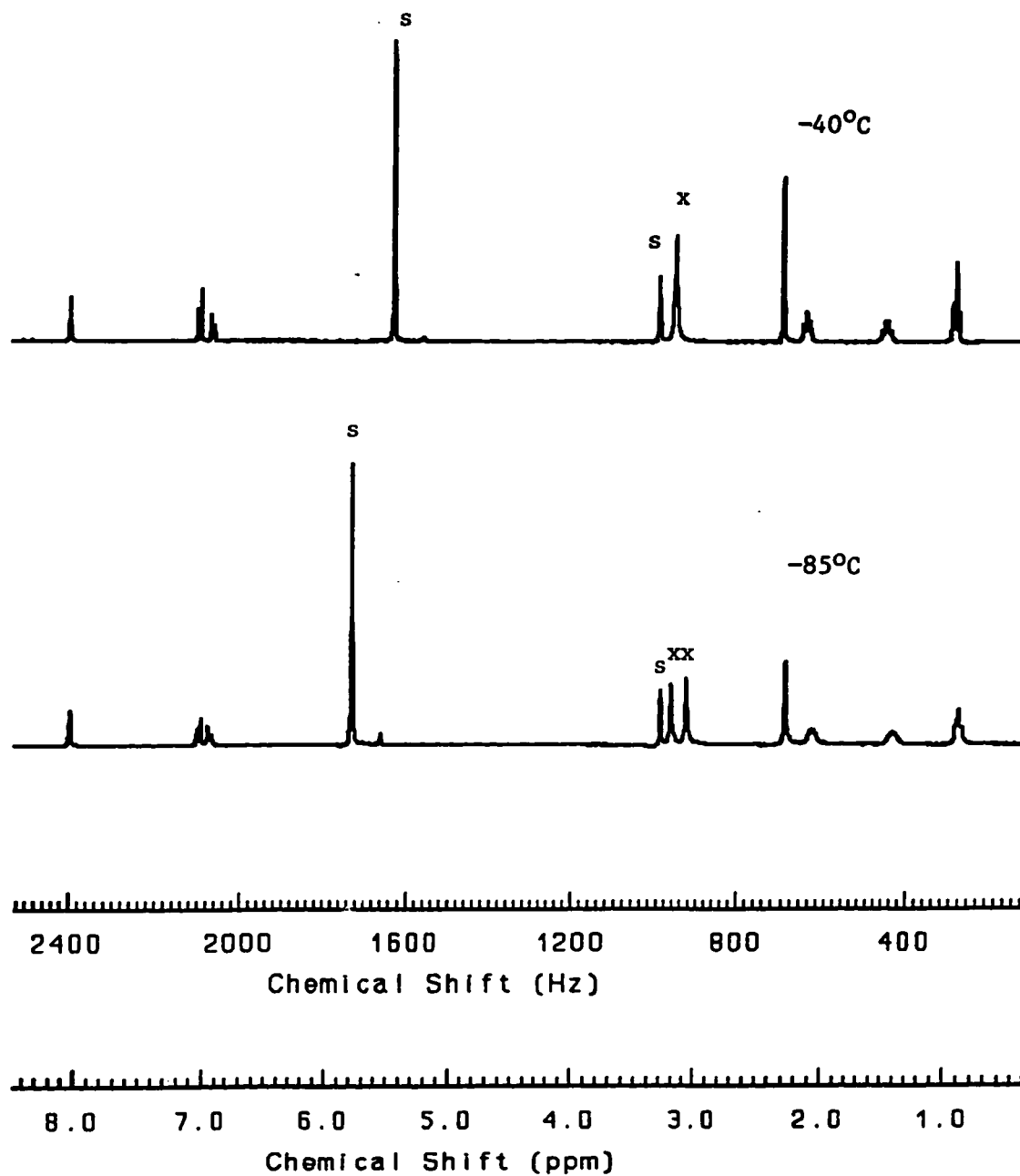
Figure 3.4 The proton NMR spectra of azapropazone (I) at -40°C and -85°C, which show the resolution of the peak caused by the methyl groups on the exocyclic amine group (x) into two peaks at the lower temperature. The solvent peaks are indicated by s (CD₃OD, 300 MHz).
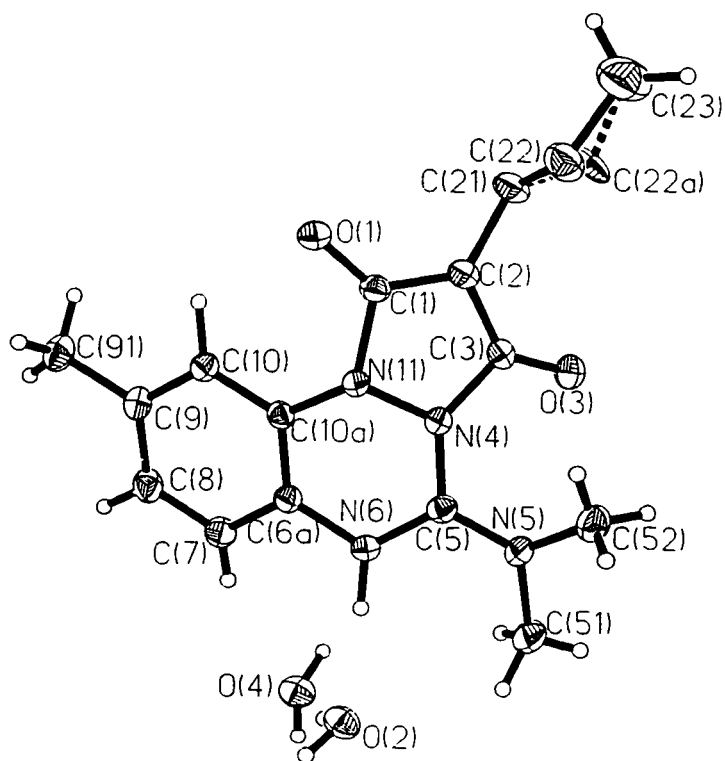
Figure 3.5 The atomic structure of I·H₂O with atom numbering. The displacement ellipsoids are drawn at the 30% probability level.
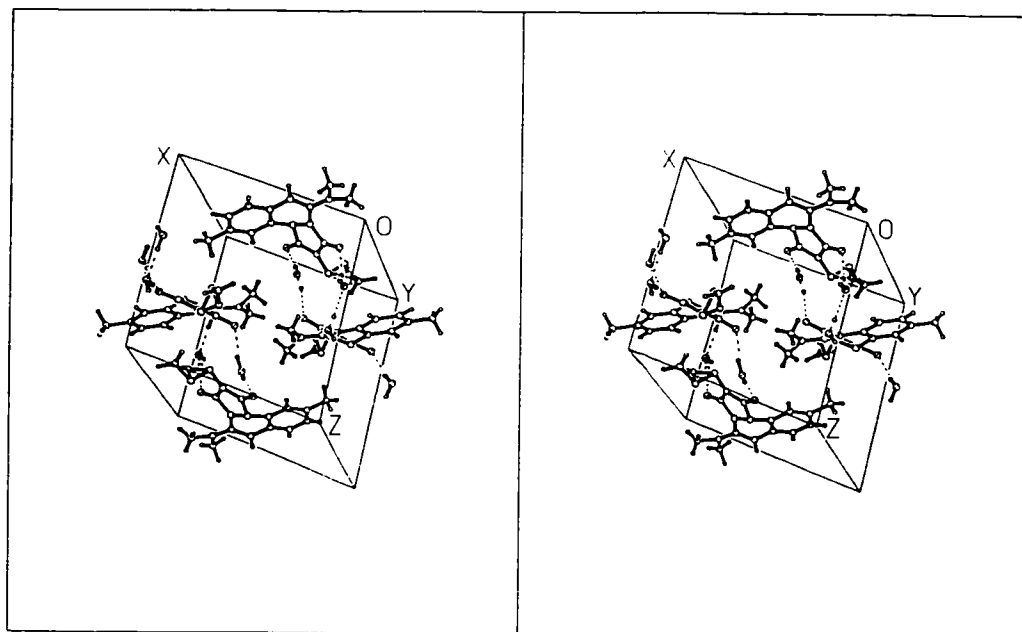
Figure 3.6 A stereoview of the packing of I·H₂O within the unit cell.

4.0 σ).

The energy to change torsional angles is much less than that required for bond lengths and angles, but even here the changes are not great. The prime changes are caused by the position of the propyl group and C(91) and N(4). Ring 1 (the benzo group) is planar and C(91) lies in this plane, although N(6) (-0.028(3) Å) and N(11) (-0.034(3) Å) lie significantly out of the ring plane. The triazine ring is non-planar and adopts a skewed boat conformation. The atoms N(11), C(10A), C(6A), and N(6) are planar with C(5) 0.406(3) Å and N(4) 0.708(3) Å out of the plane, very close to the values observed for I. Ring 3, the pyrazolidine ring, is roughly planar (maximum deviation, N(11), 0.035(1) Å). The inter-ring dihedral angles are 1-2, 12.2(1), 1-3, 46.1(1), 2-3, 34.0(1), very close to those observed for I.

The molecule I·2H$_2$O is packed as a racemic mixture, in contrast to I, which is enantiomerically pure. The packing within the unit cell (Figure 3.3) is dominated by the N(6)...O(2)(...O(3))...O(4)(...O(3))...O(1) hydrogen bonding network. Molecules are arranged in pairs related by the inversion centre at ½, 0, ½ so as to maximize π-π interactions. These pairs are also held together by the hydrogen bonding network that also binds them to adjacent pairs, to form layers which are parallel to the {101} planes. Between these layers, the interactions are all of a van der Waals type.

The drug could exist as an anion, cation, or zwitterion depending on the respective acidity or basicity of the anionic and cationic groups on the molecule.

The zwitterion is probably more stable because of the extensive delocalization of the charges.

Recently, Testa[40] has looked further into the zwitterionic nature of azapropazone to shed some light on the molecular and distribution equilibria of the drug. Studies[41] on another zwitterionic NSAID, piroxicam, have already shown that it is difficult to obtain a clear understanding of the partition behaviour of a zwitterionic molecule. Testa used a variety of experimental and computational techniques to study the molecular structure of azapropazone in the gas phase and non-protic polar solvents, protonation/deprotonation equilibria, tautomerism, and pH-lipophilicity profiles. He determined that at pHs below 6.3, the drug exits as a zwitterion that is lipophilic enough to permeate the gastric mucosa, and thus reduce gastric toxicity. At the physiological pH of 7.4, there would be zwitterionic and anionic forms of azapropazone. Despite the slight lipophilic nature of azapropazone, it is still predominately eliminated renally.

In conclusion, we have shown by single crystal X-ray crystallography and NMR spectroscopy that the postulated structure for azapropazone is wrong. These results prompted us to reexamine the products of other reactions of azapropazone, and the results are presented in the next chapter.

3.3 Experiments

Commercial azapropazone is usually a very pale cream colour, and consists of finely divided crystals plus larger aggregates. The pale cream colour is caused by the presence of about 0.01% of the molecule **IV (Chapter 4)** which is a very

intense buttercup-yellow colour. A proportion of only 0.005% is needed for visual detection.[34] The intensity of the yellow colour increases under prolonged exposure to light. Azapropazone can be purified through recrystallization, and was done so accordingly.

Sample Preparation and Characterization

Anhydrous Azapropazone (I)

Azapropazone was kindly provided by Siegfried Pharma AG, Zotingen, Switzerland, as a yellow powder and was recrystallized from dimethylformamide to give colourless needles, mp 244-247°C (lit. 247-248°C)[37]. ^{1}H NMR (200 MHz in CD$_3$OD at 25°C) δ : 0.91 (3H, t, J$_{23,22}$=7.3 Hz, -CH$_2$CH$_2$CH$_3$), 1.49 (2H, qt, J$_{22,23}$=7.3 Hz, J$_{22,21}$=7.4 Hz, -CH$_2$CH$_2$CH$_3$), 2.14 (2H, t, J$_{21,22}$=7.4 Hz, -CH$_2$CH$_2$CH$_3$), 2.29 (3H, s, -CH$_3$ aromatic), 3.19 (6H, s, -N(CH$_3$)$_2$), 6.89 (1H, d, J$_{8,7}$=8.3 Hz, aromatic), 7.00 (1H, d, J$_{7,8}$=8.3 Hz, aromatic), 8.04 (1H, s, aromatic). ^{13}C NMR (125 MHz in CD$_3$OD at 25°C) δ: 13.78 (C-23), 20.96 (aromatic-CH$_3$), 21.76 (C-22), 23.29 (C-21), 40.71 (N(CH$_3$)$_2$), 80.34 (C-2), 113.66 (C-7), 117.38 (C-8), 122.11 (C-10a), 123.64 (C-10), 134.69 (C-9), 135.36 (C-6a), 146.09 (C-5), 162.96 (C-1), 169.92 (C-3). ^{1}H NMR (300 MHz in CD$_3$OD) δ : at -40°C, 3.17 (6H, s, -N(CH$_3$)$_2$); at -85°C, 3.08 (3H, s, -N(CH$_3$)), 3.21 (3H, s, -N(CH$_3$)). EIMS:(%, intensity), 299 (100, M$^+$), 188 (30).

Azapropazone Dihydrate (I·2H$_2$O)

Azapropazone was recrystallized from 70% methanol / 30% water to give crystals suitable for single crystal X-ray diffractometry. During the melting point determination, a decomposition was noted from 104-107°C which corresponded to

the loss of lattice water. The molecule proceeded to melt at 244-248°C (lit. 247-248°C). The ^{1}H NMR spectrum of the molecule was the same as that recorded for the anhydrous form.

Crystal Structures

Anhydrous Azapropazone (I)

A crystal was selected after examination for clarity and sharp extinction with a polarizing microscope, and mounted on a glass fibre with epoxy glue. Unit cell determination and intensity data collection were performed on a Rigaku AFC6-R diffractometer with monochromatized Cu-Kα (λ = 1.54178 Å). The unit cell was obtained by least-squares refinements of the angular coordinates of 24 reflections with θ from 25.0° to 37.4°. An absorption correction was made with DIFABS.[29] The structure was solved by direct methods and refined on F by full-matrix least squares. Hydrogen atoms adjacent to atoms in the tricyclic ring system were found from the difference map, but were not refined. Hydrogen atoms in the exocyclic alkyl groups were placed in calculated positions and rode on the atoms to which they were attached. Temperature factors of non-hydrogen atoms were refined anisotropically, and those of hydrogen atoms were not refined. The details of data acquisition and treatment are given in **Table 3.1**. The atomic coordinates and isotropic temperature factors can be found in **Table 3.2** and interatomic distances and angles are given in **Table 3.3**. The molecule is shown in **Figures 3.1** and **3.2**, and the packing diagrams are shown in **Figure 3.3**. The compound presented difficulty in the refinement of atoms C(22) and C(23), which were clearly disordered.

Many different refinements were tried, with partial occupancies of multiple sites or restraints on bond lengths, but none were satisfactory or better than the results presented here.

Azapropazone Dihydrate (I·2H₂O)

A crystal was selected after examination for clarity and sharp extinction with a polarizing microscope, and mounted on a glass fibre with epoxy glue. Unit cell determination and intensity data collection were performed on a Siemens P4 diffractometer with monochromatized Mo-Kα ($\lambda = 0.71073$ Å) radiation. The unit cell was obtained by least-squares refinements of the angular coordinates of 38 reflections with θ from 14.79 to 24.99°. A semi-empirical ψ-scan absorption correction was made. The structure was solved by direct methods and refined on F^2 by full-matrix least squares. Hydrogen atoms adjacent to atoms in the tricyclic ring system were found from the difference map, but were not refined. Hydrogen atoms in the exocyclic alkyl groups were placed in calculated positions and rode on the atoms to which they were attached. Temperature factors of non-hydrogen atoms were refined anisotropically, and those of hydrogen atoms were not refined. The details of data acquisition and treatment are given in **Table 3.4**. The atomic coordinates and isotropic temperature factors can be found in **Table 3.5** and interatomic distances and angles are given in **Table 3.6**. The molecule is shown in **Figure 3.5**, and the packing diagrams are shown in **Figure 3.6**.

Variable Temperature NMR Study

Low-temperature NMR data were obtained with use of a Bruker AC-300

spectrometer. The solvent was CD_3OD which provided the deuterium lock signal. Data were acquired in 8 scans at a spectral width of 2.994 kHz (16K, 0.3655 Hz/data point). The spectra were recorded every 5° from -85°C to -65°C and -50°C to -40°C and every 1° from -65°C to -50°C.

Table 3.1 Crystallographic data for Azapropazone (I)

Formula	$C_{16}H_{20}N_4O_2$
Formula weight	300.4
Crystal colour, shape, size (mm)	colourless needle, 0.2 x 0.2 x 0.2
Space group	$P2_12_12_1$
λ (Å)	1.54178
Unit cell parameters (Å)	a = 5.570(1)
	b = 14.593(3)
	c = 19.270 (4)
Volume (Å^3)	1566.3(5)
Z	4
D_{calc} (g/cm^3)	1.274
Index ranges	$-6 \leq h \leq 6, 0 \leq k \leq 16, 0 \leq l \leq 21$
Max 2θ (°)	120
Temperature (°C)	25
Absorption coeffient (mm^{-1})	0.703
$F(000)$	640
Transmission factors (range)	0.681,1.00
Reflections collected	2689
Independent reflections	2316 (R_{int} = 0.0161)
Reflections used	2316
No. Of parameters refined	201
Final R indices	
R_1	0.0950
wR	0.0563
Goodness-of-fit, S	2.68
Largest Δ/σ	0.210
Mean Δ/σ	0.053
Data:parameter ratio	11.5:1
Largest difference peak (e Å^{-3})	0.75
Largest difference hole (e Å^{-3})	-0.89

Table 3.2   Atomic coordinates (x10⁴) and equivalent isotropic displacement
coefficients (Å²x10³) for I.

	x	y	z	U_{eq}
C(1)	409(9)	5069(3)	3143(3)	44(2)
C(2)	-70(9)	5098(3)	3853(2)	42(2)
C(3)	-567(9)	4242(3)	4113(2)	44(2)
N(4)	-606(7)	3640(2)	3504(2)	40(1)
C(5)	-1040(10)	2725(3)	3426(2)	44(2)
N(6)	146(9)	2305(3)	2931(2)	51(2)
C(6A)	2039(10)	2746(3)	2557(2)	46(2)
C(7)	3774(12)	2252(4)	2209(3)	63(2)
C(8)	5510(12)	2727(4)	1833(3)	65(2)
C(9)	5559(10)	3665(4)	1810(3)	55(2)
C(10)	3844(10)	4152(3)	2179(3)	50(2)
C(10A)	2058(9)	3705(3)	2549(2)	37(2)
N(11)	158(7)	4149(2)	2904(2)	40(1)
O(1)	992(7)	5681(2)	2724(2)	59(1)
C(21)	207(11)	5938(3)	4290(3)	60(2)
O(3)	-970(8)	3940(2)	4692(2)	58(1)
N(5)	-2535(10)	2303(3)	3842(2)	57(2)
C(51)	-4602(11)	2754(4)	4175(3)	68(2)
C(52)	-2418(15)	1299(4)	3910(3)	98(3)
C(91)	7384(11)	4177(5)	1388(3)	74(3)
C(22)	2829(28)	5883(7)	4658(6)	205(8)
C(23)	3106(29)	6612(8)	4965(6)	373(15)

* Equivalent isotropic U_{eq} defined as one third of the trace of the orthogonalized
U_{ij} tensor.

Table 3.3 Interatomic distances (Å) and angles(°) for I.

C(1)-C(2)	1.398(7)	C(2)-C(3)	1.369(6)
C(3)-N(4)	1.467(6)	N(4)-C(5)	1.366(6)
C(5)-N(6)	1.317(6)	N(6)-C(6A)	1.426(7)
C(6A)-C(7)	1.383(8)	C(7)-C(8)	1.386(8)
C(8)-C(9)	1.363(8)	C(9)-C(10)	1.398(7)
C(10)-C(10A)	1.382(7)	C(10A)-N(11)	1.418(6)
N(11)-C(1)	1.428(6)	N(4)-N(11)	1.435(5)
C(6A)-C(10A)	1.400(7)	C(1)-O(1)	1.244(6)
C(2)-C(21)	1.496(7)	C(21)-C(22)	1.660(16)
C(22)-C(23)	1.254(16)	C(3)-O(3)	1.231(6)
C(5)-N(5)	1.313(7)	N(5)-C(51)	1.472(8)
N(5)-C(52)	1.476(7)	C(9)-C(91)	1.508(8)

N(11)-C(1)-C(2)	108.7(4)	C(1)-C(2)-C(3)	11.6(4)
C(2)-C(3)-N(4)	105.1(4)	N(11)-N(4)-C(5)	118.3(3)
N(4)-C(5)-N(6)	116.2(4)	C(5)-N(6)-C(6A)	121.9(4)
N(6)-C(6A)-C(7)	121.7(4)	N(6)-C(6A)-C(10A)	117.8(4)
C(10A)-C(6A)-C(7)	120.5(5)	C(6A)-C(7)-C(8)	118.7(5)
C(7)-C(8)-C(9)	121.9(6)	C(8)-C(9)-C(10)	118.5(5)
C(9)-C(10)-C(10A)	120.8(5)	C(10)-C(10A)-N(11)	124.6(4)
C(10)-C(10A)-C(6A)	119.2(4)	C(6A)-C(10A)-N(11)	116.2(4)
C(10A)N(11)C(1)	120.7(4)	C(10A)N(11)N(4)	112.0(3)
N(4)N(11)C(1)	105.1(3)	N(11)C(1)O(1)	119.3(4)
O(1)C(1)C(2)	132.0(4)	C(1)C(2)C(21)	123.9(4)
C(21)C(2)C(3)	124.1(4)	C(2)C(21)C(22)	105.9(5)
C(21)C(22)C(23)	103.8(11)	O(3)C(3)N(4)	120.8(4)
N(5)C(5)N(6)	123.2(4)	C(5)N(5)C(52)	119.5(5)
C(8)C(9)C(91)	122.4(5)	C(2)C(3)O(3)	134.1(5)
N(4)C(5)N(5)	120.6(4)	C(5)N(5)C(51)	123.3(4)
C(51)N(5)C(52)	116.3(5)	C(91)C(9)C(10)	119.2(5)

Table 3.4 Crystallographic data for Azapropazone Dihydrate($I \cdot 2H_2O$)

Formula	$C_{16}H_{20}N_4O_2 \cdot 2H_2O$
Formula weight	336.4
Crystal colour, shape, size (mm)	colourless fragment, 0.5 x 0.3 x 0.2
Space group	$P2_1/n$
λ (Å)	0.71073
Unit cell parameters (Å)	a = 12.446(1)
	b = 11.367(1)
	c = 12.649(1)
	β = 104.45(1)°
Volume (Å^3)	1732.9(2)
Z	4
D_{calc} / D_{meas} (g/cm^3)	1.289 / 1.27(3)
Index ranges	$-1 \leq h \leq 17$, $-1 \leq k \leq 15$, $-17 \leq l \leq 17$
Max 2θ (°)	60
Temperature (°C)	25
Absorption coeffient (mm^{-1})	0.094
Transmission factors (range)	0.932, 0.954
F(000)	720
Reflections collected	5273
Independent reflections	4244 (R_{int} = 0.0222)
Reflections observed	3197 [$I > 2\sigma$ (I)]
No. Of parameters refined	227
Final R indices [I>2σ (I)]	R_1=0.0684, wR_2=0.2075
Final R indices (all data)	R_1=0.0880, wR_2=0.2299
Goodness-of-fit, S (all data)	1.091
Largest Δ/σ	-1.253
Mean Δ/σ	0.013
Data:parameter ratio	18.7:1
Largest difference peak (e Å^{-3})	0.63
Largest difference hole (e Å^{-3})	-0.44

Table 3.5   Atomic coordinates (x 10^4) and equivalent isotropic
displacement parameters (Å^2 x 10^3) for I·H_2O.

	x	y	z	U_{eq}
C(1)	1146(2)	7809(2)	3639(2)	34(1)
O(1)	366(1)	8541(1)	3478(2)	44(1)
C(2)	2216(2)	7875(2)	3494(2)	38(1)
C(21)	2751(3)	8931(2)	3127(3)	57(1)
C(22)[a]	3256(3)	9771(3)	4174(3)	59(1)
C(22A)[a]	3663(16)	9447(14)	3608(15)	50(4)
C(23A)	3896(4)	10766(4)	3887(4)	95(1)
C(3)	2778(2)	6810(2)	3793(2)	35(1)
O(3)	3703(2)	6450(2)	3761(1)	46(1)
N(4)	2027(2)	6093(2)	4211(2)	36(1)
C(5)	2144(2)	4996(2)	4649(2)	34(1)
N(5)	3123(2)	4649(2)	5245(2)	41(1)
C(51)	3360(3)	3405(2)	5464(3)	61(1)
C(52)	3918(2)	5464(2)	5908(2)	51(1)
N(6)	1245(2)	4318(2)	4438(2)	36(1)
C(6A)	243(2)	4713(2)	3713(2)	34(1)
C(7)	-585(2)	3923(2)	3230(2)	44(1)
C(8)	-1557(2)	4332(2)	2549(2)	46(1)
C(9)	-1728(2)	5534(2)	2330(2)	39(1)
C(91)	-2781(2)	5978(3)	1591(2)	52(1)
C(10)	-885(2)	6318(2)	2816(2)	36(1)
C(10A)	92(2)	5915(2)	3508(2)	31(1)
N(11)	979(2)	6663(2)	4062(1)	33(1)
O(2)	1087(2)	2013(2)	5163(2)	48(1)
O(4)	520(2)	977(2)	3144(1)	50(1)

*Equivalent isotropic U is defined as one third of the trace of the orthogonalized U_{ij} tensor.

[a]Occupancies of the constrained atoms C(22) and C(22A) were set at 0.84 and 0.16 respectively.

Table 3.6   Bond lengths [Å] and angles [°] for I·H₂O.

C(1)-O(1)	1.256(3)	C(1)-C(2)	1.390(4)
C(1)-N(11)	1.444(3)	C(2)-C(3)	1.402(3)
C(2)-C(21)	1.501(3)	C(21)-C(22A)	1.29(2)
C(21)-C(22)	1.626(5)	C(22)-C(22A)	1.04(2)
C(22)-C(23)	1.480(5)	C(22A)-C(23)	1.55(2)
C(3)-O(3)	1.233(3)	C(3)-N(4)	1.436(3)
N(4)-C(5)	1.358(3)	N(4)-N(11)	1.427(3)
C(5)-N(5)	1.323(3)	C(5)-N(6)	1.330(3)
N(5)-C(51)	1.457(3)	N(5)-C(52)	1.458(3)
N(6)-C(6A)	1.423(3)	C(6A)-C(7)	1.388(3)
C(6A)-C(10A)	1.395(3)	C(7)-C(8)	1.379(4)
C(8)-C(9)	1.399(3)	C(9)-C(10)	1.397(3)
C(9)-C(91)	1.495(3)	C(10)-C(10A)	1.387(3)
C(10A)-N(11)	1.430(3)		

O(1)-C(1)-C(2)	132.1(2)	O(1)-C(1)-N(11)	118.7(2)
C(2)-C(1)-N(11)	109.2(2)	C(1)-C(2)-C(3)	110.3(2)
C(1)-C(2)-C(21)	126.6(2)	C(3)-C(2)-C(21)	123.0(2)
C(22A)-C(21)-C(2)	128.7(8)	C(22A)-C(21)-C(22)	39.8(7)
C(2)-C(21)-C(22)	109.2(2)	C(22A)-C(22)-C(23)	73.6(8)
C(22A)-C(22)-C(21)	52.3(1)	C(23A)-C(22)-C(21)	111.8(3)
C(22)-C(22A)-C(21)	87.8(12)	C(22)-C(22A)-C(23)	66.2(9)
C(21)-C(22A)-C(23)	130.0(2)	C(22)-C(23)-C(22A)	40.1(6)
O(3)-C(3)-C(2)	133.2(2)	O(3)-C(3)-N(4)	121.5(2)
C(2)-C(3)-N(4)	105.3(2)	C(5)-N(4)-N(11)	118.2(2)
C(5)-N(4)-C(3)	131.2(2)	N(11)-N(4)-C(3)	110.6(2)
N(5)-C(5)-N(6)	123.5(2)	N(5)-C(5)-N(4)	119.7(2)
N(6)-C(5)-N(4)	116.8(2)	C(5)-N(5)-C(51)	120.8(2)
C(5)-N(5)-C(52)	122.3(2)	C(51)-N(5)-C(52)	115.5(2)
C(5)-N(6)-C(6A)	120.3(2)	C(7)-C(6A)-C(10A)	120.0(2)
C(7)-C(6A)-N(6)	121.0(2)	C(10A)-C(6A)-N(6)	119.0(2)
C(8)-C(7)-C(6A)	119.8(2)	C(7)-C(8)-C(9)	121.3(2)
C(10)-C(9)-C(8)	118.4(2)	C(10)-C(9)-C(91)	120.3(2)

Table 3.6 Bond lengths [Å] and angles [°] for I·H₂O. (Cont'd)

C(8)-C(9)-C(91)	121.3(2)	C(10A)-C(10)-C(9)	120.7(2)
C(10)-C(10A)-C(6A)	119.8(2)	C(10)-C(10A)-N(11)	124.1(2)
C(6A)-C(10A)-N(11)	116.0(2)	N(4)-N(11)-C(10A)	111.3(2)
N(4)-N(11)-C(1)	104.3(2)	C(10A)-N(11)-C(1)	121.3(2)

Chapter 4

Derivatives of Azapropazone

4.1 Overview

The determination of the correct structure of azapropazone led to the examination of some of its reaction products. Mixich reported the synthesis and ¹H NMR characterization of a series of azapropazone derivatives.[42] Much of the chemistry of azapropazone depends on the fact that it contains a 3,5-dioxo-pyrazolidine ring fused to, and therefore part of, the 1,2,4-benzotriazine ring structure. The molecule is easily attacked on the pyrazolidine ring and somewhat less easily on the dimethylamino group, but it is very resistant to attack on the benzotriazine structure.

The compounds presented in this chapter were prepared according to the methods of Mixich, followed by recrystallization and X-ray crystal structure determination. The structures allowed us to see whether the delocalization and steric effects that were observed for azapropazone were present in the derivatives. They also confirmed whether the structures proposed by Mixich agreed with the actual structure.

In addition to the structural studies, variable temperature ¹H NMR was used to determine the energy barrier for the rotation of the dimethylamino group for molecule IV.
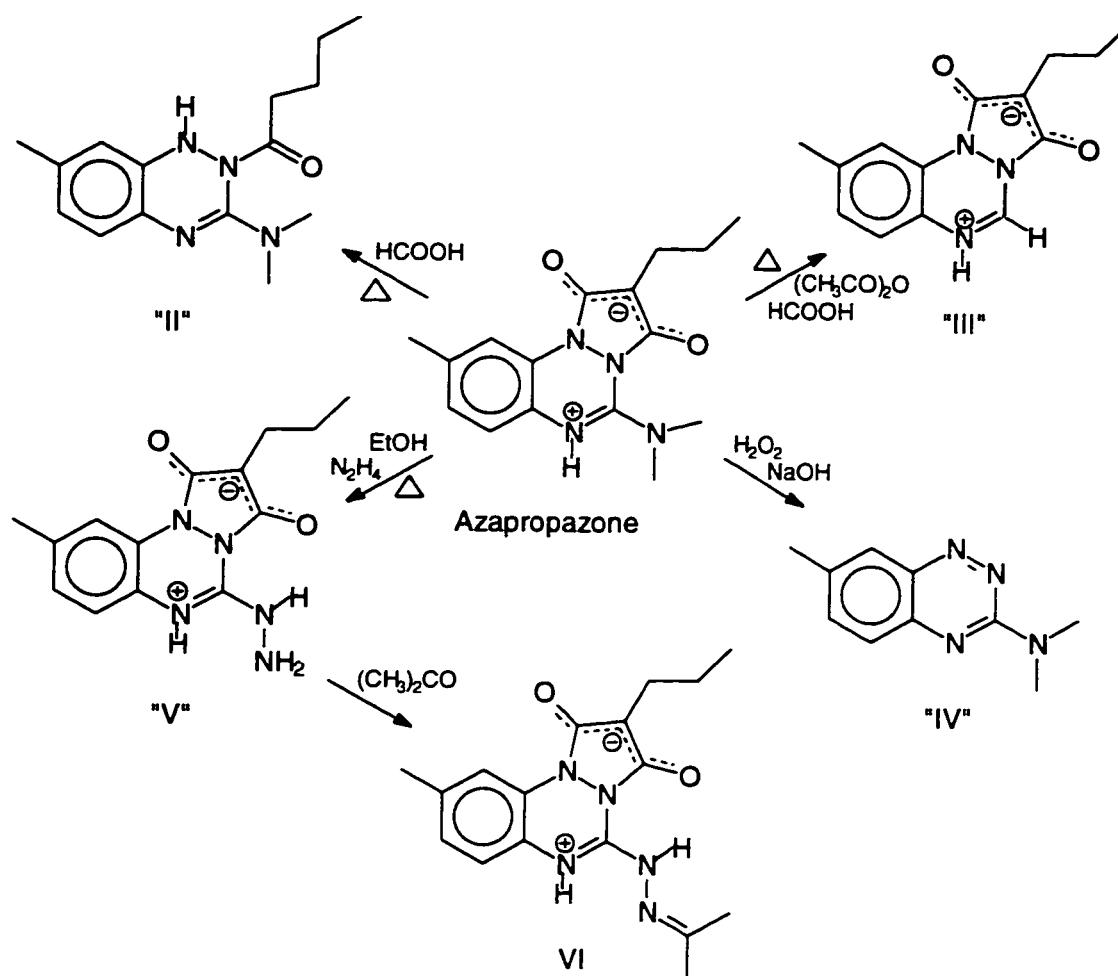
Figure 4.1 A schematic diagram of the structures of some azapropazone derivatives as proposed by Mixich ("II" to V), and a new compound (VI), and the reagents involved.

The reaction pathways and the structures of the reaction products proposed by Mixich can be seen in **Figure 4.1**. The incorrect structures are labelled with Roman numerals in quotation marks. The correct structures of the products presented in this chapter are labelled with the same Roman numeral without quotation marks. Compound **VI** is the reaction product of **V** with acetone.

4.2 Results and Discussion

The structures presented in this chapter are the products of various reactions performed on azapropazone. They allowed the examination of the structural features of a set of related molecules.

The structure of **II** is of interest because the strain caused by the interaction of the methyl group located on the exocyclic amine with the ketone group, as seen in azapropazone, has been removed. On the basis of NMR results, Mixich suggested that the pyrazolidine ring opened at N(11). The NMR spectrum, as seen in **Figure 4.4**, shows that the aromatic proton at C(10) is downfield about 0.5 ppm from the other aromatic protons, which should not be the case if the carbonyl group is no longer proximate. The determination of the crystal structure explained the NMR spectrum. The molecule is shown in **Figure 4.1** and **Figure 4.2**. The structure shows that the pyrazolidine ring opened not at N(11) but at N(4). As a result, the carbonyl group is still close enough to the aromatic proton to cause a downfield shift. Based on the structure determined, **II** should be named 3-dimethylamino-7-methyl-1-valeryl-1,4-dihydro-1,2,4-benzotriazine.

Many of the structural features are similar to azapropazone, although there are significant differences. The benzene ring is nearly planar (maximum deviation, C(10A), 0.013 Å), although again there is some evidence of a fold in the ring, but this time it is about C(8)C(10a) when the two halves are planar (maximum deviation C(7),C(6a), 0.006 Å) and the dihedral angle between the two planes is 4.5(9)°. Bond lengths and angles are normal.[43]

Figure 4.2 The structure of **II** with atom numbering. Displacement ellipsoids are drawn at 30% probability level.
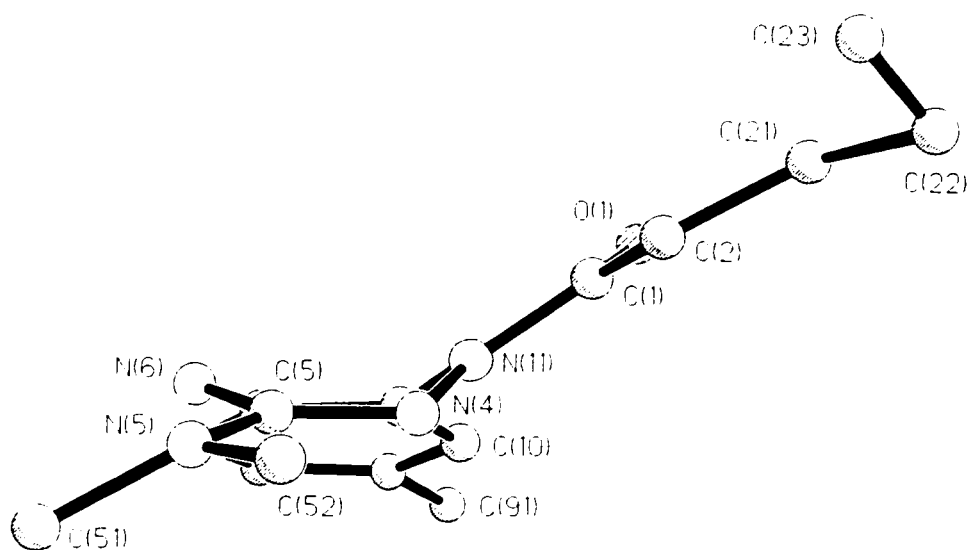
Figure 4.3 A side view of II. The atoms are drawn as rigid spheres, and the hydrogen atoms have been omitted for clarity.
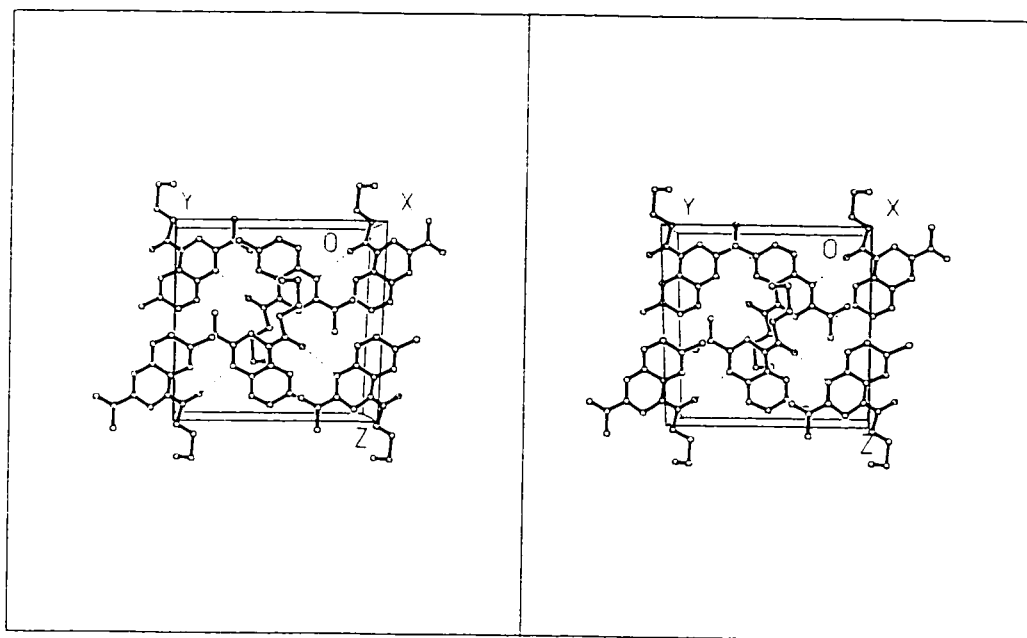
Figure 4.4 The stereoview plot of **II** packed within the unit cell. Hydrogen bonds are shown by broken lines.

The triazine ring shows some significant differences from the triazine in I. The C=N double bond is now between N(4) and C(5), which leaves the protonated N(6) position uncharged. The ring adopts a boat conformation, but in this case it is much more symmetric (plane C(6a)N(6)C(10a)N(11), 4.7(8)° to the benzene ring; maximum deviation, C(6a), 0.028 Å; C(5), 0.629 Å; N(4), 0.754 Å out of plane). With the removal of the restrictions of the pyrazolidine ring, N(11) is only 0.031Å out of the plane C(10a)C(21)N(4). The delocalization around the dimethylamino portion of the ring is less than in I, as shown by the bond lengths (N(4)-C(5), 1.304(7)Å; N(6)-C(5), 1.368(6)Å; N(5)-C(5), 1370(7)Å) and these changes are reflected in small changes in the other bond lengths of the ring. Again the dimethylamino group is not coplanar with N(4)C(5)N(6) and in this case the average angle is 29.3°, but the differences in the torsional angles are greater. The smaller conjugation to the dimethylamino group leads to greater nonplanarity at N(5), which lies 0.183Å out of the C(5)C(51)C(52) plane. The NMR spectrum showed that the two methyl groups were equivalent, but this time they did not become inequivalent at low temperature (-85°C). This could be for two reasons. The separation of the individual methyl signals is smaller or the barrier to rotation is smaller because the conjugation of the dimethylamino group to the double bond in the ring is smaller, as noted above.

The crystal packing of II (**Figure 4.4**) shows similarity to that of I. Spiral chains of molecules in the *b* direction are formed by each molecule forming an N(6)--H(6)...O(1) hydrogen bond to the next molecule (N(6)...O(1), 2.834(7)Å). However, the chains are related by a 2_1 axis, so that molecules do not lie adjacent to a

translationally equivalent one, as in I; therefore interactions between chains in both the *a* and *c* directions are of a van der Waals type.

The structure of III·CH₃CO₂H is shown in **Figure 4.5**. The C-H group at the C(5) position and the C=O group at the C(3) position in III has been interchanged compared to "III". The ¹H and ¹³C NMR spectral assignments, made with the aid of the 2D COSY pulse sequence and the inverse detected ¹H-¹³C heteronuclear HMBC and HSQC pulse sequences spectra, confirmed that this structure existed in solution. The molecule III is named 9-methyl-2-propyl-1H-Pyrazolo[1,2-a][1,2,4]benzotriazine-1,5-(2H)-dione.

A likely mechanism for the synthesis of III is given in **Scheme 1**. The C(3) site is acetylated by formic acid anhydride and the C(5) site is activated by formic acid or acetic acid. The activation of the C(3) and C(5) sites may occur concurrently. The acetylated O(3) position is substituted with a hydride ion from a formic acid molecule, while the C(5) is hydrolyzed during the work-up.

The crystal structure shows III hydrogen bonded to an acetic acid molecule of crystallization. The molecule was planar, in contrast to azapropazone itself, which had a   trigonal pyrimidal structure at the N(11) atom. Thus, our original postulate that the bend in azapropazone was caused by steric interaction of the dimethylamino group at the C(5) position seems to be correct.

In the original synthesis of molecule III, it was assumed that the hydrogen atom resided at the C(5) position, as shown for "III" in **Figure 4.1**, instead of the C(3) position, based on NMR studies. Indeed, an interpretation of ¹H and ¹³C NMR
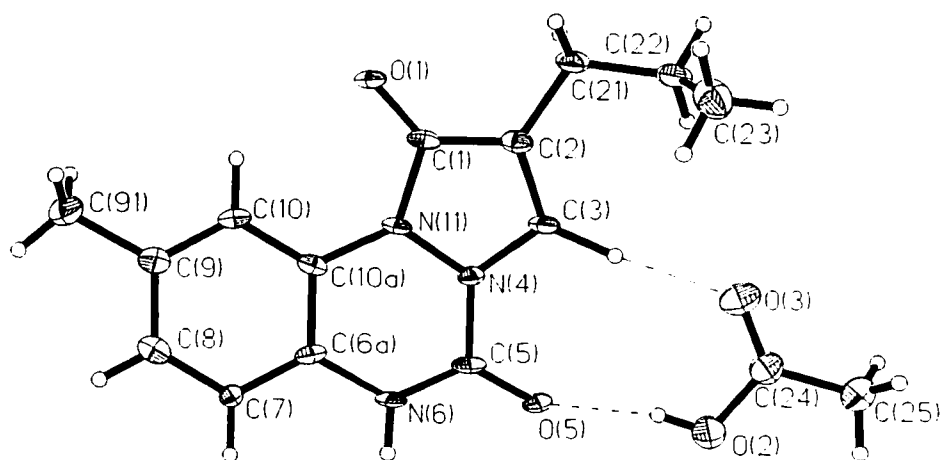
Figure 4.5 The structure of III·CH₃CO₂H, with atom numbering. Displacement ellipsoids are drawn at 30% probability level.
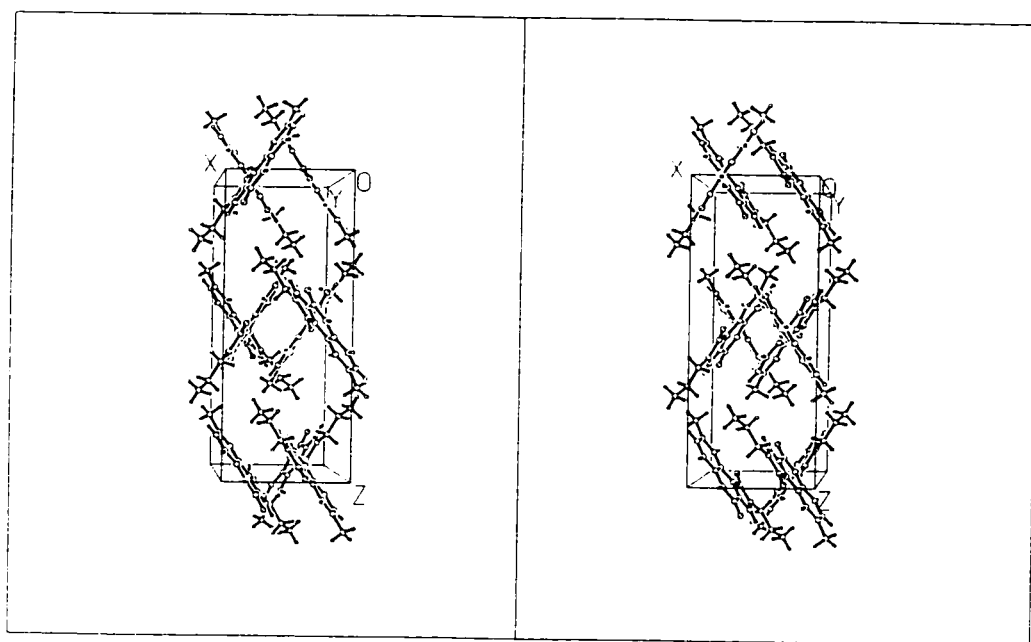
Figure 4.6 The packing of III·CH₃CO₂H within the unit cell.
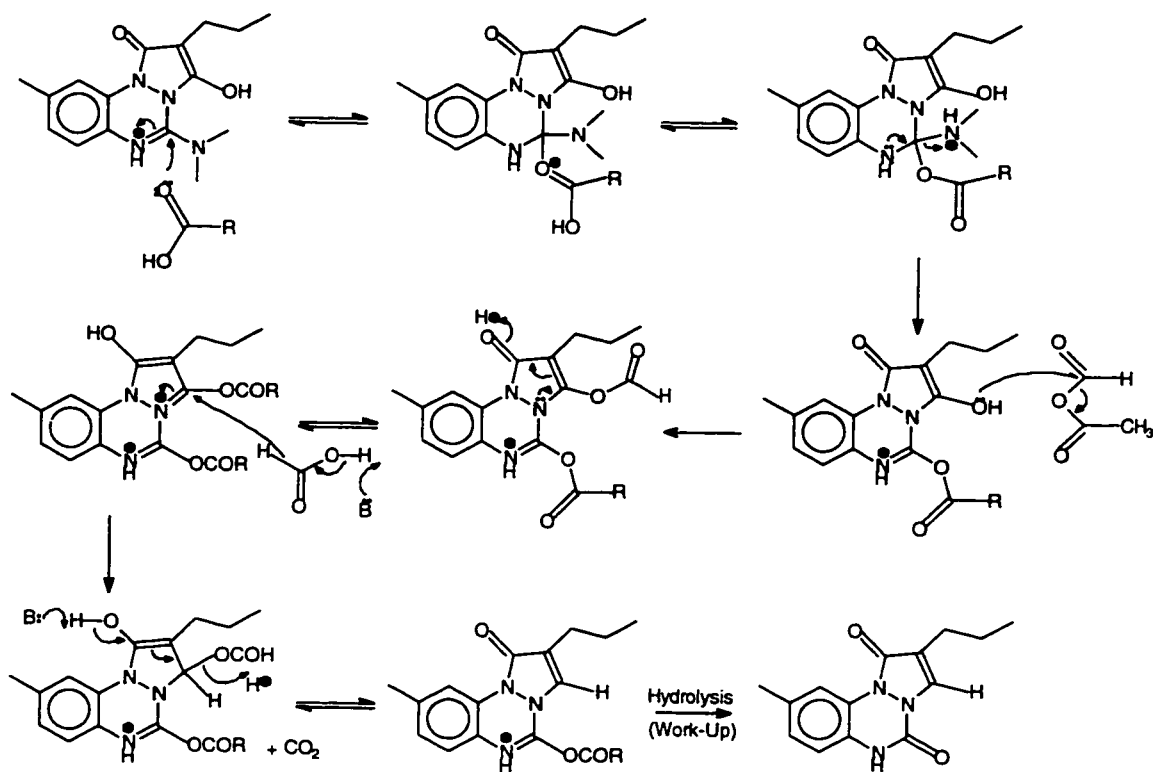
R = CH₃ or H   B: or B = Acetic Anhydride or Formic Acid Anhydride

Scheme 1

in the single dimension could easily lead to this conclusion. However, inspection of the inverse detected ^1H-^{13}C 2-D chemical shift correlation spectra with the HMBC pulse sequence showed a long range coupling between the proton at the C(3) position and the C(2) carbon atom.

The comparison of bond distances and angles of III with those of azapropazone (I) and the open-ring structure (II), showed certain differences consistent with delocalization from idealized structures. In III, the π electron density in the N(6)-C(5)-O(5) was more localized in the C=O bond [1.216(6) Å] compared to the more extensive delocalization in the N(6)-C(5)-N(5) systems of I and II. In the five-membered ring, the C(1)-C(2) bond [1.428(7)Å] was significantly longer in III than in I, which indicated that the delocalization of the electron density in this bond from C(1)-O(1) and C(2)-C(3) was small. Instead, there was evidence of delocalization of the elecron density from the C(2)-C(3) double bond [1.365(7)Å] of III into the C(3)-N(4) bond [1.356(6)Å] and even into the N(4)-N(11) bond [1.411(6)Å] and the C(10a)-N(11) bond [1.395(6)Å]. The delocalization around N(11) was quite different from that in azapropazone. The planarity of III allowed delocalization around N(11), whereas in I, where there was pyramidal distortion and N(11) was 0.395 Å out of the C(10a)C(1)N(4) plane, such delocalization could not take place.

The packing of III·CH$_3$CO$_2$H is shown in **Figure 4.6**. Molecules formed stacks along in the b direction. Within the stack, adjacent moleules were ~3.3 Å apart, so there was considerable π-π interaction between adjacent molecules.

There is a N(6)-H(6a)...O(1') hydrogen bonding chain in the c direction between molecules related by the c glide (N(6)...O(1'), 2.73(1) Å). The angles of molecules in alternate stacks along c were ~+32° and ~-32°. There were hydrogen bonds between the O(1) and N(6) atoms of different molecules, which was also seen in the packing of azapropazone. In addition to the chain hydrogen bonding, each molecule was bound to a solvate acetic acid molecule through O(2)-H(2a)...O(5) and C(3)-H(3a)...O(1) hydrogen bonds.

The molecule **IV**, the oxidation product of azapropazone, is shown in **Figure 4.7**. It is the same molecule identified as the photodecomposition product of azapropazone that is responsible for the photodermatitis that sometimes occurs in patients taking the drug.[44] The formal name for **IV** is 3-dimethylamino-7-methyl-1,2,4 benzotriazine.

The molecule is completely planar (maximum deviation C(51), 0.077Å). There is considerable delocalization through the N(5)-C(5)-N(6)-C(6a) system (N(5)-C(5), 1.353(4)Å; C(5)-N(6), 1.339(4)Å; N(6)-C(6a), 1.356(4)Å), and less so around the N(4)-N(11) double bond (N(4)-N(11), 1.296(4)Å; N(4)-C(10a), 1.377(4)Å; N(11)-C(5), 1.375(4)Å). The dihedral angle between the best planes between the benzene ring and the triazine ring is 1.2°, and the dihedral angle between the atoms of the amine group C(51)N(5)C(52) and N(4)C(5)N(6) is 2.8° (cf. 24.1(8)° for azapropazone).

The crystal packing of **IV**, shown in **Figure 4.8**, consists of spiral chains along b and c direction. In the a direction translationally equivalent molecules
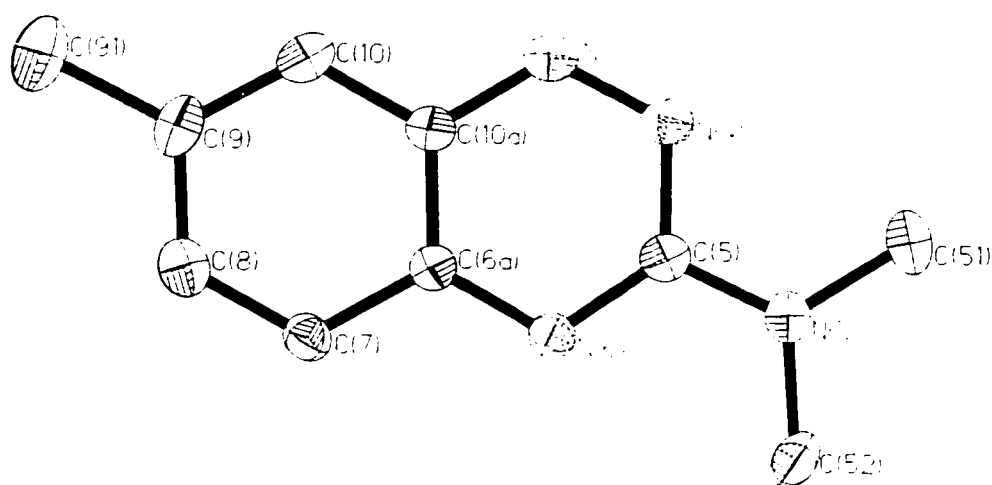
Figure 4.7 The structure of **IV** with atom numbering. Displacement ellipsoids are drawn at 50% probability level. The hydrogen atoms are not shown.
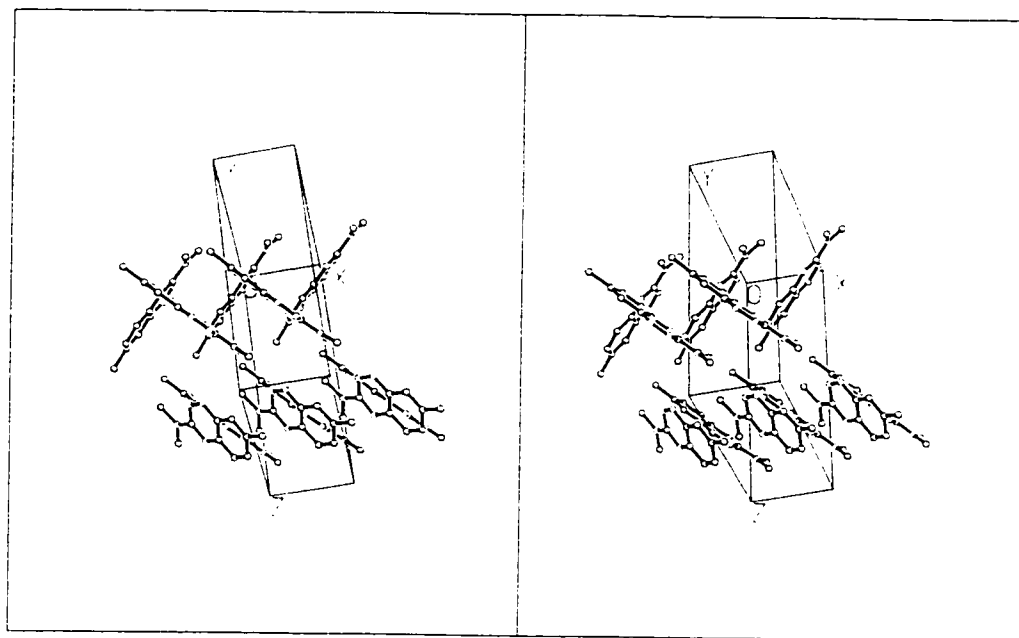
Figure 4.8 The packing diagram of **IV** within the unit cell.

are stacked 3.5 Å apart, so there is some π-π interacton. The interactions between the stacks are van der Waals.

The ¹H NMR showed that the proton attached to C(10) is shifted downfield by 0.5 ppm, even though it is not in the deshielding cone of the carbonyl group. This can be explained by the resonance and inductive effects in the molecule.

IVa   IVb
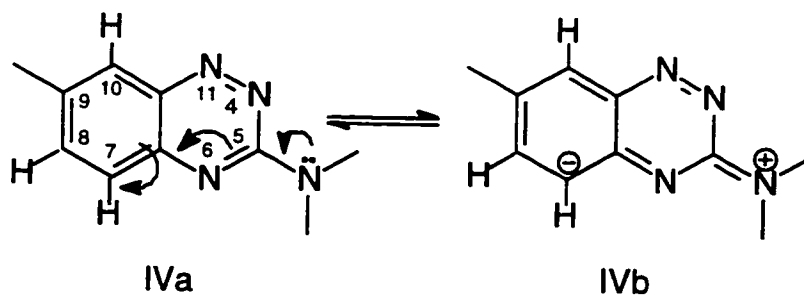
There is a σ-bond inductive effect from the N(4) and the N(6) atoms adjacent to the benzene ring. The electron withdrawing effect on the protons on C(7) and C(10) results in a downfield shift in the proton spectrum. However, the proton on C(7) can experience a resonance effect, shown with IVa and IVb, from the lone pair of electrons on the N(5) atom of the dimethylamino group. This effect causes the signal from the proton on C(7) to move upfield, thus cancelling the inductive effect. Thus, only the proton on C(10) remains downfield from the other aromatic proton.

The absence of the pyrazolidine ring in IV provided an opportunity to examine the energy barrier of the rotation of the dimethylamino group around the C(5)-N(5) bond in the absence of steric interference. The barrier was found to be 48 kJ/mol. In the case azapropazone, where steric hindrance did occur, the energy barrier for the oscillation of dimethylamino group was 40 kJ/mol. The higher barrier

for **IV** can be attested to the extensive delocalization in the molecule, as seen in **IVa** and **IVb**. It gives some double bond character to the C(5)-N(5) bond, which cannot undergo free rotation.

The structure of V·H$_2$O is shown in **Figure 4.9**. It is the same structure predicted by Mixich ("**V**"). The molecule is non-planar, although it is closer to planarity than was azapropazone. The non-planarity is best exemplified by the torsional angles for O(3)C(3)N(4)C(5), 29.8(8)°, and C(3)N(4)C(5)N(5), 14.6(7)°. The dihedral angle between the best planes of the pyrazolidine ring and the triazine ring is 15.0(3)°. The bend in the molecule seems to result from the interaction between H(5a) on the hydrazine group and and the O(3) atom. They are close enough to form a hydrogen bond (N(5)-H(5a)...O(3), 2.663(6)), but the O(3) atom is pushed down out of the C(5)N(5)H(5a) plane (0.517(7)Å) as in a steric interaction.

The delocalization of electron density throughout the molecule is less extensive than in azapropazone, although the molecule is still a zwitterion. There is more double bond character in C(2)-C(3) (1.368(8)Å) than in C(1)-C(2) (1.426(7)Å, 5.3σ). This may be caused by the H(5a)...O(3) interaction, which would draw electron density towards the C(3)-O(3) carbonyl group. However, there is not as great a difference between the C(1)-O(1) carbonyl group (1.243(6)Å) and the C(3)-O(3) carbonyl group (1.368(8)Å, 2σ). The delocalization of the electron density around the positive charge in the molecule is more similar to that of azapropazone.

The molecules in the unit cell are shown in **Figure 4.10** and are gene-rated by the I4̄ space group. There is extensive hydrogen bonding throughout
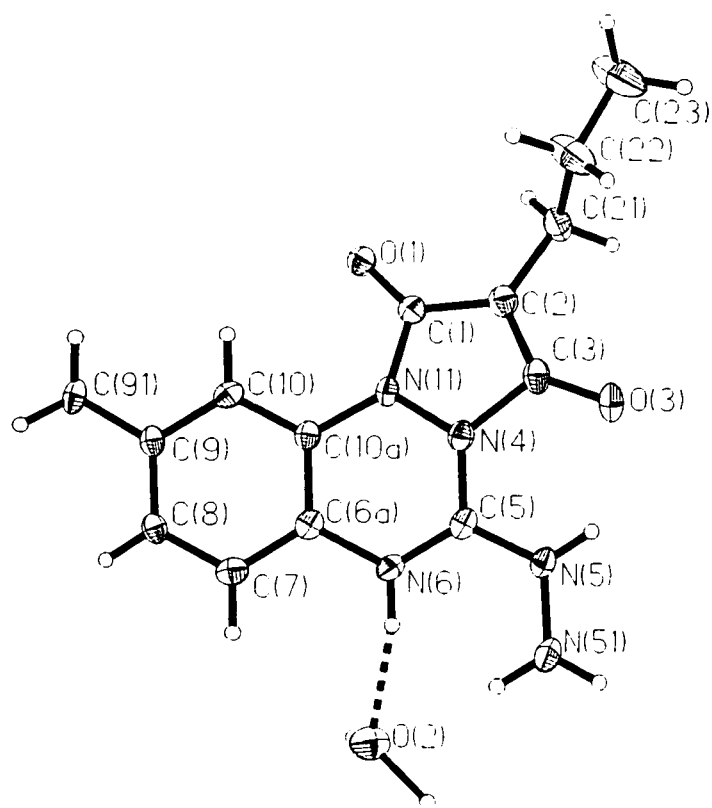
Figure 4.9 The structure of V·H₂O with atom numbering. The hydrogen bond is shown with broken lines. Displacement ellipsoids are drawn at 30% probability level.
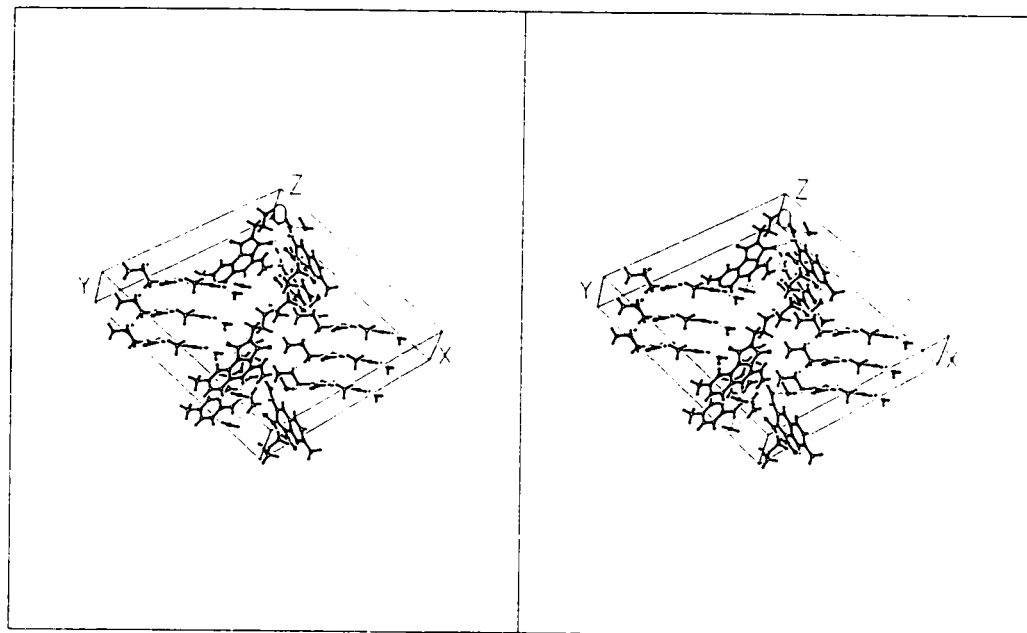
Figure 4.10 A stereoview of the packing of V·H_2O within the unit cell. Hydrogen bonds are represented by broken lines.

the packing of the molecule, from N(6)...O(2) (2.775(6)Å), to O(2)...O(1)' (2.707(6)Å), and O(3)'...N(51)" (2.872(6)Å).

The structure of VI·$(CH_3)_2SO$ is the product of the reaction of V with acetone, recrystallized from DMSO. The free amine of V nucleophilically attacked the carbonyl group of the acetone and replaced the oxygen atom to produce an imino group on the molecule. The structural characteristics of VI are similar to V. The molecule is planar, except for a slight bend in the pyrazolidine ring caused by the interaction between the O(3) atom and the H(5a) atom (N(5)...O(3), 2.638(5)Å). The non-planarity is best shown by the torsional angles of O(3)C(3)N(4)C(5), (3.5(7)°) and C(3)N(4)C(5)N(5), (9.2(7)°). The dihedral angle between the best planes of the pyrazolidine ring and the triazine ring is 3.4(6)Å. In VI, the O(3) atom is only 0.32(1)Å out of the C(5)N(5)H(5a) plane. These numbers indicate that there is considerably more bending in V than in VI, even though there is a shorter hydrogen bond between N(5) and O(3).

In addition to the differences in the non-planarity of V and VI, there was a difference in the delocalization of electron density. Whereas V had more double bond character between C(2) and C(3), the delocalization throughout the diketone system in VI is evenly distributed (O(1)-C(1), 1.244(5)Å; C(1)-C(2), 1.384(6)Å; C(2)-C(3), 1.389(5)Å; C(3)-O(3), 1.245(5)Å).

The view of the unit cell of the c axis clearly shows the eight molecules bond between N(5) and O(3) disproved the idea that it was the hydrogen bonding that encouraged the increased double bond character between C(2) and C(3) in V, as
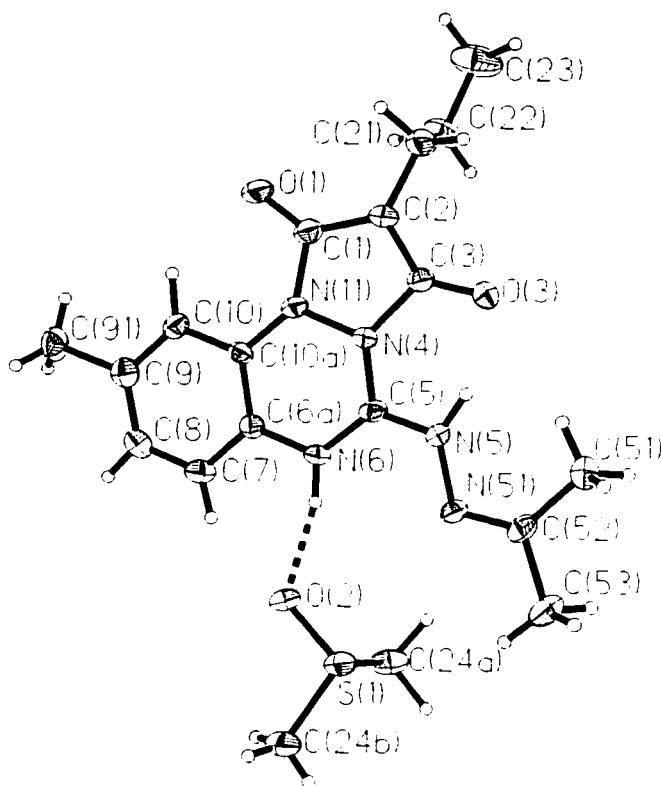
Figure 4.11 The structure of VI·(CH₃)₂SO with atom numbering. The hydrogen bond is shown with a broken line. Displacement ellipsoids are drawn at a 30% probability level.
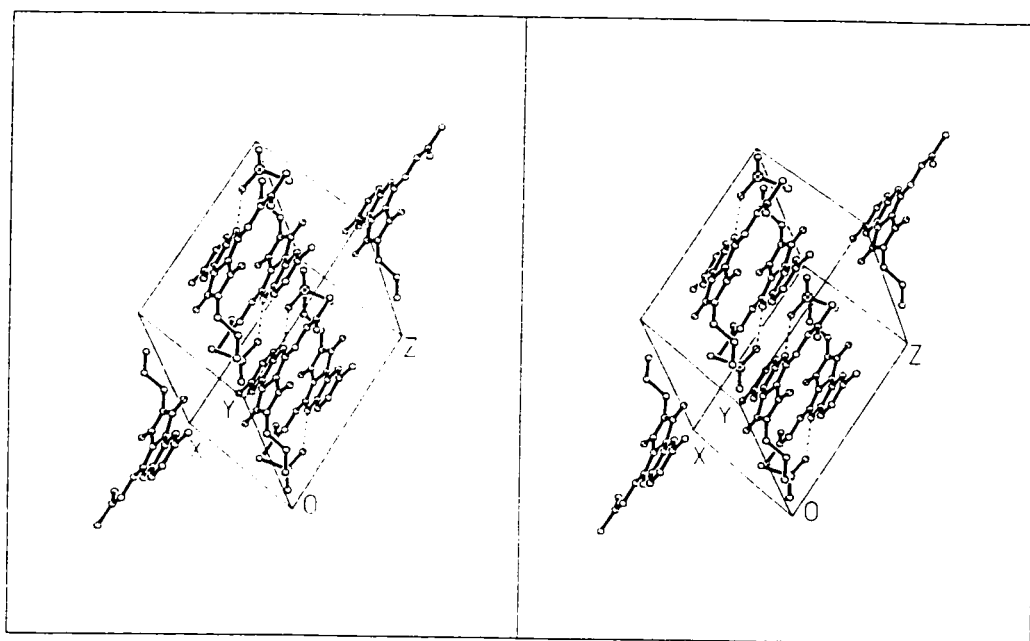
Figure 4.12 A stereoview diagram of the packing of VI·$(CH_3)_2SO$ in the unit cell. Hydrogen bonds are shown with broken lines.

proposed above.

The structure of **VI** shows N(6) hydrogen bonded to the oxygen of a dimethylsulphoxide molecule of crystallization (N(6)-H(6)...O(2), 2.700(5)Å). This is the extent of the hydrogen bond network in the packing of the molecule. The packing shows interleaved stacks of inversion-related pairs of molecules in the {1 1 0} direction. The distance between the molecules is 3.5 Å, which indicates some π-π interaction. Between stacks, the interaction is van der Waals.

4.3 Summary

This work has shown that the proposed structures for **II** and **III** were wrong. The ^{1}H NMR was not informative enough for the proper structure determination of these molecules. Instead, the "non-sporting" method of single crystal X-ray crystallography was needed solve the structures. The structures of **IV**, and **V** were as predicted. In addition, a new derivative, **VI**, was prepared and characterized.

The structural features of the molecules presented in this chapter show the differences in delocalization and conformation that occurred when the molecule of azapropazone was altered chemically. The range of characteristics, from the lack of delocalization and the non-planarity in **II**, to the extensive delocalization and planarity in **IV**, indicates that each molecule may act differently *in vivo*. A reason for this is that the delocalization of electron density affects the basicity and acidity of cationic and anionic sites of each molecule because it stabilizes the charge. The consequent pKa's of a molecule can affect its distribution in the body.

A future examination of the pKa's of the molecules is therefore warranted to

see how the delocalization with affects the pKa's. This information can be coupled with the modelling of these structures with the structures of the COX-1 and COX-2 sites in order aid in the design of effective and safe NSAIDs.

4.4 Experiments

The numbering scheme for the atoms of the structures in this chapter does not follow the IUPAC naming conventions, but is consistent with that of the parent azapropazone molecule.

Sample Preparation and Characterization

The Open-Ring Structure (II)

Azapropazone (1 g) was refluxed with formic acid (10 mL) for 1 h. Volatile solvent was removed by rotoevaporation at 70°C under vacuum (1mm Hg) to give a pale yellow oil. The oil was dissolved in 2-butanone and the solution was allowed to evaporate in air for several weeks, whereupon pale orange crystals were separated. Yield, 0.544 g, 60%; mp 159-163°C (lit. 161-162°C)[42]. ^{1}H NMR (200 MHz in CD_3OD at 25°C) δ: 0.95 (3H, t, $J_{23,22}=7.2$ Hz, $-COCH_2CH_2CH_2C\underline{H}_3$), 1.41 (2H, qt, $J_{22,23}=7.2$ Hz, $J_{22,21}=7.3$ Hz, $-COCH_2CH_2C\underline{H}_2CH_3$), 1.63 (2H, m, $J_{21,22}=$ 7.3 Hz, $J_{21,2}=3.9$ Hz, $-COCH_2C\underline{H}_2CH_2CH_3$), 2.26 (2H, s, CH_3 aromatic), 2.69 (2H, t, $J_{2,21}=3.9$ Hz, $-COC\underline{H}_2CH_2CH_2CH_3$), 2.95 (6H, s, $N(CH_3)_2$), 6.79 (1H, d, $J_{8,7}=8.1$ Hz, aromatic H(8)), 6.89 (1H, d, $J_{7,8}=8.1$ Hz, aromatic H(7)), 7.49 (1H, s, H(10)). ^{13}C NMR (50 MHz CD_3OD at 25°C) δ(ppm): 14.30 (C-23), 21.06 (aromatic-CH_3), 23.73 (C-22), 28.37 (C-21), 34.45 (C-2), 38.20 (-N($\underline{C}H_3)_2$), 115.32 (C-10), 123.61(C-7), 127.63 (C-8), 133.13 (C-9). EIMS, m/z (intensity, %) 273 (M^+).

Desdimethylaminoazapropazone (III)

Azapropazone (1g, 3.33mmol) was refluxed with formic acid (10 mL) and acetic anhydride (10 mL) under nitrogen at 50°C for 20 h. The reaction vessel was protected from light with aluminum foil. Volatile solvent was removed by roto-evaporation at 70°C (bath temperature) under vacuum (1 mm Hg) to give a bright yellow solid. The solid was dissolved in 1N NaOH (30 mL) and the resultant yellow solution was vacuum filtered through a Buchner funnel. The filtrate was acidified with concentrated HCl to form a yellow precipitate. The yellow product was recrystallized from glacial acetic acid to yield colourless needles. Yield: 557 mg, 65%; mp 261-263°C (lit. 262-264°C)[42]; TLC: R_f=0.65 (4:1 v/v $CHCl_3$:CH_3 OH); Analysis: C=61.0%, H=5.7%, N=14.3%. $C_{16}H_{19}N_3O_4$ required C=60.6%, H=6.0%, N=13.2%; IR (KBr pellet): v (cm^{-1}), 3200-3040 (broad, aromatic CH), 3063 (=C-H), 2959, 2933, 2875, 2741 (all aliphatic CH), 1735 (sharp, lactam C=O), 1641 (sharp, urea C=O), 1602 (medium, aromatic C=C); ^{1}H NMR (500.13 MHz in DMSO-d$_6$/C$_6$D$_6$ at 30°C): δ, 0.94 (3H, t, $J_{23,22}$=7.26 Hz, -CH$_2$CH$_2$CH$_3$), 1.62 (2H, m, $J_{22,23}$=7.26 Hz, $J_{22,21}$=7.46 Hz, -CH$_2$CH$_2$CH$_3$), 2.28 (3H, s, aromatic CH$_3$), 2.35 (2H, t, $J_{21,22}$=7.46 Hz, -CH$_2$CH$_2$CH$_3$), 6.97 (1H, d, $J_{8,7}$=8.05 Hz aromatic H(8)), 7.06 (1H, d, $J_{7,8}$=8.05 Hz, aromatic H(7)), 8.17 (1H, s, H(3)), 8.59 (1H, s, aromatic H(10)), 11.14 (1H, s, -N-H(6)); ^{13}C NMR (125 MHz in DMSO-d$_6$/C$_6$D$_6$ at 30°C): δ, 13.27 (C-23), 20.45 (C-9$_1$), 20.91 (C-22), 24.16 (C-21), 113.98 (C-2), 114.29 (C-10), 114.83 (C-7), 122.50 (C-6a), 122.84 (C-10a), 125.44 (C-8), 126.68 (C-3), 132.00 (9-C), 142.02 (C-5), 160.40 (C-1); EIMS: m/z (Intensity, %) 257 (100, M$^+$), 228 (30), 147 (20).

The Decomposition Product (IV)

Crude azapropazone (2g) was dissolved in 1N NaOH (20 mL). The reaction mixture was cooled in an ice bath whilst 30% H_2O_2 (2mL) was added dropwise. The dark orange solution was allowed to cool. The solution sat open to air for three days, whereupon bright orange parallelepiped crystals appeared. Mp 58-61°C (lit. 61-62°C)[42]. ^{1}H NMR (200 MHz in $CDCl_3$ at 25°C): δ, 2.48 (3H, s aromatic CH_3), 3.39 (6H, s, -N($CH_3)_2$), 7.24 (1H, d, collapsed, aromatic-H(7)), 7.50 (1H, d, collapsed, aromatic-H(8)), 7.96 (1H, s, aromatic-H(10)). ^{13}C NMR (125 MHz in DMSO-d_6 at 25°C): δ, 20.68 (aromatic CH_3), 36.74 (-N($CH_3)_2$), 125.80 (aromatic C(7)), 127.41 (aromatic C(8)), 134.66 (aromatic C(9)), 138.26 (aromatic C(10)), 140.23 (C-6a), 141.47 (C-10a), 158.83 (C-5). EIMS: m/z (%), 188 (20, M$^+$), 160 (70), 145(100, M-NC_2H_5).

Hydrazino-Azapropazone (V)

Azapropazone (2 g, recrystallized twice from methanol) was dissolved in absolute ethanol (30 mL) and warmed to 50°C under N_2. The reaction vessel was covered with foil. Hydrazine hydrate (330 μL) was added to the yellow solution. The solution was heated for 1 h, and then the solvent was removed by evaporation at reduced pressure (1 mm Hg) at 60°C under vacuum. The residue was recrystallized from methanol to give a fine white cotton-like product. Yield, 1.46 g, 76 %; mp 208-210°C (lit. 209-211°C), TLC: (80 $CHCl_3$: 20 CH_3OH), R$_f$ = 0.2 (streaking); ^{1}H NMR (500 MHz in DMSO-d_6 at 25°C) δ: 0.83 (3H, t, $J_{23,22}$= 7.5 Hz, -$CH_2CH_2CH_3$), 1.39 (2H, m, $J_{22,23}$= 7.5 Hz, $J_{22,21}$= 7.6 Hz, -$CH_2CH_2CH_3$), 1.95

(2H,t, $J_{21,22}$=7.6 Hz), 2.19 (3H,s, aromatic CH_3), 6.71 (1H, q, $J_{8,7}$= 8.2 Hz, $J_{8,10}$= 1.9 Hz, aromatic-H(8)), 7.16 (1H, d, $J_{7,8}$= 8.2 Hz, aromatic-H(7)), 8.06 (1H, d, $J_{10,8}$= 1.9 Hz), 10.81 (1H, s, N-H(6)). ^{13}C NMR (50 MHz in DMSO-d_6 at 25°C) δ: 13.86 (C-23), 20.90 (aromatic CH_3), 21.78 (C-22), 22.78 (C-21), 81.57 (C-2), 113.84 (C-10), 116.20 (C-7), 120.94 (C-10a), 122.91 (C-8), 127.12 (C-6a), 133.91 (C-9), 148.62 (C-5), 161.79 (=C-OH), 164.69 (C=O); EIMS: m/z, 287 (100, M$^+$), 258 (10), 175 (70), 147 (90).

Hydrazino-Imine-Azapropazone (VI)

Compound **V** (420 mg) was dissolved in a 50/50 mixture of methanol and acetone (40 mL), and put in the fridge for 12 h. Colourless needles fell out of solution during that time. Crystals suitable for the diffractometer were grown from DMSO. Yield: 295 mg, 61%; mp 195-197°C; ^{1}H NMR (500 MHz in DMSO-d_6 at 25°C) δ: 0.84 (3H, t, $J_{23,22}$=7.2 Hz, -$CH_2CH_2CH_3$), 1.41 (2H, m, $J_{22,23}$=7.2 Hz, $J_{22,21}$=7.5Hz, -$CH_2CH_2CH_3$), 1.93 (3H, s, CH_3-51 or 52), 1.97 (2H, t, $J_{21,22}$=7.5 Hz, -$CH_2CH_2CH_3$), 2.12 (3H, s, CH_3-51 or 52), 2.20 (3H, s, aromatic-CH_3), 6.72 (1H, m, $J_{8,7}$=3.6 Hz, $J_{8,10}$=2.0 Hz, aromatic H-8), 7.16 (1H, d, $J_{7,8}$=3.6 Hz, aromatic H-7), 8.08 (1H, d, $J_{10,8}$=2.0 Hz, aromatic H-10), ^{13}C NMR (125 MHz in DMSO-d_6 at 25°C) δ: 13.88 (C-23), 17.55 (C-51 or 53), 20.90 (aromatic-CH_3), 21.72 (C-22), 22.70 (C-21), 24.62 (-51 or 53), 82.41 (C-2), 113.82 (C-10), 116.61 (C-7), 120.60 (C-10a), 123.00 (C-8), 127.02 (C-6a), 134. 31(C-9), 144.45 (C-5), 159.50 (C-52), 161.56 (=C-OH), 164.16(-C=O). EIMS m/z (intensity, %): 327 (M+, 100), 287 (30).

Crystal Stuctures

Crystal Structure of II

A crystal was selected after examination for clarity and sharp extinction with a polarizing microscope, and mounted on a glass fibre with epoxy glue. Unit cell determination and intensity data collection were performed on a Rigaku AFC6-R diffractometer with monochromatized Cu-Kα (λ=1.54178Å) radiation. The unit cell was obtained by least-squares refinements of the angular coordinates of 24 reflections with θ from 21.2° to 39.7°. An absorption correction was made with DIFABS.[29] The structure was solved by direct methods and refined on F by full-matrix least squares. Hydrogen atoms adjacent to atoms in the benzotriazine ring were found from the difference map, but were not refined. Hydrogen atoms in the exocyclic alkyl groups were placed in calculated positions and rode on the atoms to which they were attached. Temperature factors of non-hydrogen atoms were refined anisotropically, and those of hydrogen atoms were not refined. The details of data acquisition and treatment are given in **Table 4.1**. The atomic coordinates and isotropic temperature factors can be found in **Table 4.2** and interatomic distances and angles are given **Table 4.3**. The molecule is shown in **Figures 4.2** and **4.3**, and the packing diagram is shown in **Figure 4.4**. The refinement of atoms C(22) and C(23) presented difficulty because of disorder. Many refinements were tried, with partial occupancies of multiple sites or restraints on bond lengths, but none were satisfactory or better than the results presented here.

Crystal Structure of III·CH₃CO₂H

Crystals were selected after examination for sharp extinctions with a polarizing microscope and were secured in 0.2 mm sealed capillaries with epoxy glue. Unit cell determination and intensity data collection were performed on a Siemens P4 diffractometer with monochromatized Mo-Kα (λ=0.71073 Å) radiation from a rotating anode. The unit cell was obtained by least-squares refinements of the angular coordinates of 32 reflections with θ from 9.80° to 24.74°. An absorption correction was not applied. The structure was solved by direct methods and refined on F^2 by full-matrix least squares. The hydrogen atom adjacent to atom C(3) was found from the difference map. All the other hydrogen atoms were placed in calculated positions and rode on the atoms to which they were attached. The details of data acquisition and treatment are given in **Table 4.4**. The atomic coordinates and isotropic temperature factors can be found in **Table 4.5** and interatomic distances and angles are given in **Table 4.6**. The molecule is shown in **Figure 4.6** and the packing diagram is shown in **Figure 4.7**.

Crystal Structure of IV

A crystal was selected after examination for clarity and sharp extinction with a polarizing microscope. The crystal was soluble in all solvents and adhesives used to try to mount the crystal. Instead, a glass capillary was drawn out over a Bunsen burner and broken off at the top so that the crystal could sit in the top. The bottom of the capillary was glued to a brass pin. Unit cell determination and intensity data collection were performed on a Siemens SMART Platform CCD 3-circle

diffractometer with monochromatized Mo-Kα (λ=0.71073Å) radiation.[45] An initial set of cell constants was calculated from reflections harvested from three sets of 30 frames. This produced orientation matrices determined from 46 reflections. Final cell constants were calculated from a set of 2079 strong reflections from the actual data collection. A semi-empirical ψ-scan absorption correction was applied. The structure was solved by direct methods and refined on F^2 by full-matrix least squares. The details of data acquisition and treatment are given in **Table 4.7**. The atomic coordinates and isotropic temperature factors can be found in **Table 4.8** and interatomic distances and angles are given in **Table 4.9**. The molecule is shown in **Figure 4.7** and the packing diagrams can be found in **Figure 4.8**.

Crystal Structure of V·H₂O

A crystal was selected after examination for clarity and sharp extinction with a polarizing microscope, and mounted on a glass fibre with epoxy glue. Unit cell determination and intensity data collection were performed on a Siemens SMART Plarform CCD 3-circle diffractometer with monochromatized Mo-Kα radiation (λ=0.71073Å).[45] An initial set of cell constants was calculated from reflections harvested from three sets of 30 frames. These initial set of frames were oriented such that orthogonal wedges of reciprical space were surveyed. This produced orientation matrices determined from 41 reflections. Final cell constants were calculated from a set of 3065 strong reflections from the actual data set. The data collection technique used was hemisphere collection, where a randomly oriented region of reciprocal space is surveyed to the extent of 1.3

hemispheres to a resolution of 0.84 Å. Three major swaths of frames of 45 seconds duration were collected with 0.30° steps in ω. This collection strategy provided a high degree of redundancy. The crystal did not diffract well, but it did provide enough intensity with the long scans to solve and refine. All non-hydrogen atoms were refined with anisotropic displacement parameters. All hydrogen atoms were placed in ideal positions and refined as riding atoms with relative isotropic displacement parameters (1.2 U_{eq} for methylene and aryl hydrogen atoms, 1.5 U_{eq} for methyl hydrogen atoms). Further details of data acquisition and treatment can be found in **Table 4.10**. The atomic coordinates and isotropic temperature factors can be found in **Table 4.11** and interatomic distances and angles are given in **Table 4.12**. The molecule is shown in **Figure 4.9**, and the packing diagram is shown in **Figure 4.10**.

Crystal structure of VI·$(CH_3)_2SO$

A crystal was selected after examination and clarity and sharp extinction with a polarizing microscope, and mounted on a glass fibre with epoxy glue. Unit cell determination and intensity data collection were performed on a Siemens P4 diffractometer with monochromatized Mo-Kα (λ = 0.71073 Å) radiation. The unit cell was obtained by least-squares refinements of the angular coordinates of 35 reflections with θ from 11.32 to 19.34°. A semi-empirical ψ-scan absorption correction was applied. The structure was solved by direct methods and refined on F^2 by full-matrix least squares. Hydrogen atoms were put in calculated positions, and were not refined: they rode on the atoms to which they were attached.

Temperature factors of non-hydrogen atoms were refined anisotropically, and those of hydrogen atoms were not refined. The details of data acquisition and treatment are given in **Table 4.13**. The atomic coordinates and isotropic temperature factors can be found in **Table 4.14** and the interatomic distances and angles are given in **Table 4.15**. The molecule is shown in **Figure 4.11**, and the packing diagrams are shown in **Figure 4.12**.

Variable Temperature ^{1}H NMR Experiment with IV

The variable temperature NMR data were obtained with a Bruker AC-300 spectrometer. The solvent was acetone-d_6 which provided the deuterium lock signal. The spectra were recorded every 10° from -53 to 40°C. The spectra were simulated and fitted with the program MEX by A.D.Bain.[46]

Table 4.1 Crystallographic data for **II**.

Formula	$C_{15}H_{22}N_4O$
Formula weight	274.4
Crystal colour, shape, size (mm)	Orange hexagonal plate, 0.3 x 0.3 x 0.2
Space group	$P2_1/n$
λ (Å)	1.54178
Unit cell parameters (Å)	a = 10.240(2)
	b = 12.608(3)
	c = 13.176 (4)
	β = 108.46(3)°
Volume (Å^3)	1613.6(8)
Z	4
D_{calc} (g/cm^3)	1.129
Index ranges	$-4 \le h \le 10, -13 \le k \le 14, -14 \le l \le 14$
Max. 2θ (°)	120
Temperature (°C)	25
Absorption coeffient (mm^{-1})	0.585
F(000)	592
Transmission factor (range)	0.59,1.00
Reflections collected	2358
Independent reflections	2209 (R_{int} = 0.0537)
Reflections used	2209
No. Of parameters refined	171
Final R indices	
R_1	0.1671
wR	0.0703
Goodness-of-fit, S	1.63
Largest Δ/σ	0.001
Mean Δ/σ	0.000
Data:parameter ratio	12.9:1
Largest difference peak (e Å^{-3})	0.58
Largest difference hole (e Å^{-3})	-0.45

Table 4.2 Atomic coordinates (x10^4) and equivalent isotropic displacement coefficients (Å^{2}x10^3) for II.

	x	y	z	U$_{eq}$
O(1)	2247(4)	6247(3)	3753(3)	65(2)
N(4)	4034(5)	3822(3)	4393(3)	50(2)
N(11)	3397(4)	4722(3)	3769(3)	47(2)
N(5)	4247(5)	2013(4)	4310(4)	63(2)
N(6)	3334(4)	2962(3)	2716(4)	55(2)
C(2)	2714(6)	5155(4)	5313(4)	64(3)
C(5)	3866(5)	2965(5)	3806(4)	48(2)
C(1)	2751(6)	5432(4)	4227(4)	53(3)
C(52)	4637(7)	1995(4)	5468(5)	85(4)
C(51)	4805(7)	1180(5)	3824(5)	88(3)
C(10A)	3575(5)	4833(4)	2738(4)	45(2)
C(7)	3517(5)	3910(5)	1148(4)	56(3)
C(91)	4221(7)	6823(5)	794(5)	84(4)
C(10)	3852(5)	5777(4)	2310(4)	52(3)
C(6A)	3461(5)	3895(4)	2183(4)	47(2)
C(8)	3712(6)	4856(5)	702(5)	63(3)
C(9)	3923(6)	5793(5)	1281(5)	55(3)
C(22)	2345(12)	5912(8)	7127(8)	201(5)
C(21)	2164(10)	6004(7)	5836(6)	158(6)
C(23)	1642(12)	5158(9)	7093(10)	310(9)

* Equivalent isotropic U$_{eq}$ defined as one third of the trace of the orthogonalized U$_{ij}$ tensor.

Table 4.3   Bond lengths (Å) and angles(°) for II.

C(1)-C(2)	1.486(8)	N(4)-C(5)	1.308(7)
C(5)-N(6)	1.365(7)	N(6)-C(6A)	1.397(7)
C(6A)-C(7)	1.382(9)	C(7)-C(8)	1.372(9)
C(8)-C(9)	1.386(9)	C(9)-C(10)	1.381(9)
C(10)-C(10A)	1.384(8)	C(10A)-N(11)	1.434(8)
N(11)-C(1)	1.361(8)	N(4)-N(11)	1.432(6)
C(6A)-C(10A)	1.377(8)	C(1)-O(1)	1.228(7)
C(2)-C(21)	1.478(11)	C(21)-C(22)	1.656(14)
C(22)-C(23)	1.185(16)	C(5)-N(5)	1.367(7)
N(5)-C(51)	1.439(9)	N(5)-C(52)	1.449(8)
C(9)-C(91)	1.521(9)		

N(11)-C(1)-C(2)	115.8(5)	N(11)-N(4)-C(5)	111.4(4)
N(4)-C(5)-N(6)	123.9(5)	C(5)-N(6)-C(6A)	117.3(4)
N(6)-C(6A)-C(7)	123.2(5)	N(6)-C(6A)-C(10A)	117.5(5)
C(10A)-C(6A)-C(7)	119.3(5)	C(6A)-C(7)-C(8)	119.5(5)
C(7)-C(8)-C(9)	121.5(6)	C(8)-C(9)-C(10)	118.7(6)
C(9)-C(10)-C(10A)	119.6(5)	C(10)-C(10A)-N(11)	125.1(5)
C(10)-C(10A)-C(6A)	121.0(6)	C(6A)-C(10A)-N(11)	113.9(5)
C(10A)-N(11)-C(1)	125.4(4)	C(10A)-N(11)-N(4)	115.7(4)
N(4)-N(11)-C(1)	117.0(4)	N(11)-C(1)-O(1)	120.7(5)
O(1)-C(1)-C(2)	123.5(6)	C(1)-C(2)-C(21)	114.1(5)
C(2)-C(21)-C(22)	119.5(7)	C(21)-C(22)-C(23)	98.6(9)
N(4)-C(5)-N(5)	118.3(5)	N(5)-C(5)-N(6)	117.8(5)
C(5)-N(5)-C(51)	121.1(5)	C(5)-N(5)-C(52)	117.7(5)
C(51)-N(5)-C(52)	116.2(5)	C(8)-C(9)-C(91)	120.9(6)
C(91)-C(9)-C(10)	120.4(5)		

Table 4.4 Crystallographic data for III·CH_3CO_2H.

Formula	$C_{14}H_{15}N_3O_2 \cdot CH_3CO_2H$
Formula weight	317.3
Crystal colour, shape, size (mm)	Colourless needle, 0.4 x 0.1 x 0.1
Space group	C2/c
λ (Å)	0.71073
Unit cell parameters (Å)	a = 26.173(6)
	b = 7.758(1)
	c = 15.420(4)
	β = 90.22(2)°
Volume (Å³)	3131.3(1)
Z	8
D_{calc} (g/cm³)	1.346
D_{meas} (g/cm³)	1.32(3)
Index ranges	$-1 \le h \le 28, -1 \le k \le 8, -16 \le l \le 16$
Temperature (°C)	-50
Absorption coeffient (mm⁻¹)	0.098
F(000)	1344
Reflections collected	2612
Independent reflections	2052 (R_{int} = 0.0718)
Reflections used	2052
No. Of parameters refined	208
Final R indices [I > 2σ(I)]	R_1=0.0534, wR_2=0.1175
Final R indices (all data)	R_1=0.0942, wR_2=0.1445
Goodness-of-fit, S	0.742
Data:parameter ratio	9.8:1
Largest difference peak (e Å⁻³)	0.243
Largest difference hole (e Å⁻³)	-0.230

Table 4.5   Atomic coordinates (x10⁴) and equivalent isotropic displacement parameters (Å^2x 10³) for III·CH_3CO_2H.

	x	y	z	U_{eq}
N(4)	2977(2)	989(6)	4852(3)	29(1)
N(6)	2591(2)	29(7)	3587(3)	34(1)
N(11)	2590(2)	226(6)	5358(2)	26(1)
O(5)	3336(2)	1547(5)	3550(2)	38(1)
C(10A)	2182(2)	-617(8)	4957(3)	26(2)
C(6A)	2190(2)	-722(8)	4047(3)	26(2)
O(1)	2448(1)	-28(6)	6833(2)	37(1)
C(10)	1778(2)	-1329(8)	5421(3)	33(2)
C(7)	1797(2)	-1544(8)	3622(3)	27(2)
C(3)	3333(2)	1703(8)	5383(3)	33(2)
C(1)	2725(2)	489(8)	6233(3)	28(2)
C(5)	2988(2)	876(8)	3945(3)	33(2)
O(2)	4240(2)	3023(7)	3269(3)	79(2)
C(9)	1383(2)	-2174(8)	4993(3)	35(2)
C(8)	1397(2)	-2256(8)	4083(4)	38(2)
C(21)	3459(2)	2019(8)	7038(3)	39(2)
C(91)	941(2)	-295(8)	5492(4)	48(2)
C(2)	3191(2)	1450(7)	6224(3)	29(2)
C(24)	4547(2)	3371(10)	3958(4)	55(2)
C(22)	4004(2)	2702(9)	6910(3)	48(2)
O(3)	4399(2)	3113(8)	4668(3)	92(2)
C(23)	4390(2)	1283(8)	6719(4)	59(2)
C(25)	5030(2)	4179(9)	3707(4)	70(3)

* U_{eq} is defined as one third of the trace of the orthogonalized U_{ij} tensor.

Table 4.6   Bond lengths [Å] and angles [°] for III·CH₃CO₂H.

C(1)-O(1)	1.244(6)	N(6)-C(6A)	1.395(7)
C(1)-N(11)	1.409(6)	C(6A)-C(10A)	1.407(6)
C(1)-C(2)	1.428(7)	C(6A)-C(7)	1.375(7)
C(2)-C(3)	1.365(7)	C(7)-C(8)	1.383(7)
C(2)-C(21)	1.502(6)	C(8)-C(9)	1.405(7)
C(3)-N(4)	1.356(6)	C(9)-C(10)	1.389(7)
N(4)-N(11)	1.411(6)	C(9)-C(91)	1.519(7)
N(4)-C(5)	1.402(6)	C(10)-C(10A)	1.392(7)
C(5)-O(5)	1.216(6)	C(10A)-N(11)	1.395(6)
C(5)-N(6)	1.346(7)	C(21)-C(22)	1.536(7)
C(22)-C(23)	1.522(8)	C(24)-O(2)	1.357(7)
C(24)-O(3)	1.179(6)	C(24)-C(25)	1.465(8)
O(1)-C(1)-N(11)	121.3(5)	C(10A)-C(6A)-C(7)	119.1(5)
O(1)-C(1)-C(2)	132.5(5)	C(10A)-C(6A)-N(6)	119.9(5)
N(11)-C(1)-C(2)	106.1(5)	C(7)-C(6A)-N(6)	121.0(4)
C(3)-C(2)-C(1)	108.7(5)	C(8)-C(7)-C(6A)	120.5(5)
C(3)-C(2)-C(21)	128.5(5)	C(7)-C(8)-C(9)	121.2(6)
C(1)-C(2)-C(21)	122.8(5)	C(10)-C(9)-C(8)	118.3(6)
C(2)-C(3)-N(4)	109.0(5)	C(10)-C(9)-C(91)	121.1(5)
C(3)-N(4)-N(11)	109.3(4)	C(8)-C(9)-C(91)	120.7(6)
C(3)-N(4)-C(5)	127.7(5)	C(10A)-C(10)-C(9)	120.6(5)
N(11)-N(4)-C(5)	122.9(5)	C(10)-C(10A)-C(6A)	120.3(5)
O(5)-C(5)-N(6)	125.7(5)	C(10)-C(10A)-N(11)	122.7(4)
O(5)-C(5)-N(4)	119.4(6)	C(6A)-C(10A)-N(11)	117.0(5)
N(6)-C(5)-N(4)	114.9(5)	C(10A)-N(11)-C(1)	133.0(5)
C(5)-N(6)-C(6A)	125.2(5)	C(10A)-N(11)-N(4)	120.1(4)
C(1)-N(11)-N(4)	106.9(4)	C(2)-C(21)-C(22)	115.2(5)
C(23)-C(22)-C(21)	113.1(5)	O(3)-C(24)-O(2)	119.8(6)
O(3)-C(24)-C(25)	127.1(6)	O(2)-C(24)-C(25	112.9(5)

Table 4.7 Crystallographic data for **IV**

Formula	$C_{10}H_{12}N_4$
Formula weight	188.24
Crystal colour, shape, size (mm)	orange plate, 0.50 x 0.28 x 0.12
Space group	$P2_12_12_1$
λ (Å)	0.71073
Unit cell parameters (Å)	a = 4.9123(4)
	b = 12.392(1)
	c = 16.218(1)
Volume (Å^3)	987.3(1)
Z	4
D_{calc} (g/cm^3)	1.266
Index ranges	$-4 \le h \le 5$, $-14 \le k \le 13$, $-16 \le l \le 19$
Max 2θ (°)	50.4
Temperature (°C)	-100
Absorption coeffient (mm^{-1})	0.081
$F(000)$	400
Transmission factor (range)	0.679, 0.801
Reflections collected	4862
Independent reflections	1720 (R_{int} = 0.0547)
Reflections used	1720
No. Of parameters refined	142
Final R indices [I > 2σ(I)]	R1=0.0585, wR2=0.1154
Final R indices (all data)	R1=0.0862, wR2=0.1281
Goodness-of-fit on F^2, S	1.168
Data:parameter ratio	12.11:1
Largest difference peak (e Å^{-3})	0.148
Largest difference hole (e Å^{-3})	-0.136

Table 4.8   Atomic coordinates $(\times 10^4)$ and equivalent isotropic displacement parameters $(\text{Å}^2 \times 10^3)$ for **IV**.

	x	y	z	U_{eq}
N(6)	1294(5)	6712(2)	3747(2)	37(1)
N(4)	2336(6)	5308(2)	2760(2)	43(1)
N(11)	597(6)	4649(2)	3088(2)	44(1)
N(5)	4515(6)	6962(2)	2729(2)	48(1)
C(5)	2646(6)	6319(2)	3096(2)	37(1)
C(6A)	-513(6)	6014(2)	4087(2)	33(1)
C(7)	-2041(7)	6313(3)	4788(2)	42(1)
C(8)	-3812(7)	5594(3)	5128(2)	48(1)
C(9)	-4210(7)	4544(3)	4809(2)	45(1)
C(10)	-2723(7)	4250(2)	4123(2)	45(1)
C(10A)	-880(6)	4979(2)	3763(2)	34(1)
C(91)	-6189(8)	3781(3)	5218(2)	65(1)
C(52)	4968(8)	8045(3)	3040(2)	55(1)
C(51)	6180(7)	6588(3)	2043(2)	53(1)

$^{+}U_{eq}$ is defined as one third of the trace of the orthogonalized U_{ij} tensor.

Table 4.9   Bond lengths [Å] and angles [°] for **IV**.

N(6)-C(5)	1.339(4)	N(6)-C(6A)	1.356(4)
N(4)-N(11)	1.296(3)	N(4)-C(5)	1.375(4)
N(11)-C(10A)	1.377(4)	N(5)-C(5)	1.353(4)
N(5)-C(52)	1.452(4)	N(5)-C(51)	1.456(4)
C(6A)-C(10A)	1.397(4)	C(6A)-C(7)	1.412(4)
C(7)-C(8)	1.362(4)	C(8)-C(9)	1.413(5)
C(9)-C(10)	1.381(4)	C(9)-C(91)	1.510(4)
C(10)-C(10A)	1.406(4)		

C(5)-N(6)-C(6A)	114.4(2)	N(11)-N(4)-C(5)	119.0(3)
N(4)-N(11)-C(10A)	119.1(3)	C(5)-N(5)-C(52)	119.7(3)
C(5)-N(5)-C(51)	122.0(3)	C(52)-N(5)-C(51)	118.3(3)
N(6)-C(5)-N(5)	118.0(3)	N(6)-C(5)-N(4)	126.1(3)
N(5)-C(5)-N(4)	115.9(3)	N(6)-C(6A)-C(10A)	121.2(3)
N(6)-C(6A)-C(7)	120.5(2)	C(10A)-C(6A)-C(7)	118.3(3)
C(8)-C(7)-C(6A)	119.6(3)	C(7)-C(8)-C(9)	122.9(3)
C(10)-C(9)-C(8)	117.7(3)	C(10)-C(9)-C(91)	122.0(3)
C(8)-C(9)-C(91)	120.3(3)	C(9)-C(10)-C(10A)	120.3(3)
N(11)-C(10A)-C(6A)	120.2(3)	N(11)-C(10A)-C(10)	118.6(3)
C(6A)-C(10A)-C(10)	121.2(3)		

Table 4.10 Crystallographic data for V·H_2O.

Formula	$C_{14}H_{17}N_5O_2$·H_2O
Formula weight	305.34
Crystal colour, shape, size (mm)	colourless needle,0.45x0.04x0.04
Space group	$I\bar{4}$
λ (Å)	0.71073
Unit cell parameters (Å)	a = 25.538(1)
	b = 25.538(1)
	c = 4.6560(3)
Volume (Å^3)	3036.7(3)
Z	8
D_{calc} (g/cm^3)	1.336
Index ranges	-30≤ h≤29, -14≤ k≤ 30, -5≤ l≤5
Max 2θ (°)	50.8
Temperature (°C)	-100
Absorption coeffient (mm^{-1})	0.097
F(000)	1296
Transmission factor (range)	0.699, 0.960
Reflections collected	7682
Independent reflections	2635 (R_{int} = 0.1010)
Reflections used	2635
No. Of parameters refined	207
Final R indices [I > 2σ(I)]	R_1=0.0857, wR_2=0.1541
Final R indices (all data)	R_1=0.1171, wR_2=0.2095
Goodness-of-fit on F^2, S	1.269
Data:parameter ratio	12.73:1
Largest difference peak (e Å^{-3})	0.285
Largest difference hole (e Å^{-3})	-0.238

Table 4.11 Atomic coordinates (x 10^4) and equivalent isotropic displacement parameters (Å^2 x 10^3) for $V \cdot H_2O$.

	x	y	z	U_{eq}
N(6)	6304(2)	2109(2)	2387(9)	32(1)
N(4)	7096(2)	1704(2)	3316(9)	31(1)
N(11)	6935(2)	1251(2)	1794(10)	31(1)
C(5)	6740(2)	2081(2)	3898(11)	29(1)
C(6A)	6173(2)	1720(2)	329(12)	31(1)
C(7)	5720(2)	1765(2)	-1309(11)	33(1)
C(8)	5596(2)	1372(2)	-3228(12)	32(1)
C(9)	5910(2)	936(2)	-3580(11)	30(1)
C(10)	6367(2)	900(2)	-2001(11)	30(1)
C(10A)	6496(2)	1286(2)	-10(11)	29(1)
C(91)	5761(2)	499(2)	-5615(12)	38(1)
C(3)	7538(2)	1555(2)	5064(12)	35(1)
C(2)	7638(2)	1038(2)	4502(11)	38(1)
C(1)	7266(2)	839(2)	2501(11)	33(1)
O(3)	7749(2)	1898(2)	6620(9)	45(1)
O(1)	7203(1)	393(1)	1492(9)	39(1)
N(5)	6855(2)	2420(2)	5946(9)	33(1)
N(51)	6546(2)	2871(2)	6256(10)	40(1)
C(21)	8059(2)	717(2)	5905(13)	45(2)
C(22)	8584(3)	733(3)	4470(18)	81(3)
C(23)	8978(3)	377(4)	5810(21)	103(3)
O(2)	5476(1)	2804(2)	3025(10)	54(1)

*U_{eq} is defined as one third of the trace of the orthogonalized U_{ij} tensor.

Table 4.12 Bond lengths [Å] and angles [°] for V·H$_2$O.

N(6)-C(5)	1.320(6)	N(6)-C(6A)	1.420(6)
N(4)-C(5)	1.352(6)	N(4)-N(11)	1.418(6)
N(4)-C(3)	1.444(7)	N(11)-C(1)	1.387(6)
N(11)-C(10A)	1.404(6)	C(5)-N(5)	1.321(6)
C(6A)-C(7)	1.389(7)	C(6A)-C(10A)	1.391(7)
C(7)-C(8)	1.380(7)	C(8)-C(9)	1.382(7)
C(9)-C(10)	1.382(7)	C(9)-C(91)	1.512(7)
C(10)-C(10A)	1.393(7)	C(3)-O(3)	1.259(6)
C(3)-C(2)	1.368(8)	C(2)-C(1)	1.426(7)
C(2)-C(21)	1.502(8)	C(1)-O(1)	1.243(6)
N(5)-N(51)	1.403(6)	C(21)-C(22)	1.498(8)
C(22)-C(23)	1.493(10)		
C(5)-N(6)-C(6A)	121.4(4)	C(5)-N(4)-N(11)	119.2(4)
C(5)-N(4)-C(3)	127.0(5)	N(11)-N(4)-C(3)	107.0(4)
C(1)-N(11)-C(10A)	132.6(4)	C(1)-N(11)-N(4)	108.9(4)
C(10A)-N(11)-N(4)	118.5(4)	N(6)-C(5)-N(5)	122.5(5)
N(6)-C(5)-N(4)	120.0(5)	N(5)-C(5)-N(4)	117.5(5)
C(7)-C(6A)-C(10A)	119.8(5)	C(7)-C(6A)-N(6)	120.6(5)
C(10A)-C(6A)-N(6)	119.6(5)	C(8)-C(7)-C(6A)	119.1(5)
C(7)-C(8)-C(9)	121.9(5)	C(10)-C(9)-C(8)	118.7(5)
C(10)-C(9)-C(91)	119.7(5)	C(8)-C(9)-C(91)	121.5(5)
C(9)-C(10)-C(10A)	120.4(5)	C(6A)-C(10A)-C(10)	120.0(5)
C(6A)-C(10A)-N(11)	117.3(4)	C(10)-C(10A)-N(11)	122.7(5)
O(3)-C(3)-C(2)	134.6(5)	O(3)-C(3)-N(4)	118.4(5)
C(2)-C(3)-N(4)	107.0(5)	C(3)-C(2)-C(1)	110.2(5)
C(3)-C(2)-C(21)	125.2(5)	C(1)-C(2)-C(21)	124.5(5)
O(1)-C(1)-N(11)	121.8(5)	O(1)-C(1)-C(2)	131.3(5)
N(11)-C(1)-C(2)	106.8(4)	C(5)-N(5)-N(51)	119.1(4)
C(22)-C(21)-C(2)	115.6(5)	C(23)-C(22)-C(21)	113.7(6)

Table 4.13 Crystallographic data for VI·$(CH_3)_2SO$.

Formula	$C_{15}H_{15}N_5O \cdot C_2H_6SO$
Formula weight	359.45
Crystal colour, shape, size (mm)	colourless needle,0.3x0.2x0.25
Space group	$P\bar{1}$
λ (Å)	0.71073
Unit cell parameters (Å, °)	a = 9.532(2) α=70.53(3)
	b = 9.692(4) β=80.45(3)
	c = 12.370(4) γ=81.58(2)
Volume (Å³)	1057.4(6)
Z	2
D_{calc} (g/cm³)	1.129
Index ranges	$-1 \leq h \leq 10$, $-9 \leq k \leq 9$, $-13 \leq l \leq 13$
Max 2θ (°)	45.0
Temperature (°C)	25
Absorption coeffient (mm⁻¹)	0.171
F(000)	380
Reflections collected	2941
Independent reflections	2685 (R_{int} = 0.0652)
Reflections used	2685
No. Of parameters refined	253
Final R indices [$I > 2\sigma(I)$]	R_1=0.0538, wR_2=0.1124
Final R indices (all data)	R_1=0.1201, wR_2=0.1318
Goodness-of-fit on F^2, S	0.818
Data:parameter ratio	10.61:1
Largest difference peak (e Å⁻³)	0.211
Largest difference hole (e Å⁻³)	-0.258

Table 4.14 Atomic coordinates (x 10^4) and equivalent isotropic displacement parameters (Å^2 x 10^3) for VI·$(CH_3)_2SO$.

	x	y	z	U_{eq}
N(4)	5915(4)	6955(4)	6389(3)	39(1)
C(10A)	3858(5)	8705(5)	6401(4)	35(1)
O(3)	8095(4)	5533(4)	6675(3)	53(1)
C(5)	5703(5)	6845(5)	5375(4)	36(1)
N(5)	6607(4)	5913(4)	4964(3)	42(1)
C(3)	7119(5)	6338(5)	7034(4)	40(1)
N(6)	4623(4)	7674(4)	4847(3)	38(1)
C(2)	6830(5)	6840(5)	7984(4)	41(1)
O(1)	4879(4)	8318(4)	8667(3)	60(1)
N(51)	6553(4)	5864(4)	3865(3)	43(1)
N(11)	4907(4)	7751(4)	6989(3)	42(1)
C(10)	2922(5)	9652(5)	6890(4)	40(1)
C(1)	5521(6)	7676(5)	7983(4)	45(1)
C(7)	2678(6)	9611(5)	4710(4)	46(1)
C(91)	785(6)	11554(6)	6841(5)	64(2)
C(21)	7865(6)	6600(6)	8845(4)	59(2)
C(9)	1855(5)	10567(5)	6282(4)	47(1)
C(6A)	3717(5)	8685(5)	5313(4)	35(1)
C(8)	1762(5)	10551(5)	5188(4)	48(1)
C(53)	7560(6)	4877(6)	2357(4)	62(2)
C(52)	7515(5)	4956(5)	3553(4)	43(1)
C(51)	8641(5)	4020(6)	4250(4)	55(2)
C(22)	8788(6)	7890(7)	8539(5)	75(2)
C(23)	9772(7)	7678(7)	9433(5)	99(2)
S(1)	3947(2)	7081(2)	2081(1)	48(1)
C(24B)	2609(6)	7633(6)	1152(4)	67(2)
C(24A)	5184(6)	8388(6)	1276(4)	59(2)
O(2)	3299(4)	7554(4)	3117(3)	59(1)

*U_{eq} is defined as one third of the trace of the orthogonalized U_{ij} tensor.

Table 4.15 Bond lengths [Å] and angles [°] for VI·(CH$_3$)$_2$SO.

N(4)-C(5)	1.344(5)	N(4)-N(11)	1.413(5)
N(4)-C(3)	1.448(6)	C(10A)-N(11)	1.381(5)
C(10A)-C(6A)	1.381(6)	C(10A)-C(10)	1.398(6)
O(3)-C(3)	1.245(5)	C(5)-N(5)	1.323(5)
C(5)-N(6)	1.328(5)	N(5)-N(51)	1.385(5)
C(3)-C(2)	1.389(6)	N(6)-C(6A)	1.416(5)
C(2)-C(1)	1.384(6)	C(2)-C(21)	1.510(6)
O(1)-C(1)	1.244(5)	N(51)-C(52)	1.280(5)
N(11)-C(1)	1.423(6)	C(10)-C(9)	1.389(6)
C(7)-C(6A)	1.372(6)	C(7)-C(8)	1.377(6)
C(91)-C(9)	1.534(6)	C(21)-C(22)	1.541(7)
C(9)-C(8)	1.376(6)	C(53)-C(52)	1.500(6)
C(52)-C(51)	1.490(7)	C(22)-C(23)	1.510(7)
S(1)-O(2)	1.511(3)	S(1)-C(24B)	1.764(5)
S(1)-C(24A)	1.787(6)		
C(5)-N(4)-N(11)	121.8(4)	C(5)-N(4)-C(3)	128.6(4)
N(11)-N(4)-C(3)	109.6(3)	N(11)-C(10A)-C(6A)	118.5(4)
N(11)-C(10A)-C(10)	121.8(4)	C(6A)-C(10A)-C(10)	119.7(4)
N(5)-C(5)-N(6)	124.2(4)	N(5)-C(5)-N(4)	117.0(4)
N(6)-C(5)-N(4)	118.7(4)	C(5)-N(5)-N(51)	120.1(4)
O(3)-C(3)-C(2)	135.5(5)	O(3)-C(3)-N(4)	119.5(4)
C(2)-C(3)-N(4)	104.9(4)	C(5)-N(6)-C(6A)	121.7(4)
C(1)-C(2)-C(3)	111.0(4)	C(1)-C(2)-C(21)	124.9(4)
C(3)-C(2)-C(21)	124.0(5)	C(52)-N(51)-N(5)	114.0(4)
C(10A)-N(11)-N(4)	118.3(3)	C(10A)-N(11)-C(1)	132.8(4)
N(4)-N(11)-C(1)	105.7(4)	C(9)-C(10)-C(10A)	120.0(4)
O(1)-C(1)-C(2)	131.2(5)	O(1)-C(1)-N(11)	120.1(5)
C(2)-C(1)-N(11)	108.7(4)	C(6A)-C(7)-C(8)	120.3(4)
C(2)-C(21)-C(22)	112.5(4)	C(8)-C(9)-C(10)	119.0(5)
C(8)-C(9)-C(91)	121.0(5)	C(10)-C(9)-C(91)	120.0(5)
C(7)-C(6A)-C(10A)	119.9(4)	C(7)-C(6A)-N(6)	120.6(4)
C(10A)-C(6A)-N(6)	119.4(4)	C(9)-C(8)-C(7)	120.9(5)
N(51)-C(52)-C(51)	125.8(4)	N(51)-C(52)-C(53)	117.2(5)

Table 4.15 Bond lengths [Å] and angles [°] for VI·$(CH_3)_2SO$. (Cont'd)

C(51)-C(52)-C(53)	116.9(4)	C(23)-C(22)-C(21)	112.3(5)
O(2)-S(1)-C(24B)	104.7(2)	O(2)-S(1)-C(24A)	105.4(2)
C(24B)-S(1)-C(24A)	99.2(3)		

Chapter 5

Contrast Agents and Relaxivity Measurements: Gd(EDTA)⁻ and Gd(DTPA)²⁻

The development of contrast agents to be used for MRI has been the subject of numerous publications in recent years. Since Gd(III) is a nine-coordinate, spin 7/2, paramagnetic ion,[47] with high relaxivity in aqueous solution, it has been an early target of study. Polyamino polycarboxylic acids such as diethylenetriaminepentaacetic acid (DTPA) and ethylenediaminetetraacetic acid (EDTA) have been among the chelating agents used in such studies. However, gadolinium complexes of these ligands are salts under physiological conditions, and the requirement of nonparamagnetic cationic counterions increases the osmolarity of the solution. According to Baxter, et al.,[48] the adverse effects of ionic chelates are always higher than those of nonionic ones at the same concentration. Minimum osmolality is predicted for a neutral complex, which would behave in aqueous solution as one particle. In order to produce neutral complexes, researchers have been derivatizing DTPA at two of the carboxylic acid moieties. Usually, some thermodynamic stability is sacrificed with the derivatized Gd(III) complexes, but a compensation may be made with increased site specificity. Also, the T_1 relaxivity may either decrease or increase, depending on the nature of the derivative. The next section reviews the current research in this area.

115

5.1 Neutral DTPA - Type Gd(III) Complexes as Potenial Contrast Agents

The diagnostic potential of paramagnetic agents was first demonstrated by Carr *et al.*[49] Gd(III) diethylenetriaminepentaacetate ($[Gd(DTPA)(H_2O)]^{2-}$) was administered intravenously to patients with cerebral tumours, providing enhancement of the lesion in the region of capillary breakdown. The X-ray structure of the complex, which was crystallized from water, showed that the Gd(III) ion had a coordination number of nine.[50] The ion is coordinated by three amino nitrogens and five carboxylic oxygens from the acetate moieties forming a distorted mono-capped square antiprism around Gd(III). A water molecule forms the cap above the large square face of the antiprism ($Gd-OH_2 = 3.06$ Å). The coordination of Gd(III) in solution was deduced from NMR studies of corresponding Ln(III) complexes. The Ln(III) complexes of a particular ligand are usually almost isostructural, so results were indicative of the coordination of the Gd-DTPA complex. In solution, Ln-DTPA undergoes a dynamic exchange between two enantiomers.[51,52] The isomerization involves exchanges of coordinated terminal acetates between the top and bottom faces of the square antiprismatic complex, which is possible because of the conformational mobility of the ethylene bridges. The conformational interconversions lead to a pseudomirror plane through the backbone of the middle acetate group.[53] The Gd-DTPA complex has a very high stability constant ($\log K_f = 23$),[54] which largely limits the formation of free Gd(III) ions or ligand, both of which can be toxic. The complex is very soluble in water and has a T_1 relaxivity (R_1) of 4.71 $mM^{-1}s^{-1}$, which aids its usefulness as a contrast agent.[55]

A drawback of the Gd(DTPA) complex is that it has a negative charge, which,

as previously mentioned, results in a relatively high osmolarity under physiological conditions and consequently undesired side effects. Therefore, bis(amide) analogues, which are shown in **Figure 5.1**, have recently been introduced as alternatives. A summary of the R_1 values of the DTPA derivatives with Gd(III) can be found in **Table 5.1**.

One of the first bis(amide) analogues to be pursued was [Gd-DTPA-BMA)(H$_2$O)] (refer to **Figure 5.1**) as a nonionic alternative to [Gd(DTPA)]$^{2-}$.[56] The crystal structure of the Dy(III) analogue to the Gd-DTPA-BMA complex shows that DTPA-BMA acts as an octadentate ligand (like the parent DTPA^{5-}) by using three nitrogens, three carboxylates and two amidic carbonyls as donor groups.[57] The ninth coordination position of the lanthanide ion is occupied by a water molecule which is exchanging with the bulk water and in turn contributes to the paramagnetic relaxation of the bulk water.

The crystal structure of Gd-DTPA-BEA shows a similar coordination as the Dy-DTPA-BMA complex, with the amide carbonyl oxygens playing a prominent role in the metal ion coordination.[58] The gadolinium ion is in a nine-coordinate ligand environment comprised of three amine nitrogen atoms, three carboxylic acid oxygen atoms, two amide oxygen atoms, and one water molecule. The asymmetric unit contains six additional water molecules, which form a hydrogen bond network with the coordinated water molecule, and the three uncoordinated carboxylic acid oxygen atoms. The coordination geometry is best described as a distorted tricapped trigonal prism with the outer amine nitrogen atoms and the coordinated

DTPA	OH
DTPA-BMA	NHCH$_3$
DTPA-BEA	NHCH$_2$CH$_3$
DTPA-BPA	NHCH$_2$CH$_2$CH$_3$
DTPA-BP^{i}A	NHCH(CH$_3$)$_2$
DTPA-BBu^{i}A	NHC(CH$_3$)$_3$
DTPA-BBzA	NHCH$_2$C$_6$H$_6$
DTPA-BPhA	NHC$_6$H$_6$
DTPA-BPEA	NHCH$_2$CH$_2$C$_6$H$_6$
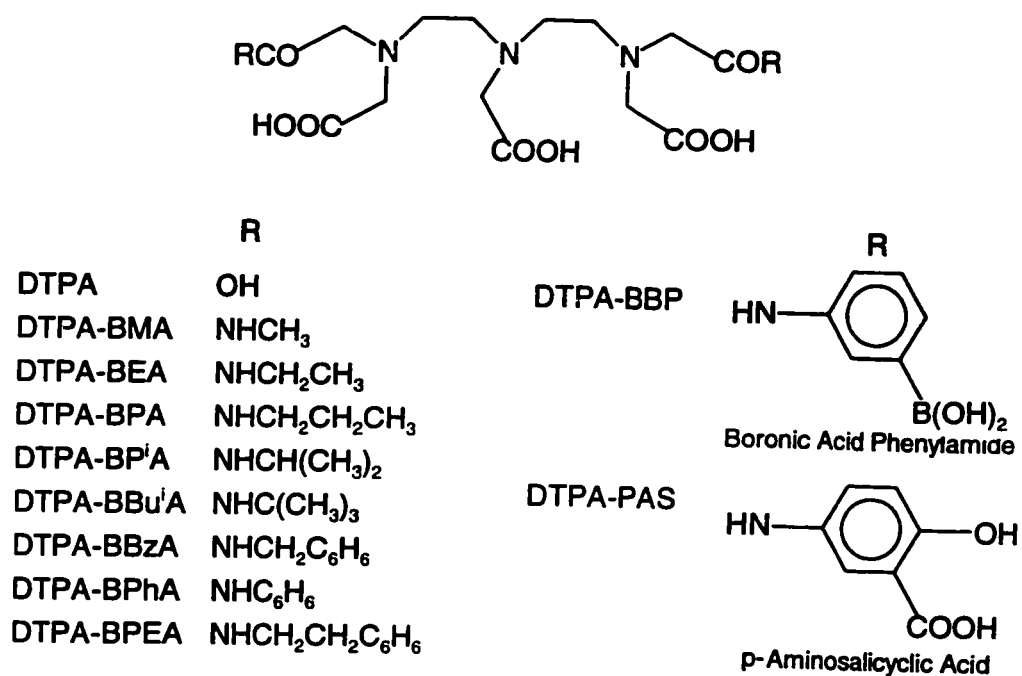
Figure 5.1 Octadentate DTPA derivatives that form neutral complexes with Gd(III).

Table 5.1 Relaxivities of DTPA and DTPA-bisamide complexes with Gd(III).

Ligand	Relaxivity (mM^{-1}s^{-1})[a]	Reference
DTPA	4.71	55
DTPA-BMA	4.42	56
DTPA-BEA	4.80	58
DTPA-BP^{i}A	4.27	61
DTPA-BBu^{i}A	5.09	60
DTPA-BBzA	4.50	60
DTPA-BPhA	4.17	62
DTPA-BPEA	4.86	60
DTPA-PAS	4.60	63
DTPA-BBP	4.60	64

[a] freq., 20MHz, 25°C

water oxygen atom forming the three rectangular face caps. The distances between the gadolinium ion and the amide oxygen atoms are 2.425(3) Å and a short 2.362(3) Å. The bond lengths show a trend of short metal-carboxylate bonds, which are from 2.351(3) Å to 2.384 (3) Å (0.03-0.04 Å shorter than the sum of their ionic radii)[59] and long metal-nitrogen bonds, which are from 2.645(4) Å to 2.759(4) Å (0.08-0.19 Å longer than the sum of their ionic radii). This trend is also seen in the crystal structure of Gd-DTPA-BBzA, where the metal-amine bond lengths range from 2.600(7) to 2.751(8) Å and the metal-carboxylate bond lengths range from 2.368(6) to 2.384(7) Å.[60] This structure also shows the coordination geometry around the gadolinium to be a distorted tricapped trigonal prism, with coordination to the metal through the amide oxygen atoms.

Peters, et al.[61] determined the structure and the dynamics of the Ln(III) complexes of DTPA-BP[i]A in aqueous solution by studying their multinuclear NMR. The results indicated that there was one water molecule in the inner coordination sphere of the complex, and the ligand coordinated the metal in an octadentate fashion via the three nitrogen atoms of the diethylenetriamine backbone, three carboxylate oxygens, and the two amide oxygens. In addition, four possible diastereomeric pairs occur in aqueous solution. The conformational mobility of the ethylene bridges leads to an exchange between the diastereomers, a mechanism which is similar to that observed in the corresponding Ln-DTPA complexes.[51,52] A racemization process at the terminal nitrogen atoms was observed, which involves decoordination and N-inversion, as a result of the relatively weak coordinating strength of the amide group with respect to the carboxylate group. In the DTPA

complexes, this process was not observed on the NMR timescale.

It is quite likely that other Gd-DTPA(bis-amide) complexes are fluxional on the NMR timescale. The similarity in the R_1 values (see **Table 5.1**) indicate that there is one coordinated water molecule, and the octadenticity of the ligand is maintained. Bligh et al.,[14] showed that the metal coordination of the amide group was through the carbonyl oxygen atom for the DTAP-BP^{i}A, DTPA-BBu^{i}A, and DTPA-BPEA Gd(III) complexes by observing that the carbonyl stretching frequencies were shifted by about 20-90 cm^{-1} to lower energy in the infrared spectra. Similar coordination has been assumed for the DTPA-BPhA,[62] DTPA-BPAS,[63] and DTPA-BBP[64] Gd(III) complexes.

A major limitation in the use of Gd-DTPA-bisamide complexes as contrast agents for MRI could be their relatively low stability constants, which are all in the log K_f =16 range,[65] about 6 orders of magnitude smaller than the corresponding value for the DTPA complex. The remarkable difference in stabilities between the DTPA and the DTPA-bisamide Gd(III) complexes is related to the decreased ability of the carbonyl group of the amides to coordinate to the Gd(III) ion with respect to the carboxylates. This shortcoming may justify some concerns about the potential release in body fluids of the highly toxic Gd(III) and free ligand. However, since the release of the metal ion presumably occurs through an exchange mechanism involving Zn(II), Cu(II), and/or Ca(II) ions, it was suggested[65] that the chemotoxicity of the Gd(III) complexes is better related to the selectivity constant of the ligand (a function of its stability constant with Gd(III) and other metal ions) rather than to the Gd pK_f values only. In fact, it has been reported that the Gd-DTPA-BMA complex

has a very high *in vivo* stability, as it is excreted in urine without any metabolic alteration.[66]

The addition of substituents to Gd-DTPA complexes can have a varying effect on the R_1 value because of changes in τ_c, which affects T_{1M}. As defined in equation 1-4, τ_c is determined by the shortest of the three correlation times, τ_R, T_{1e}, and τ_M. A number of observations[67] on polyaminocarboxylate complexes of Gd(III) have established that, at magnetic fields higher than 0.25 T, R_1 values are essentially determined by the molecular reorientational time, τ_R, in addition to the number of coordinated water molecules in the inner sphere, or the q value. Aime *et al.*[68] have postulated that the increased molecular weight of a complex (even a difference of 200 g/mol) should cause an elongation of τ_R, which would dominate the molecular correlation time τ_c at higher fields (0.5-1.5 T) and result in a higher relaxivity in the high frequency observation range (10-50 MHz). Usually, for a small Gd(III) complex, τ_R is about 10^{-10} s, whereas T_{1e} and τ_M are significantly longer.[67,69,70] However, if τ_M becomes so long as to approach the value of T_{1M} (~10^{-6} s) it may largely influence the solvent proton relaxation rate, through equation 1-2 and determine a lower value of R_1. Aime *et al.* were able to show the quenching effect of a long τ_M with Gd-DTPA-BMA, for which $T_{1M} \sim \tau_M$, by comparing it with Gd-DTPA, where $T_{1M} \gg \tau_M$. The temperature was varied from 0 to 100°C and the relaxivities were determined at various points at 20 MHz.[68] Both τ_R and τ_M increase with decreasing temperature, thus resulting in an opposite temperature dependence of τ_M and T_{1M}. The results showed that the R_1 value of Gd-DTPA steadily decreased

as the temperature increased from 5 to 30°C whereas Gd-DTPA-BMA showed no change in R_1 in the same temperature range. The same behaviour was seen with Gd-DTPA-BPhA.[62] It was suggested that the elongation of τ_M may be based on the decrease of the residual charge on the metal ion upon transformation of carboxylate to amide functionalities, thus causing a stronger $Gd-OH_2$ bond, which then results in a decrease of the water exchange rate. The results show, however, that at the human body temperature, this parameter does not introduce any quenching effect on the observed relaxivity.

In 1993, roughly 25% of all MRI procedures were performed in the United States using a contrast agent.[71] The complex Gd-DTPA was the first contrast agent in clinical use[72] and so far it has been used safely for more than six years, proving particularly helpful for the diagnosis of brain and spine lesions.[71] The non-ionic Gd-DTPA-BMA has also been recently introduced.[73] Both of these contrast agents diffuse from the vascular space into the interstitial fluid, do not enter cells, and are excreted almost entirely through the kidneys. While this may be appropriate for certain pathologies, it is clear that there are many other tissues and organs that can be targeted for enhanced imaging. This is the goal of much of the research in the MRI contrast agent field today.

5.2 Gd-EDTA and Derivatives as Contrast Agents

Much less is known about derivatives of Gd-EDTA as potential contrast agents than there is known about derivatives of Gd-DTPA. The relaxivity of Gd-EDTA is 7.6 $mM^{-1}s^{-1}$ at 20 MHz and 25°C,[74] which is higher than that of Gd-DTPA

under the same conditions. The increased relaxivity is mainly due to a q value of 2 or 3 in solution, depending on the temperature,[75] and 3 in the solid state.[76] The main reason that Gd-EDTA derivatives have not been investigated as potential contrast agents is because of the instability of Gd-EDTA itself *in vivo*. Its log K_f is 17.4, but it has an in vivo toxicity comparable to $GdCl_3$ (LD_{50} ~ 0.5 mmol/kg; *cf.* Gd-DTPA: LD_{50}= 10-20mmol/kg).[77] The reason for the high toxicity is revealed by the crystal structure of the complex (*vide infra*).[75] The ligand occupies roughly one hemisphere of the ion, leaving the other side relatively open for coordination by labilizing ligands or for oxo-bridged dimer formation, thus promoting the dissociation of the complex. However, Meares *et al.* discovered that substituting the EDTA ligand decreased its dissociation rate from [111]In(III).[78] The investigators attributed the apparent increased stability to steric effects, which decrease rearrangement and dissociation rates.

There is clearly more research needed in the area of substituted Gd-DTPA and Gd-EDTA complexes as potential contrast agents. The rest of this chapter presents the crystal structure of $Gd(EDTA)K \cdot 8H_2O$, and the methods used to determine T_1 relaxivity values of Gd(III) complexed with DTPA and EDTA derivatives, as presented in **Chapters 6** and **7**. The method is evaluated here with $Gd(EDTA)^-$ and $Gd(DTPA)^{2-}$, and the results are compared to T_1 times reported in the literature.

5.3 Interpretation of Relaxation Times at High Field

The best way to determine the relaxivity of a metal complex is to measure the magnetic field dependence of water proton relaxation rates by a technique called NMR Dispersion (NMRD) and fitting the data using established theories.[79] However, a major obstacle in the application of this technique is the necessary instrumentation, *i.e.* the field-cycling relaxometer, which is not commercially available. Aime *et al.*[80] have proposed a relatively simple procedure that allows the determination of R_1 at a single, high magnetic field. The inner-sphere $1/T_1$ value is given by equation 1-2, and T_{1M} is expressed by the well known Solomon-Bloembergen equations (equation 1-3). From X-ray crystallographic and NMR proton relaxation studies of Gd(III) complexes,[20] it was concluded that the parameters involved in the theory of paramagnetic relaxation fall in the following values or range of values: $\tau_R = 4\text{-}8 \times 10^{-11}$ s; $\tau_M = 0.8\text{-}5 \times 10^{-9}$ s; $T_{1e} \geq 1 \times 10^{-7}$ s (at 270 MHz); $r = 3.0\text{-}3.2$ Å. From the values of these parameters it follows that, for Gd(III) complexes at high magnetic fields, T_{1M} is of the order of 1×10^{-6} s and this implies that $\tau_M \ll T_{1M}$ and equations 1-2 and 1-3 can be written in the simplified forms:

$$\frac{1}{T_1} = \frac{P_M q}{T_{1M}} \tag{5-1}$$

$$\frac{1}{T_{1M}} = (\frac{\mu_o}{4\pi})^2 \frac{6S(S+1)\gamma_I^2 g^2 \beta^2}{15 r^6} \tau_c \tag{5-2}$$

where S is the total electron spin of the metal ion, γ_I is the proton gyromagnetic ratio, g is the electronic g-factor, β is the Bohr magneton, μ_o is the permeability constant, and τ_c is defined by equation 1-4. Furthermore, the condition $1/\tau_R \gg 1/T_{1e}$, $1/\tau_M$ holds and the rotational tumbling time, τ_R, may be assumed to be the actual correlation time at high magnetic field.

In principle, an estimate of τ_R for isotropic tumbling may be obtained from the Stokes-Debye formula (equation 1-6). James has discussed the problem of using the viscosity parameter η, which relates to macroscopic *translational* properties, to predict τ_R; a knowledge of *rotational* microviscosity, which unfortunately is less understood, would actually be required to accurately estimate τ_R.[81] Instead, Aime's method is based upon the assumption that the rotational correlation time for the water protons in the first hydration sphere of the paramagnetic ion is the same as that for the other nuclei in the complex, in particular, for the carbon atoms of the methylene groups of the ligand. The correlation time may then be evaluated from the dipolar ^{13}C spin-lattice relaxation rate (R_{1c}^{DD}) using equation 5-3:[82]

$$\tau_R = (\frac{\mu_o}{4\pi})^2 \frac{R_{1c}^{DD} r^6}{2\gamma_C^2 \gamma_H^2 \hbar^2}$$

(5-3)

where r is the CH bond length. Separation of the dipolar contribution[83] was obtained using the experimentally observed NOE enhancement factor (5-4):

$$\frac{R_{1c}^{DD}}{R_{1c}} = \frac{NOE}{1.988}$$

(5-4)

where R_{1c} is the total ^{13}C spin-lattice relaxation rate measured for the analogous diamagnetic La(III) complex. The NOE determines how much of a dipolar contribution is responsible for the ^{13}C relaxation rate. This is the method chosen to evaluate the complexes presented in this thesis.

5.4 Results and Discussion

The crystal structure of the Gd-EDTA complex has been solved before as the sodium salt.[84] The complex crystallized according to the orthorhombic space group *Fdd2*, as predicted by Hoard.[76] The compound presented here, seen in **Figure 5.2** is isostructural to the corresponding sodium salt, with three water molecules (O(1), O(2), and O(3)) bound directly to the Gd(III), and five lattice water molecules. The bond lengths, bond angles, atom positions are very similar to the sodium salt.[83] The bond lengths between the metal and the protons of Gd-OH$_2$ for the bound waters O(1), O(2), and O(3) range from 2.8-2.9Å. There is an increase in the cell volume from the sodium salt to the potassium analogue of about 4%Å^3. High temperature factors that were observed for three of the lattice waters observed in the Na salt are present in the K salt, although in this case it has proved possible to separate each of two water molecules, (O(6)/O(6A) and O(8)/O(8A)), into two sites and

Figure 5.2 The structure of **K[Gd(EDTA)(H₂O)₃]·5H₂O**. The displacement ellipsoids are at 30% probability level.
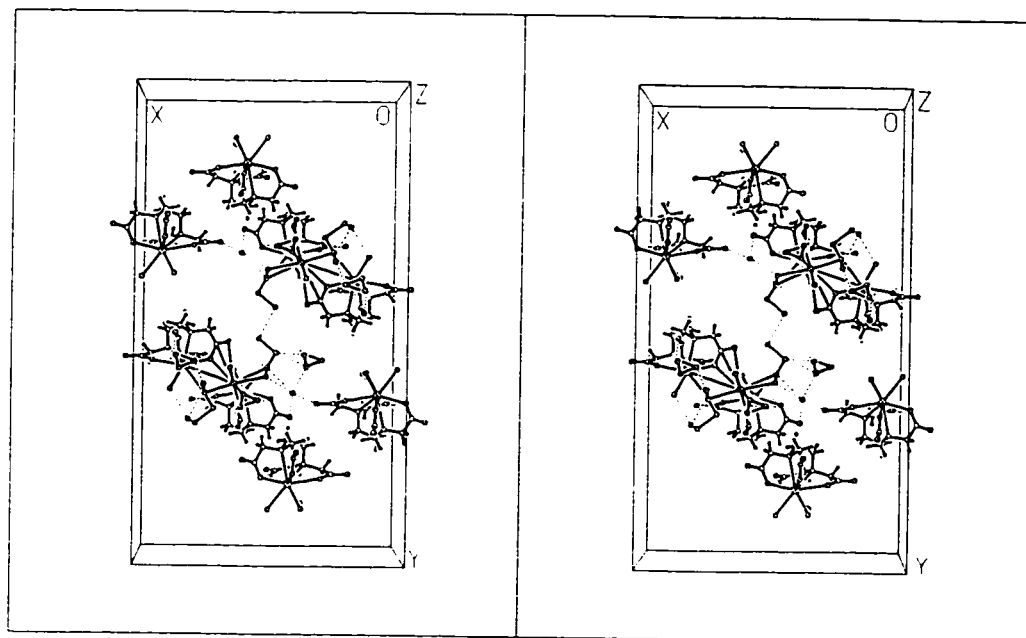
Figure 5.3 The stereoview packing plot of **K[Gd(EDTA)(H$_2$O)$_3$]·5H$_2$O** within the unit cell. Half of the molecules have been removed for clarity.

refine the occupancy of these sites. The water molecule O(5) proved much more difficult to handle. There was clearly considerable disorder present, and up to four sites showed electron densities of 4-5 eÅ^{-3}. Many attempts were made at varying positions and occupancies, with little success. Eventually, atoms were placed at positions shown by the electron density peaks and these positions were not refined. The occupancies were refined with all atoms given the same temperature factor. Even this was a problem, since initially it did not prove possible to refine the occupancies of all four atoms at once. Finally, the occupancies of the three largest peaks were refined (all three atoms with the same temperature factor) and the remaining site was given a fixed occupancy that made the temperature factor close to that of the other three atoms. This was adjusted after each set of refinement cycles. When refinement had ceased, all four atoms were included in the occupancy variation and the refinement proceeded satisfactorily. The atom positions of the disordered water molecules showed that some K...O distances were rather short, which suggested that the potassium atom was disordered. The temperature factors of the potassium atom were quite high, as well. Thus, the change from the sodium to potassium ions in the structure seems to have decreased the efficiency of what was already poor packing, increasing the amount of disorder. The stereoview diagram of the packing can be seen in **Figure 5.3**, where half of the molecules in the unit cell have been removed in order to visualize the hydrogen bonding, which is extensive.

The T_1 relaxation experiments were performed on various concentrations of Gd-EDTA and Gd-DTPA. A plot of the concentration of each sample versus the

relaxation rates is shown in **Figure 5.4**. The slope, minus the relaxivity of the blank, gives the relaxivity of each complex in $mM^{-1}s^{-1}$.[30] **Table 5.2** compares the results with those achieved by Aime. A full NOE effect was observed for the methylene carbon atoms in both the La-EDTA and La-DTPA, which implies fast tumbling of the complexes and 100% dipole-dipole relaxation. Therefore, the ^{13}C relaxation rate (R_{1c}) is used in place of R_{1c}^{DD} in equation **5.3**. The R_{1c} and τ_R values are shown in **Table 5.3**, along with the literature results. A C-H value of 1.08 Å was used for r. A comparison between the results presented here and those reported in the literature shows excellent agreement.

Results

Complex	Slope ($mM^{-1}s^{-1}$) - Blank ($mM^{-1}s^{-1}$)		= Relaxivity ($mM^{-1}s^{-1}$)
Gd-EDTA	6.3(2)	0.1	6.2
Gd-DTPA	4.2(2)	0.1	4.1
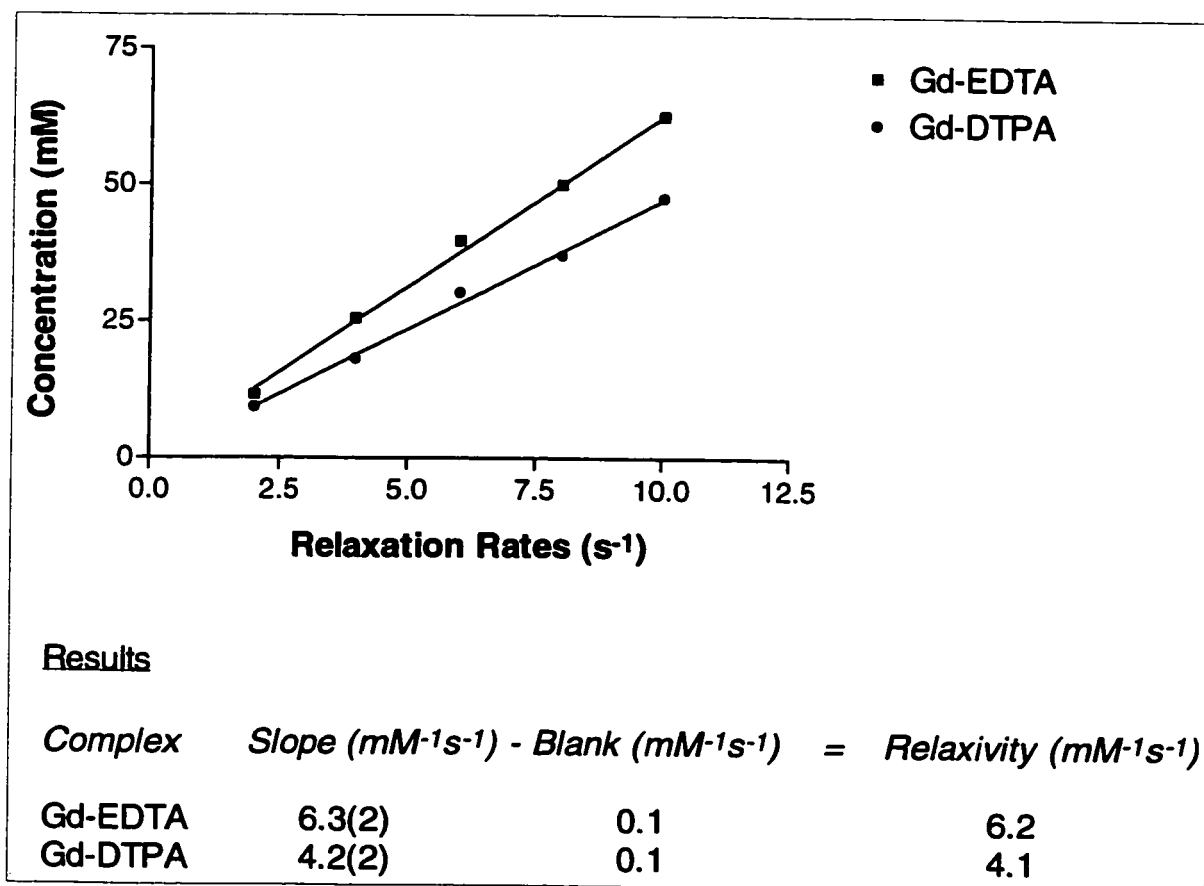
Figure 5.4 The relaxivities of Gd-EDTA and Gd-EDTA in 100% D_2O at 300 MHz and 27°C.

The substitution of τ_R for τ_c in Eq. **5.2**, and the use of reasonable metal-proton (r) distances for Gd-OH$_2$ allow the determination of 1/T$_{1M}$, and then the determination of q from Eq. **5.1**. The r values were toggled to give a reasonable q value. The results, presented in **Table 5.4**, confirm the validity of the experiment, as well as assign values to the r and q parameters.

Table 5.2 Relaxivities of Gd-EDTA and Gd-DTPA (mM^{-1}s^{-1}) Complexes in 100% D$_2$O at 27°C and pH 7.2.

Complex	R$_1$(mM^{-1}s^{-1})	Reference R$_1$
Gd-EDTA	6.2[a]	6.0[b]
Gd-DTPA	4.1[a]	3.7[b]

[a] This work; 300 MHz. [b] Reference 30; 400 MHz.

Table 5.3 Experimental ^{13}C Longitudinal Relaxation Rates and Calculated Values of the Rotational Correlation Times for Aqueous solutions of La(III) Complexes at 27°C and pH 7.2.

Complex	R$_{1c}$ (s^{-1})	R$_{1c}$[a] (s^{-1})	τ_R (ps)	τ_R[a] (ps)
La-EDTA	3.1	2.8	72	65
La-DTPA	3.4	3.1	79	73

[a] Reference 30.

Table 5.4 Calculated Parameters for the Complexes in 100%D_2O at 27°C and pH 7.2.

Complex	q	q[a]	r (Å)	r[a] (Å)
Gd-EDTA	2	2	2.95	3.15
Gd.DTPA	1	1	2.80	3.14

[a] Reference 30.

5.5 Experiments

Crystal Structure of $K[Gd(EDTA)(H_2O)_3] \cdot 5H_2O$

Crystals of the compound were prepared by refluxing Gd_2O_3 with EDTA dipotassium salt in water, and then adjusting the pH to 6 with 1N HCl. Crystals were produced after slow evaporation of the water. A crystal was mounted on a glass fibre with epoxy glue. Unit cell determination and intensity data collection were performed on a Siemens P4 diffractometer with monochromatized Mo Kα radiation (λ=0.71073 Å). Unit cell parameters were refined by a least squares fit of angular parameters from 39 reflections ($3° \leq 2\theta \leq 55°$). The intensities were measured with a θ(crystal)-2θ(counter) scan. No signs of crystal decay or instrumental instability were observed during data collection. An absorption correction was applied via a ψ-scan. The structure was solved by direct methods and refined on F^2 by the method of full-matrix least squares. Hydrogen atoms were placed in calculated positions on the ligand, and water hydrogen atoms were not assigned at all. Temperature factors of non-hydrogen atoms were refined anisotropically; some of the oxygen atoms from the water molecules were refined isotropically and some of their site occupancies were refined. Hydrogen atoms were not refined, but rode on

the atoms to which they were attached. Details of crystal data collection and structure solution are listed in **Table 5.5**. The atomic positional parameters are given in **Table 5.6** and interatomic distances and angles are given in **Table 5.7**. The structure of the molecule is shown in **Figure 5.2** and the molecular packing is shown in **Figure 5.3**.

T₁ Relaxation Experiments

Longitudinal relaxation times were determined with the spin inversion recovery technique on a Bruker AC-300 Fourier transform spectrometer. Each measurement was repeated at least twice to determine compliance. The spectra were recorded without spinning at 27°C. A 20 mM stock solution of the Gd(III) ion and DTPA or EDTA was made by adding the appropriate amount of the hexahydrate $GdCl_3$ and the free acid of the ligand. The pH was adjusted to 6.5-7.2 with 10% $NaOD/D_2O$ and 10% DCl/D_2O. Solutions of 2mM, 4mM, 6mM, 8mM, and 10mM were prepared from the stock solution by dilution with D_2O. A blank of each ligand, without a paramagnetic metal, was prepared at a concentration of 6mM and the pH was adjusted to 6.7. The La(III) complexes were prepared with hexahydrate $LaCl_3$ at a concentration of 0.1 M for the EDTA complex, and 0.05 M for the DTPA complex. Solutions were degassed by bubbling dry nitrogen through them for 3 minutes.

Table 5.5 Crystallographic data for $K[Gd(EDTA)(H_2O)_3]\cdot 5H_2O$

Formula	$C_{10}H_{12}GdKN_2O_8\cdot 8H_2O$
Formula weight	628.69
Crystal colour, shape, size (mm)	colourless block, 0.50 x 0.40 x 0.40
Space group	Fdd2
λ (Å)	0.71073
Unit cell parameters (Å)	a = 19.827(4)
	b = 35.750(7)
	c = 12.268(2)
Volume (Å^3)	8695.7(5)
Z	16
D_{calc} (g/cm^3)	1.921
Index ranges	$-1 \leq h \leq 25$, $-1 \leq k \leq 46$, $-1 \leq l \leq 15$
Max 2θ (°)	55.0
Temperature (°C)	25
Absorption coeffient (mm^{-1})	3.320
$F(000)$	5008
Transmission factor (range)	0.130, 0.221
Reflections collected	3092
Independent reflections	2828 (R_{int} = 0.0343)
Reflections used[I > 2σ(I)]	2596
No. Of parameters refined	266
Final R indices [I > 2σ(I)]	R1=0.0477, wR2=0.1229
Final R indices (all data)	R1=0.0547, wR2=0.1277
Goodness-of-fit on F^2, S	1.178
Data:parameter ratio	9.76:1
Largest difference peak (e Å^{-3})	1.93
Largest difference hole (e Å^{-3})	-2.08

Table 5.6. Atomic coordinates (x 10^4) and equivalent isotropic displacement parameters (Å^2 x 10^3) for **K[Gd(EDTA)(H$_2$O)$_3$]·5H$_2$O**.

	x	y	z	U$_{eq}$
Gd(1)	852(1)	1546(1)	0	29(1)
C(1)	392(5)	1753(3)	-2523(13)	38(2)
O(11)	178(4)	1650(3)	-1575(7)	37(2)
O(12)	54(5)	1754(3)	-3364(9)	51(2)
C(2)	1144(6)	1858(4)	-2619(10)	44(3)
C(1')	2464(6)	1738(3)	-479(11)	39(2)
O(11')	2051(4)	1665(2)	264(7)	41(2)
O(12')	3085(4)	1741(3)	-345(8)	51(2)
C(2')	2192(6)	1800(4)	-1630(11)	40(3)
N(3)	1489(5)	1920(3)	-1601(9)	36(2)
C(4)	1497(7)	2330(3)	-1317(12)	44(3)
C(5)	822(7)	2471(4)	-945(15)	45(4)
N(6)	604(5)	2276(2)	93(11)	40(2)
C(7)	986(9)	2424(4)	1024(16)	55(4)
C(8)	1027(8)	2154(4)	1980(14)	52(3)
O(81)	995(5)	1818(2)	1777(9)	48(2)
O(82)	1107(10)	2283(4)	2910(12)	98(5)
C(7')	-125(7)	2336(4)	243(12)	52(3)
C(8')	-456(7)	2016(4)	886(14)	50(3)
O(81')	-221(4)	1697(3)	743(9)	46(2)
O(82')	-956(6)	2089(4)	1473(14)	84(4)
K	-1183(3)	1168(2)	896(4)	98(2)
O(1)	1328(4)	1046(2)	1168(8)	39(2)
O(2)	1354(5)	1094(3)	-1273(8)	45(2)
O(3)	77(4)	987(2)	-170(8)	40(2)
O(4)	1848(6)	2885(3)	3456(14)	72(3)
O(5)	-2158	823	1968	33(3)
O(5A)	-1577	957	2499	33(3)
O(5B)	-1381	656	2232	33(3)
O(5C)	-1480	694	3049	33(3)
O(6)	13(26)	1177(20)	3268(64)	131(10)
O(6A)	-38(19)	979(13)	2771(43)	131(10)
O(7)	-1040(9)	1538(4)	3032(19)	101(6)
O(8)	-2174(18)	2152(9)	714(33)	159(12)
O(8A)	-2879(47)	1845(25)	397(84)	159(12)

U$_{eq}$ is defined as one third of the trace of the orthogonalized U$_{ij}$ tensor.

Table 5.7. Bond lengths [Å] and angles [°] for K[Gd(EDTA)(H₂O)₃]·5H₂O.

Gd(1)-O(81')	2.376(9)	Gd(1)-O(11)	2.379(8)
Gd(1)-O(81)	2.405(11)	Gd(1)-O(11')	2.438(8)
Gd(1)-O(2)	2.456(9)	Gd(1)-O(1)	2.477(9)
Gd(1)-O(3)	2.528(7)	Gd(1)-N(6)	2.658(9)
Gd(1)-N(3)	2.691(10)	Gd(1)-K	4.394(4)
C(1)-O(12)	1.23(2)	C(1)-O(11)	1.29(2)
C(1)-C(2)	1.54(2)	C(2)-N(3)	1.44(2)
C(1')-O(12')	1.242(14)	C(1')-O(11')	1.25(2)
C(1')-C(2')	1.53(2)	C(2')-N(3)	1.459(14)
N(3)-C(4)	1.51(2)	C(4)-C(5)	1.50(2)
C(5)-N(6)	1.52(2)	N(6)-C(7)	1.47(2)
N(6)-C(7')	1.47(2)	C(7)-C(8)	1.52(2)
C(8)-O(81)	1.23(2)	C(8)-O(82)	1.24(2)
C(7')-C(8')	1.53(2)	C(8')-O(81')	1.25(2)
C(8')-O(82')	1.25(2)	C(8')-K	3.357(14)
O(81')-K	2.692(10)	O(82')-K	3.40(2)
K-O(5A)	2.246(5)	K-O(5B)	2.488(6)
K-O(5)	2.643(4)	K-O(3)	2.892(11)
K-O(7)	2.95(2)	K-O(5C)	3.193(6)
K-O(6A)	3.30(4)	O(5)-O(5A)	1.41
O(5)-O(5B)	1.68	O(5A)-O(5C)	1.17
O(5A)-O(5B)	1.19	O(5B)-O(5C)	1.03
O(6)-O(6A)	0.94(7)		
O(81')-Gd(1)-O(11)	76.9(3)	O(81')-Gd(1)-O(81)	70.5(3)
O(11)-Gd(1)-O(81)	137.6(3)	O(81')-Gd(1)-O(11')	141.5(3)
O(11)-Gd(1)-O(11')	128.9(3)	O(81)-Gd(1)-O(11')	72.2(3)
O(81')-Gd(1)-O(2)	139.1(3)	O(11)-Gd(1)-O(2)	79.3(3)
O(81)-Gd(1)-O(2)	142.6(3)	O(11')-Gd(1)-O(2)	78.7(3)
O(81')-Gd(1)-O(1)	106.4(3)	O(11)-Gd(1)-O(1)	142.9(3)
O(81)-Gd(1)-O(1)	73.9(3)	O(11')-Gd(1)-O(1)	71.2(3)
O(2)-Gd(1)-O(1)	74.9(3)	O(81')-Gd(1)-O(3)	70.5(3)
O(11)-Gd(1)-O(3)	73.5(3)	O(81)-Gd(1)-O(3)	117.8(3)
O(11')-Gd(1)-O(3)	137.9(3)	O(2)-Gd(1)-O(3)	71.1(3)

Table 5.7. Bond lengths [Å] and angles [°] for **K[Gd(EDTA)(H₂O)₃]·5H₂O**. (Cont'd)

O(1)-Gd(1)-O(3)	73.1(3)	O(81')-Gd(1)-N(6)	66.1(3)
O(11)-Gd(1)-N(6)	77.1(4)	O(81)-Gd(1)-N(6)	65.5(4)
O(11')-Gd(1)-N(6)	90.2(3)	O(2)-Gd(1)-N(6)	138.4(4)
O(1)-Gd(1)-N(6)	138.9(4)	O(3)-Gd(1)-N(6)	131.8(3)
O(81')-Gd(1)-N(3)	126.0(3)	O(11)-Gd(1)-N(3)	66.0(3)
O(81)-Gd(1)-N(3)	113.9(3)	O(11')-Gd(1)-N(3)	63.4(3)
O(2)-Gd(1)-N(3)	70.9(3)	O(1)-Gd(1)-N(3)	127.0(3)
O(3)-Gd(1)-N(3)	128.1(3)	N(6)-Gd(1)-N(3)	68.3(4)
O(81')-Gd(1)-K	32.0(2)	O(11)-Gd(1)-K	74.7(2)
O(81)-Gd(1)-K	90.3(2)	O(11')-Gd(1)-K	156.4(2)
O(2)-Gd(1)-K	109.2(2)	O(1)-Gd(1)-K	89.1(2)
O(3)-Gd(1)-K	38.7(2)	N(6)-Gd(1)-K	97.0(2)
N(3)-Gd(1)-K	140.0(2)	O(12)-C(1)-O(11)	125.1(9)
O(12)-C(1)-C(2)	117.6(13)	O(11)-C(1)-C(2)	117.2(11)
C(1)-O(11)-Gd(1)	126.2(7)	N(3)-C(2)-C(1)	115.5(11)
O(12')-C(1')-O(11')	123.6(12)	O(12')-C(1')-C(2')	118.1(11)
O(11')-C(1')-C(2')	118.2(9)	C(1')-O(11')-Gd(1)	125.3(8)
N(3)-C(2')-C(1')	110.9(10)	C(2)-N(3)-C(2')	112.8(11)
C(2)-N(3)-C(4)	110.8(10)	C(2')-N(3)-C(4)	106.3(9)
C(2)-N(3)-Gd(1)	109.5(6)	C(2')-N(3)-Gd(1)	108.7(7)
C(4)-N(3)-Gd(1)	108.6(8)	C(5)-C(4)-N(3)	112.9(10)
C(4)-C(5)-N(6)	110.8(10)		

Chapter 6

Amino Acid Derivatives of EDTA and DTPA as Potential Contrast Agents

The area of neutral, lipophilic imaging agents has been under-exploited compared to the charged, hydrophilic counterparts. Neutral and lipophilic potential contrast agents are of interest for a few reasons. For instance, they may be taken up by the liver in preference to the kidney, which would allow hepatobiliary imaging. They may also cross the blood brain barrier, which is a feat that is not possible for a charged, hydrophilic complex. In addition, large lipophilic groups, especially aromatic rings, may interact noncovalently with hydrophobic regions of membrane receptors or other transport proteins, which may allow a localization of the imaging agent in particular tissues or pathologies. Lauffer *et al.* has demonstrated this last feature by showing that there is a correlation between lipophilicity of a metal complex and albumin binding.[85]

The noncovalent binding of metal complexes to macromolecules *in vivo* has an added advantage to increased site specificity. The binding of the metal chelate to the macromolecule significantly increases the τ_R, which improves the R_1 and enhances the T_1-weighted MR image. This effect can also be seen when chelates are covalently attached to protein amino acid residues. For example, Lauffer *et al.* covalently attached EDTA and DTPA to amino groups on bovine serum albumin and

immunoglobulins, and then titrated the solution with a paramagnetic metal. The paramagnetic metal complex was thereby immobilized and the τ_R value was increased, which increased the value of R_1 by a factor of 2 to 10.[86,87] Aime *et al.*[64] also used this effect to determine whether Gd-DTPA-BBP (see **Figure 5.1**) had bound to glycated protein. The boronic functionality has the ability to form a stable linkage with cis-diol moieties of the sugar on the protein. As the adduct formed, the enhancement of the proton relaxation rate doubled, as a consequence of the increased τ_R.

This chapter presents the synthesis, characterization, and the proton relaxivity enhancement of benzylated amino acid monosubstituted EDTA and disubstituted DTPA ligands, each of which form neutral complexes with Gd(III). The ligands are shown in **Figure 6.1** with atom numbering. The amino acids that were chosen were glycine, phenylalanine, and tyrosine.

The choice of the amino acids allowed a study of the effects that subtle structural differences on metal complexes can have on the value of R_1. The glycine is not substituted at C(10), and therefore has slightly more hydrophilic character than phenylalanine, while the tyrosine has a hydroxyl group at C(16), which should lessen the lipophilicity compared to the phenylalanine complexes.
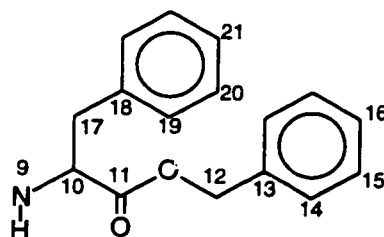
The differences in structure could also affect the biodistribution of the complexes, either because of solubility differences, receptor site recognition, or both. As mentioned above, the phenyl groups may increase the interaction of these complexes with membrane bound proteins. This property was examined in
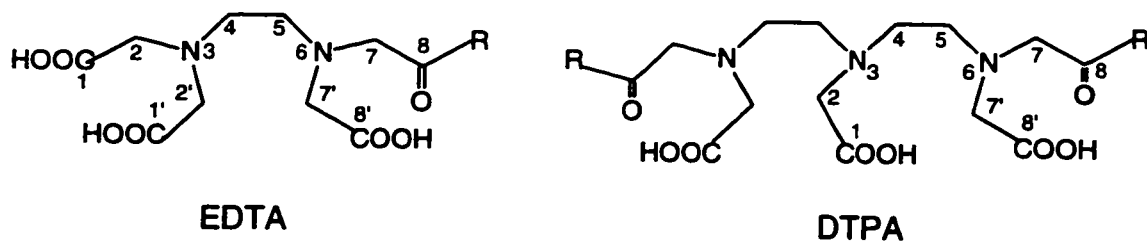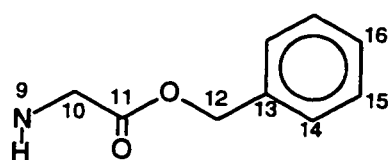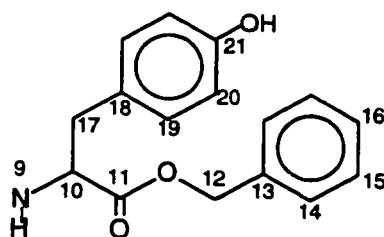
Figure 6.1 The EDTA and DTPA derivatives with atom numbering.

biodistribution and *in vivo* SPECT imaging studies of DTPA-GB with ^{111}In(III), found in **Chapter 8**.

6.1 Results and Discussion

The ligands were made by reacting one mole of EDTA-monoanhydride with one mole of the free amine of a benzylated amino acid, or one mole of DTPA-dianhydride with two moles of the free amine. The result was the formation of amide bonds where the amino acids attached to the chelants.

All of the reactions were performed under dry nitrogen to prevent hydrolysis of the anhydrides. Nevertheless, EDTA or DTPA would often be evident in the final products. To remove residual EDTA, the derivatives EDTA-TB and EDTA-PB were washed with copious amounts of water. The derivative EDTA-GB, which is slightly soluble in water, was recrystallized from water. The DTPA derivatives were separated by dissolving them in 1M ammonium acetate, and running the solutions down a column filled with G-10 Size Exclusion Sephadex Gel (MW cutoff <700). The ligands, which have a molecular weight greater than 700, were retrieved from the first few fractions, which were combined and lyophilized. The ligands were dissolved in water, and retrieved as solids upon acidification, and then dried under high vacuum. This was to facilitate the weighing of the ligands for the T_1 experiments.

All of the ligands were soluble in water when base was added to pH$\approx$6.5-7. However, the solubility of the TB and PB derivatized chelants proved to be a problem when GdCl$_3$ was added. To circumvent this problem, two approaches were

Table 6.1 Relaxivities of Gd-EDTA and Gd-DTPA Derivative Complexes.[a]

Complex	$R_1 (mM^{-1}s^{-1})$	95% Confidence Interval
Gd-EDTA-GB	7.5	6.1 to 8.9
Gd-EDTA-TB[b,c]	5.2	4.6 to 5.7
Gd-EDTA-PB[c]	13.3	11.0 to 15.6
Gd-EDTA[c]	5.7	4.7 to 6.6
Gd-DTPA-GB	3.9	3.3 to 4.5
Gd-DTPA-TB[b,c]	5.8	4.4 to 7.1
Gd-DTPA-PB[c]	16.3	14.4 to 18.2
Gd-DTPA	4.2	4.9 to 6.7

[a] In 100% D_2O unless otherwise stated; 27°C; pH 7.2; 300 MHz. [b] Lower concentrations. [c] 50/50 D_2O/MeOD.

taken. For the PB derivatives, the standards were dissoved in a 50/50 mixture of D_2O/MeOD. For the TB derivatives, the concentrations of the standards were decreased from 2, 4, 6, 8, and 10 mM to 0.4, 0.8, 1.2, 1.6, and 2.0 mM, and were also dissoved in a 50/50 mixture of D_2O/MeOD. In order to observe the affect such a mixture would have on the values of R_1, the relaxivities for Gd-EDTA and Gd-DTPA were redetermined in solutions of 50/50 D_2O/MeOD.

The data in **Table 6.1** represent preliminary R_1 values that give an indication of the relaxivity properties of the Gd(III) complexes. Because of the assumptions made (see **Chapter 5**), it is best to assess the results qualitatively.

When MeOD was used with D_2O, the R_1 values of the Gd-EDTA and Gd-DTPA complexes decreased slightly. This might be expected because of the lesser viscosity, η, of the MeOD (0.547 x 10^{-2} g cm^{-1} s^{-1} for MeOH cf. 1.002 x 10^{-2}

g cm^{-1} s^{-1} for H$_2$O, both at 20°C).[88] As shown in equation 1-5, the value of η is directly proportional to τ_R, which is directly proportional to R$_1$ (equations 5-1 and 5-2). Surprisingly, the R$_1$ values of the PB derivatives are quite high. This may be caused by an increase in τ_R because of the increased size of the Gd complex, similar to the effect experienced by Lauffer and Aime, as mentioned above.

Conversely, the R$_1$ values for Gd-EDTA-GB, Gd-DTPA-GB, Gd-EDTA-TB, and Gd-DTPA-TB change much less, within the 95% confidence intervals, compared to the original values of 6.2 mM^{-1}s^{-1} for Gd-EDTA and 4.1mM^{-1}s^{-1} for Gd-DTPA. The τ_R value did not seem to change the R$_1$ value even for the TB complexes, which are certainly as large as the PB complexes. One reason for the apparent quenching effect may be an increase in the τ_M value so that it is similar to the T$_{1M}$ value ($\sim 10^{-6}$). The increase in τ_M leads to a decrease in 1/T$_1$ according to equation 1-2. This was observed for the Gd-DTPA-BMA complex (see **Chapter 5**), where τ_M was found to be 0.81 µs. The lengthening of τ_M may occur because there is less residual electron density on the metal when the carboxylate is transformed to an amide group. This may be responsible for a stronger Gd-OH$_2$ bond, which then results in a decrease of the water exchange rate.

The lengthening of the time that a water molecule spends coordinated to the gadolinium ion does not seem to have shortened the relaxivities of Gd-EDTA-PB and Gd-DTPA-PB. The high R$_1$ values for these complexes may in fact be caused by a change in the relative translational diffusion time (τ_D) which leads to change in

the outer sphere solvent relaxation contribution to R_1. This process is not very well understood compared to inner sphere processes,[20] but studies suggest that a decrease in viscosity, as in the 50/50 D_2O/MeOD case, leads to a decrease in τ_D, and a subsequent increase in $[1/T_1]_{outer\ sphere}$ relaxation. It is interesting that the Gd-EDTA and Gd-DTPA complexes were not affected in this way. The Gd-EDTA-TB and Gd-DTPA-TB complexes may not have had as much of an effect on the outer sphere relaxation because of the lower concentrations used in the experiment.

It is clear that more information is needed to completely evaluate these complexes as potential contrast agents for MRI. The poor solubility of the TB and PB complexes may prove to be a problem unless biodistribution studies show that they are very site specific. If that is the case, a lower concentration of the compound would need to be administered.

6.2 Experiments

<u>Anhydrides</u>

EDTA-Dianhydride (EDTADA)

This synthesis was performed according to methods previously described.[89] EDTA (18.5 g , 0.06 mole) was suspended in 32 mL of dry pyridine under a nitrogen atmosphere. The temperature was adjusted to 60-65°C. Acetic anhydride (24 mL) was added with a syringe. The mixture was stirred for 24 h at 65°C. The mixture was allowed to cool, and was then vacuum filtered under nitrogen and washed with acetic anhydride (3 x 50 mL) and diethyl ether (3 x 50 mL). The colourless solid was left under high vacuum for 16 h and stored in a dessicator. Yield: 13.4 g (85%).

Mp: 181-183°C (lit. 176-182°C)[89]. ^{1}H NMR (200 MHz, DMSO-d$_6$), δ: 2.67 (s, 4H, N-CH$_2$-CH$_2$-N), 3.71 (s, 8H, N-CH$_2$-C=O-); ^{13}C NMR (50 MHz, DMSO-d$_6$), δ: 50.72, (N-CH$_2$-CH$_2$-N), 51.79 (N-CH$_2$-C=O-), 165.26 (N-CH$_2$-C=O-); EIMS:m/z (%intensity), 256(7) [M$^+$], 128 (100) [symmetrical cleavage]; IR (KBr pellet): υ$_{Max}$, 1770 cm [anhydride].

EDTA-Monoanhydride (EDTAMA)

The synthesis was performed according to a method already described.[90] EDTADA (5 g, 0.019 mole) was suspended in dry DMF (30 mL) under a dry nitrogen atmosphere and heated to 70-72°C, upon which dissolution was apparent. Distilled water (350 μL, 0.019 mole) was added by means of a microsyringe. The solution was stirred at 72°C for 3 h over which time EDTAMA precipitated as a colourless solid. The reaction mixture was cooled to room temperature. The precipitate was filtered under vacuum and a steady stream of dry nitrogen and washed with diethyl ether (3 x 25 mL). The white solid was collected and dried under high vacuum. Yield: 3.85 g (72 %). Mp 188-190°C (lit. 189-191°C)[90]. ^{1}H NMR (200 MHz, DMSO-d$_6$), δ: 2.60 (2H, t, J= 6 Hz, N-CH$_2$-CH$_2$-N on carboxyl side), 2.81 (2H, t, J=6 Hz, N-CH$_2$-CH$_2$-N on anhydride side), 3.43 (4H, s, CH$_2$ next to COOH), 3.73 (4H, s, CH$_2$ next to anhydride), ^{13}C NMR (50 MHz, DMSO-d$_6$), δ: 50.56 (C- 4), 52.05 (C-5), 52.50 (C-2,2'), 54.64 (C-7,7'), 165.67 (anhydride carbonyls), 172.35 (carboxyl carbonyls). EIMS: m/z (% intensity), 274 (5) [M$^+$], 256(15) [M$^+$-H$_2$O], 216(20) [M$^+$-CH$_2$COO], 146(40), 128(100). IR (KBr pellet):υ$_{Max}$, 1640 [carboxyls], 1770 cm^{-1} [anhydride].

DTPA-Dianhydride (DTPADA)

The synthesis was performed according to a published method.[87] DTPA (3.1 g, 0.0078 mole) was suspended in a mixture of acetic anhydride (7 mL) and dry pyridine (6 mL) under dry nitrogen and warmed to 65°C. The suspension was stirred vigorously for 48 h. The reaction mixture was cooled to room temperature, filtered by vacuum under a dry stream of nitrogen and washed with acetic anhydride (3 x 20 mL) and diethyl ether (3 x 20 mL). The cream coloured solid was left under high vacuum for 24 h and stored in a dessicator. Yield: 2.5 g (90 %). Mp, 169-171°C (lit. 171-173°C)[87], ^{1}H NMR (200 MHz, DMSO-d_6), δ: 2.59 (4H, t, J=7.5 Hz, H-4), 2.74 (4H, t, J=7.5 Hz, H-5), 3.30 (2H, s, H-2), 3.71 (8H, s, CH_2 by anhydride), ^{13}C NMR (50 MHz, DMSO-d_6), δ: 50.67 (C-4), 51.73 (C-5), 52.53 (C-2), 54.47 (CH_2 by anhydride), 165.67 (anhydride carbonyls), 171.89 (carboxyl carbonyl). IR (KBr pellet):υ_{Max}, 1760 [anhydrides], 1640 cm^{-1}[carboxyl].

Amino Acids: Free Amines

The amino acids were obtained as their p-toluenesulfonate salts. In order to convert them to the free amine, they were dissolved in water with a half molar amount of Na_2CO_3 (glycine benzyl ester and phenylalanine benzyl ester) or an equimolar amount of $NaHCO_3$ (tyrosine benzyl ester). The aqueous layer was then washed three times with an equivalent volume CH_2Cl_2. The CH_2Cl_2 washings were combined and evapourated to dryness at reduced pressure to give the free amine as pale yellow oils. The yields were between 80-95%. The characterization of each free amine is as follows:

Glycine Benzyl Ester (GB)

TLC (1 CH$_3$OH: 4 CHCl$_3$), R$_f$=0.47. ^{1}H NMR (200 MHz, DMSO-d$_6$): δ: 1.44 (2H, s, -NH$_2$), 3.44 (2H, s, H-10), 5.15 (2H, s, H-12), 7.34 (5H, s, aromatic). EIMS: m/z (%intensity), 166 (30) [M$^+$], 91 (100) [M$^+$-phenyl].

Phenylalanine Benzyl Ester (PB)

TLC (1 CH$_3$OH: 4 CHCl$_3$), R$_f$ = 0.61. ^{1}H NMR (200 MHz, DMSO-d$_6$): δ: 1.81 (2H, s, -NH$_2$), 2.83 (2H, m, H-17), 3.62 (1H, t, J$_{10,17}$= 6.8 Hz, H-10), 5.04, (2H, s, H-12), 7.24 (10H, m, aromatic).

Tyrosine Benzyl Ester (TB)

TLC (1 CH$_3$OH: 4 CHCl$_3$), R$_f$ = 0.42. ^{1}H NMR (200 MHz, DMSO-d$_6$): δ: 1.95 (2H, s, -NH$_2$), 2.71 (2H, m, H-17), 3.53 (1H, t, J$_{10,17}$=6.6 Hz, H-10), 5.03 (2H, s, H-12), 6.61 (2H, d, J$_{19,20}$=8.4 Hz, H-19), 6.90 (2H, d, J$_{20,19}$=8.4 Hz, H-20), 7.28 (5H, m, aromatic), 9.19 (1H, s, -OH).

EDTA and DTPA Derivatives

The free amines were reacted with the anhydrides in a ratio of 1:1 for the EDTAMA, and a ratio of 2:1 for the DTPADA. The reactants (0.001 mole each) were dissolved in dry DMF (10 mL) in a dry nitrogen environment. The solutions were stirred for 2 h at room temperature. The reaction was followed with TLC (1 CH$_3$OH: 4 CHCl$_3$, visualized with a UV lamp), where the product would stay at the base line, but unreacted amine would move up the plate. The reaction was judged complete when there was no residual amine evident. Upon completion, the solvent was removed at reduced pressure at 60°C. The EDTA ligands were removed from the reaction flask with a minimum amount of MeOH. The MeOH solution was

diluted with water and acidified with 10% HCl to pH 6, whereupon a colourless precipitate formed. The precipitate was collected by filtration and washed with water to remove excess EDTA. To the reaction flasks of the DTPA ligands was added the minimum amount of 0.5 M NH_4^+-acetate buffer (pH 7). Each solution was chromatographed on a Sephadex G-10 size exclusion column (15 cm x 1 cm) and collected in fractions of 2 mL (60 drops). The first four fractions were collected and lyophilized. Both the DTPA and EDTA ligands were checked for purity with MS electrospray (MSES). The -ve mode of ESMS, with 0.1% NH_4OH added to the sample, detected residual EDTA or DTPA, and the +ve mode, with 0.1%HCl added to the sample, detected residual amine. The purification procedure was repeated until the starting materials could not be detected by ESMS. The EDTA ligands sometimes showed disubstituted EDTA with an intensity of <5% in -ve ESMS, but it could not be seen in the ^1H NMR spectrum. All of the ligands were soluble in MeOH and EtOH. They were soluble in water when a base was added to bring the pH to ~ 7. Each ligand had the following characteristics:

EDTA-GB

This ligand was obtained as a colourless solid that would absorb water and turn to a pale yellow oil if left open to the air. ^1H NMR (500 MHz, D_2O), δ: 2.81 (2H, t (br.), H-4), 3.10 (2H, s, H-7'), 3.14 (2H, s, H-5), 3.27 (2H, s, H-7), 3.61 (4H, s, H-2,2'), 3.92 (2H, s, H-10), 5.04 (2H, s, H-12), 7.28 (5H, s, aromatic). ^{13}C NMR (125 MHz, D_2O), δ, ppm, 41.44 (C-10), 49.71 (C-5), 51.58 (C-4), 57.85 (C-7'), 58.01 (C-2,2'), 58.31 (C-7), 67.69 (C-12), 128.47 (aromatic C-14 or C-15), 128.80 (C-16), 128.91 (C-14 or C-15), 135.27 (C-13), 170.40 (C-1,1'), 171.26 (C-11), 174.46 (C-8),

178.22 (C-8'). ESMS (-ve mode + 1 drop 0.1% NH₄OH): m/z (% intensity), 585.4

(2) [disubstituted EDTA⁻¹], 438.4(100) [M⁻], 219 (35) [M²⁻].

EDTA-PB

This ligand would remain as a colourless powder indefinitely, even when exposed to air. ¹H NMR (500 MHz, D₂O), δ: 2.69 (4H, s (br), H-4), 2.99 (4H, m, H-5 and H-7), 3.10 (1H, s, H-10), 3.17 (2H, s, H-7'), 3.53 (4H, s, H-2,2'), 4.57 (2H, m, H-17), 5.06 (2H, m, H-12), 7.08 (m, aromatic), 7.18 (m, aromatic), 7.30 (m, aromatic). ¹³C NMR (125 MHz, D₂O), δ: 36.25 (C-10), 49.83 (H-4), 52.89 (C-5), 54.29 (C-17), 56.76 (C-2,2'), 57.96 (C-7 or c-7'), 58.27 (C-7 or C-7'), 67.82 (C-12), 128.61 (aromatic), 128.84 (aromatic), 128.88 (aromatic), 128.91 (aromatic), 129.29 (aromatic), 135.22 (aromatic C-13 or C-18), 136.58 (aromatic C-13 or C-18), 171.07 (C-1,1'), 172.70 (C-11), 173.77 (C-8'), 178.46 (C-8). ESMS (-ve mode + 1 drop 0.1% NH₄OH): m/z (% intensity), 765.4 (3) [disubstituted-EDTA⁻¹], 528.3 (100) [M], 263.9(15) [M²⁻].

EDTA-TB

This ligand was obtained as a yellow, sticky oil. ¹H NMR (500 MHz, D₂O), δ: 2.61 (2H, s(br.), H-4), 2.69 (2H, m, H-17), 2.92 (4H, m, H-5 and H-7), 3.08 (2H, s, H-7'), 3.50 (4H, s, H-2, 2'), 4.30 (1H, t(br), H-10), 4.77 (1H, d, J₁₂ₐ,₁₂ᵦ = 12.1 Hz, H-12a), 4.82 (1H, d, J₁₂ᵦ,₁₂ₐ = 12.1 Hz, H-12b), 6.48 (2H, d, J ₁₉,₂₀=6.9 Hz, aromatic H-19 or H-20), 6.64 (2H, d, J₁₉,₂₀=6.9 Hz, aromatic H-19 or H-20), 6.89 (m, aromatic), 6.99 (m, aromatic), ¹³C NMR (125 MHz, D₂O), δ: 35.54 (C-17), 49.38 (C-5), 52.80 (C-4), 54.12 (C-10), 56.62 (C-2,2'), 57.50 (C-7 or C-7'), 115.46 (C-19 or C-20), 127.77 (aromatic), 128.31 (aromatic), 128.54 (aromatic), 128.62 (aromatic), 130.43 (C-21),

134.98 (C-13), 170.22 (C-1,1'), 172.43 (C-11 or C-8'), 172.73 (C-11 or C-8'), 177.39 (C-8), ESMS (-ve mode + 1 drop 0.1% NH_4OH): m/z (% intensity), 797.4 (3) [disubstituted-EDTA^{-1}], 544.3 (100) [M$^-$], 272.0(10) [M^{2-}].

DTPA-GB

This ligand remained a pale yellow, flaky solid when not exposed to air. When exposed for a few minutes, it became a sticky yellow oil. ^{1}H NMR (500 MHz, D_2O), δ: 2.84 (4H, s, H-5), 3.09 (8H, s, H-7' and H-4), 3.28 (4H, s, H-7), 3.53 (2H, s, H-2), 3.95 (4H, s, H-10), 5.08 (4H, s, H-12), 7.31 (10H, s, aromatic). ^{13}C NMR (125 MHz, D_2O), δ: 41.34 (C-10), 49.95 (C-4), 52.98 (C-5), 54.81 (C-2), 58.46 (C-7 or C-7'), 58.55 (C-7 or C-7'), 67.66 (C-12), 128.39 (aromatic C-14 or C-15), 128.78 (aromatic C-16), 128.92 (aromatic C-14 or C-15), 135.35 (C-13), 170.32 (C-1), 171.14 (C-11), 174.60 (C-8), 178.64 (C-8'). ESMS (-ve mode + 1 drop 0.1% NH_4OH): m/z (% intensity), 686.4 (100) [M$^-$], 342.7 (20) [M^{2-}].

DTPA-PB

This ligand was obtained as a sticky yellow oil. ^{1}H NMR (500 MHz, D_2O), δ: 2.74 (4H, m, H-17), 2.95 (4H, t(hidden), H-4), 3.17 (2H, s, H-2), 3.28 (4H, t, $J_{5,4}$= 6.5 Hz, H-5), 3.71 (4H, s, H-7'), 4.45 (2H, t(br), H-10), 4.65 (2H, d(hidden), H-12a), 4.73 (2H, d, $J_{12b,12a}$=12.1 Hz, H-12b), 6.74 (m, aromatic), 6.85 (m, aromatic), 6.91 (m, aromatic). ^{13}C NMR (125 MHz, D_2O), δ: 36.77 (C-17), 49.28 (C-4), 52.99 (C-5), 53.79 (C-10), 56.39 (C-2), 57.14 (C-7'), 57.60 (C-7), 67.22 (C-12), 127.05 (aromatic), 128.25 (aromatic), 128.31 (aromatic), 128.49 (aromatic), 128.65 (aromatic), 129.16 (aromatic), 135.23 (aromatic), 136.25 (aromatic), 170.64 (C-8'), 172.20 (C-11), 173.05 (C-8), 178.31 (C-1). ESMS (-ve mode + 1 drop 0.1%

NH_4OH): m/z (% intensity), 866.4 (30) [M'], 432.9 (100) [M^{2-}].

DTPA-TB

This ligand was obtained as a sticky yellow oil. ^1H NMR (500 MHz, D_2O), δ: 2.69 (4H, s, H-4), 2.75 (2H, m, H-17a or H-17b), 2.81 (2H, m, H-17a or H-17b), 2.96 (4H, s, H-7), 3.14 (4H, s, H-7'), 3.42 (2H, s, H-2), 4.44 (2H, t (br), J=7.2 Hz, H-10), 4.78 (2H, d, $J_{12a,12b}$=12.2 Hz, H-12a), 4.87 (2H, d, $J_{12b,12a}$=12.2 Hz, H-12b), 6.59 (4H, d, $J_{20,19}$= 7.9 Hz, aromatic H-20 or H-19), 6.75 (4H, d, $J_{20,19}$= 7.9 Hz, aromatic H-20 or H-19), 7.00 (m, aromatic), 7.10 (m, aromatic), ^{13}C NMR (125 MHz, D_2O), δ: 35.69 (C-17), 49.63 (C-5), 52.46 (C-4), 54.07 (C-10), 57.87 (C-7), 58.51 (C-7'), 67.50 (C-12), 115.57 (aromatic C-20), 127.85 (aromatic), 128.40 (aromatic), 128.59 (aromatic), 128.69 (aromatic), 130.51 (aromatic C-13), 154.73 (aromatic C-18), 170.15 (C-1), 172.45 (C-11), 173.46 (C-8'), 178.45 (C-8). ESMS (-ve mode + 1 drop 0.1% NH_4OH): m/z (% intensity), 898.6 (30) [M'], 449.1 (100) [M^{2-}].

The details of the T_1 relaxation experiments are given in **Chapter 2**.

Chapter 7

Azapropazone Derivatives of EDTA and DTPA as Potential Contrast Agents

The joining of azapropazone, an anti-inflammatory drug, to a paramagnetic metal chelate presents the possibility that the agent may be attracted by COX-1 and/or COX-2 receptors (see section **1.2**), and therefore localize in inflammation sites. Usually, macromolecules are used to achieve such specificity. For example, biomolecules such as radiolabelled polyclonal human immunoglobulin G and white blood cells (WBCs)have been studied as inflammation site radioimaging agents with moderate success.[91, 92] Chemotactic peptides (MW$\approx$ 1500) labelled with ^{111}In or ^{99m}Tc, which bind to high-affinity receptors on WBC membranes, have also been studied to image inflammation, with slightly greater success. The disadvantage of the macromolecular complexes is that diagnostically useful images were not obtained until at least 4h and often as long as 24 h after injection.

This chapter presents the synthesis, characterization, and proton relaxivity enhancement effects of EDTA-AZAP and DTPA-AZAP complex with Gd (III). The schematic structures of the ligands with the atom numbering are presented in **Figure 7.1**. It was hoped that paramagnetic complexes with these ligands would produce inflammation imaging agents superior to those mentioned above because they are smaller hydrophilic molecules that should show rapid blood clearance, which would allow imaging at earlier times. This postulate was tested for DTPA-AZAP with ^{111}In in biodistribution and *in vivo*
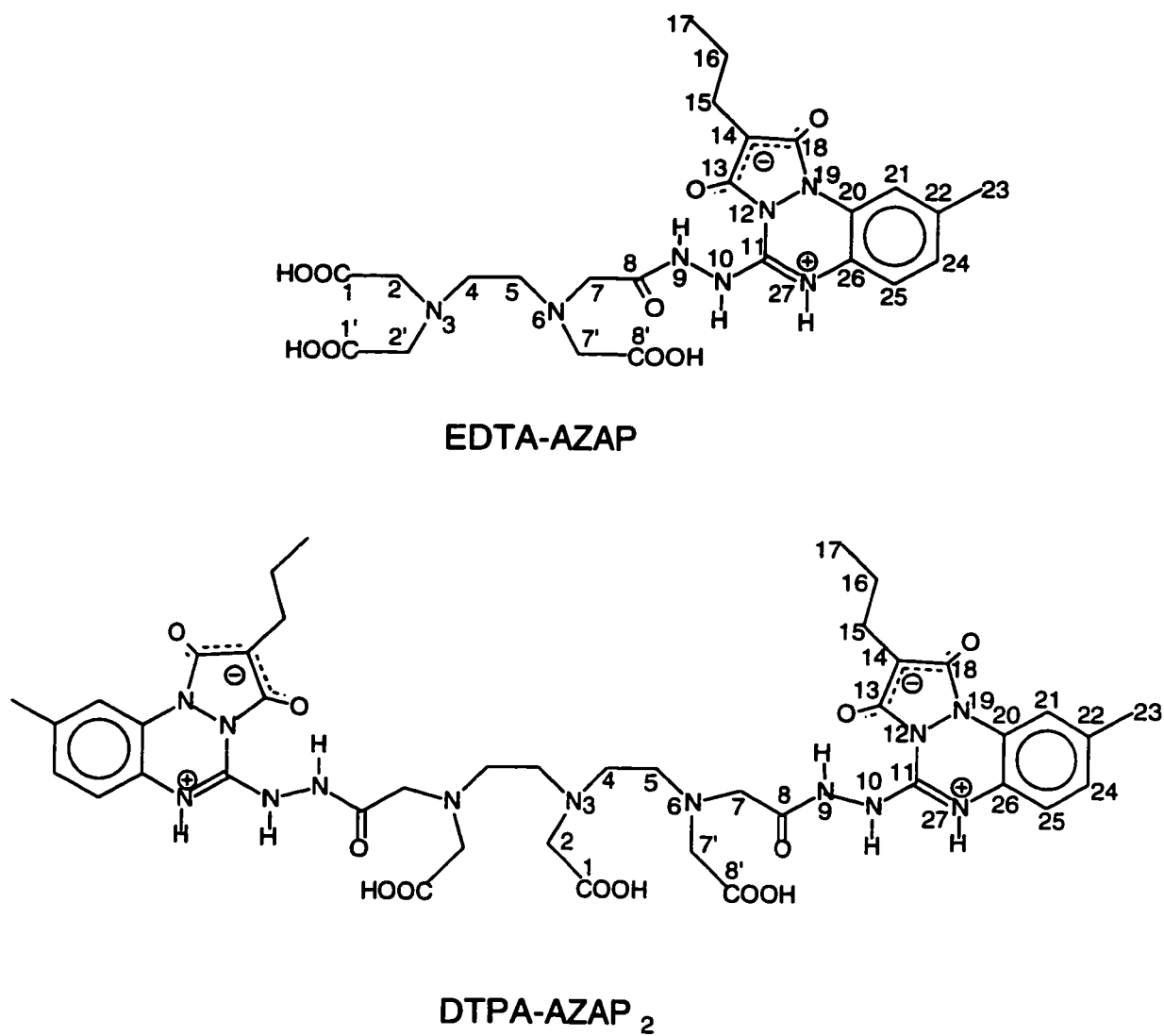
Figure 7.1 The schematic structures of EDTA-AZAP and DTPA-AZAP with atom numbering.

SPECT imaging. The results are presented in **Chapter 8.**

7.1 Results and Discussion

The ligands were made by reacting 1 mole of AZAP-NH-NH$_2$ (**V, Chapter 4**) with 1 mole of EDTAMA, and 2 moles of **V** with 1 mole of DTPADA in a dry nitrogen atmosphere. The ligands were purified by dissolving them in 1M ammonium acetate buffer and chromatographing them on a column packed with G10 size exclusion Sephadex Gel. The first few fractions were combined and lyophilized.

Both of the Gd-EDTA-AZAP and Gd-DTPA-AZAP complexes were soluble in water at pH 7.2-7.5, which perhaps makes them more attractive as potential imaging agents than the amino acid derivatives (**Chapter 6**).

The proton relaxitivity results are shown in **Table 7.1.** The relaxivity of Gd-EDTA-AZAP is lower than that of Gd-EDTA, while the relaxivity of Gd-DTPA-AZAP is similar to its Gd-DTPA counterpart. There were no apparent effects from a lengthening of τ_R, which could increase R_1 (see **Chapter 6**). There may have been an increase in the time that a water molecule remained coordinated to the metal, or τ_M. This effect could be the cause of the shortening of R_1 for Gd-EDTA-AZAP, although the reason why the same effect was not seen with the Gd-DTPA-AZAP complex is unclear.

Table 7.1 Relaxivities of Gd-EDTA-AZAP and Gd-DTPA-AZAP Complexes in 100% D$_2$O.[a]

Complex	Relaxivity (mM^{-1}s^{-1})	95% Confidence Interval
Gd-EDTA-AZAP	4.1	3.6 to 4.6
Gd-DTPA-AZAP	3.9	3.3 to 4.5

[a] 300 MHz; pH 7.2-7.5; 27°C.

The lower R_1 value of the Gd-EDTA-AZAP may indicate that there is only one coordinated water in this complex, as its relaxivity is in the order of magnitude that is normally found for DTPA lanthanide metal complexes, which normally have one coordinated water.

In conclusion, there were no enhanced relaxivities with the complexes presented in this chapter. However, the agents may be useful if they prove to be site specific.

7.2 Experiments

All reactions were performed under dry nitrogen and in reaction vessels covered with foil to protect the azapropazone products from light. The AZAP-NH-NH$_2$ (V) was synthesized according to the reaction described in **Chapter 4**. The EDTA monoanhydride (EDTAMA) and DTPA dianhydride (DTPADA) were synthesized according to the reactions described in **Chapter 6**.

EDTA-AZAP

Compound V (95 mg, 0.33 mmol) was dissolved in dry DMF (15 mL). EDTAMA (104 mg, 0.33 mmol) was added to the solution. The reaction was left stirring for 6 h at room temperature, after which time the solvent was removed at reduced pressure (1 mm Hg, 60°C). The yellow residue was dissolved in 0.1 N NaOH/MeOH (0.5 mL). A colourless precipitate (EDTA·2Na, 12 mg) appeared after 5 h, and was collected by filtration. After 12 h, the desired product appeared as a flaky yellow-white precipitate. It was collected by filtration under reduced pressure and washed with acetone. The solid was dissolved in water (3 mL) and acidified with 0.1 N HCl (0.25 mL). A colourless solid precipitated, which was collected by filtration, dried on the high vacuum overnight, and

stored under nitrogen. The colourless solid became a yellow gel upon exposure to air. Yield of colourless solid: 70 mg (34 %). ^{1}H NMR (500 MHz, D$_2$O), δ: 0.76 (3H, t, $J_{17,16}$=7.1 Hz, H-17), 1.34 (2H, m, H-16), 2.01 (2H, t, $J_{15,16}$= 7.1 Hz, H-15), 2.10 (3H, s, H-23), 3.02 (2H, t(br), H-5), 3.28 (2H, s, H-7), 3.34 (2H, t(br), H-4), 3.53 (2H, s, H-7'), 3.78 (4H, s, H-2,2'), 6.73 (1H, d, $J_{24,25}$= 7.9 Hz, H-24) 6.98 (1H, d, $J_{25,24}$=7.9 Hz, H-25), 7.77 (1H, s, H-21). ^{13}C NMR (125 MHz, D$_2$O), δ: 20.52 (C-17), 21.77 (C-23), 21.97 (C-16), 22.87 (C-15), 49.86 (C-5), 53.26 (C-4), 56.66 (C-7'), 57.09 (C-2,2'), 58.24 (C-7), 87.39 (C-14), 114.28 (C-21), 118.28 (C-24), 124.43 (C-25), 136.09 (C-22), 147.08 (C-11), 161.41 (C-20 or C-26), 170.57 (C-1,1'), 173.35 (C-8'), 178.20 (C-8). ESMS (-ve mode + 1 drop 0.1% NH$_4$OH): m/z (% intensity), 560 (100)[M$^-$], 280 (10)[M^{2-}].

DTPA-AZAP

Compound V (270 mg, 0.94 mmol) was dissolved in dry DMF (20 mL). DTPADA (168 mg, 0.47 mmol) was added to the solution. The reaction was left stirring for 6 h at room temperature, after which time the solvent was removed at reduced pressure (1 mm Hg, 60°C). The yellow residue was dissolved in 1 M ammonium acetate buffer (2.5 mL, pH=7). The solution was chromatographed on a Sephadex G-10 size exclusion column (15 cm x 1 cm) and collected in fractions of 2 mL (60 drops). The first four fractions were collected and lyophilized to give a colourless flaky solid. The solid was dissolved in water (4 mL) and acidified with 0.1 N HCl to pH = 3. The free acid of the product was obtained as a colourless solid. The product was filtered, dried on the high vacuum overnight, and stored under dry nitrogen. Yield: 113 mg (26 %). ^{1}H NMR (500 MHz, D$_2$O), δ: 0.77 (6H, t, $J_{17,16}$=7.3 Hz), 1.32 (4H, m, H-16), 1.93 (6H, s, H-23), 1.94 (4H, t(covered), H-15), 3.08 (4H, s, H-5), 3.32 (8H, s, H-4,7), 3.55 (4H, s, H-7'), 3.87 (2H, s, H-2), 6.44 (2H, d, $J_{24,25}$=7.7

Hz, H-24), 6.82 (2H, d, $J_{25,24}$=7.7 Hz, H-25), 7.46 (2H, s, H-21), ^{13}C NMR (125 MHz, D_2O),

δ: 20.66 (C-17), 21.86 (C-16), 21.89 (C-23), 22.24 (C-15), 50.02 (C-5), 53.30 (C-4), 56.78

(C-7'), 57.61 (C-2), 58.48 (C-7), 87.36 (C-14), 114.21 (C-21), 117.64 (C-24), 123.76 (C-25),

136.03 (C-22), 146.21 (C-11), 160.55 (C-20 or C-26), 164.90 (C-20 or C-26), 170.77 (C-1),

173.02 (C-8'), 178.29 (C-8). ESMS (-ve mode + 1 drop 0.1% NH_4OH): m/z (% intensity),

931(40)[M$^-$], 465 (100)[M^{2-}].

Chapter 8

Animal Studies

The evaluation of the ligands studied in this chapter includes an investigation of the biodistribution of their metal complexes, as well as their imaging capability. The imaging capability is evaluated by the selective retention of the agent in a specific organ so that the organ may be observed in greater detail. In this way, an abnormality in that organ may be detected.

MRI facilities were not as readily available as were the SPECT imaging facilities at Resolution Pharmaceuticals, Inc.[33] Therefore, some of the DTPA derivatives were used with ^{111}In as models to examine their clearances from blood, and biodistribution and imaging capabilities. The compounds were injected into rats, which were imaged and then dissected to determine the radioactivity in various organs. Inflammation was induced in one thigh of each rat, thus evaluating the compounds as inflammation imaging agents as well.

8.1 Results and Discussion

The labelling of the ligands was necessary in order to determine complete complexation of the ^{111}In with each ligand. The ligands were complexed with the ^{111}In in a 1:1 ratio and then spotted on a paper chromatogram which was developed with 50/50 NH$_4$-acetate/MeOH. The chromatograms were analyzed with a

phosphorimager. The results can be seen in **Figure 8.1**. The In-DTPA-PB complex (plates 1-5) showed evidence of an unidentified impurity. Therefore, this sample was not used for the biodistribution or imaging studies with the rats. The In-DTPA-GB (plates 6-10) and In-DTPA-AZAP (plates 11-15) gave more promising results. The In-DTPA-AZAP plates appear smudged, which could mean that the sample was impure. However, a subsequent experiment in which a drop of concentrated CH_3COOH was added to the developing solution showed that the sample ran as one spot up the paper. Therefore, the DTPA-AZAP and DTPA-GB ligands were used in the biodistribution and imaging studies.

A total of 24 male Sprague-Dawley rats were used in the biodistribution experiment. The procedure for analyzing the rats included anesthesia. Unfortunately, two of the rats died before they could be analyzed because of an overdose of anesthetic. As a result, only one rat was analyzed at the 21 h for ^{111}In-DTPA-AZAP.

The average tissue distribution of the ^{111}In-DTPA-GB is summarized in **Table 8.1**, and the average tissue distribution of ^{111}In-DTPA-AZAP can be seen in **Table 8.2**. This information is plotted in **Figure 8.2** and **Figure 8.3** for a quick analysis of the results.

The counts of the GI tract and the bladder and urine were not included in the above tables and graphs because they were only recorded in %dose/organ. The results of the counts of these tissues are discussed below.

The graphs and tables shown below suggest that there was
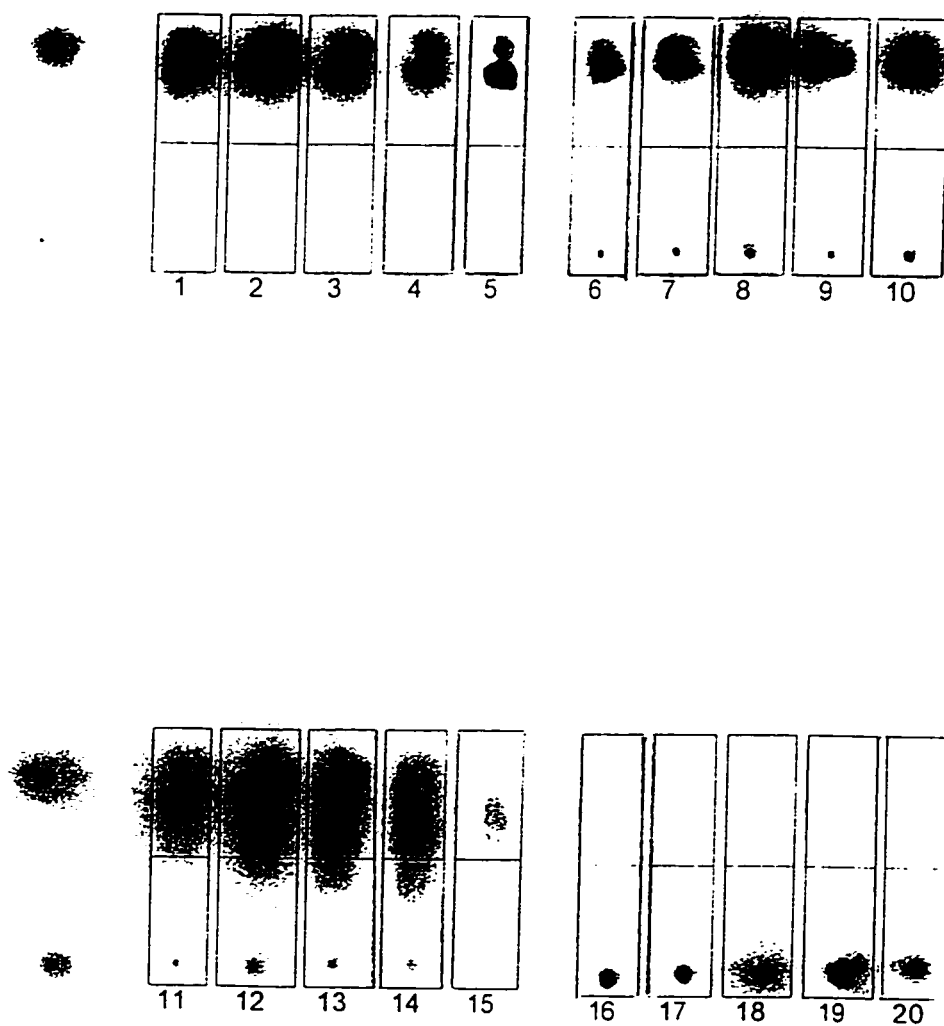
Figure 8.1 The results of labelling studies with the DTPA derivatives and ^{111}In; compound In-DTPA-PB (plates 1-5), compound In-DTPA-GB (plates 6-10), compound In-DTPA-AZAP (plates 11-15), [111]InCl$_3$ (plates 16-20).

significantly more of the ^{111}In-DTPA-GB complex in each organ compared to the ^{111}In-DTPA-AZAP complex. This is because there was more ^{111}In-DTPA-GB retained in the blood stream compared to ^{111}In-DTPA-AZAP at any given time. A percentage of a radioactive compound in the blood stream will result in higher counts in all of the organs. A large percentage of ^{111}In-DTPA-AZAP was excreted into the renal system very soon after injection. This was shown to be the case as more than 20% of the injected dose was present in the bladder and urine within the first hour. Little of this compound remained in the blood, with a maximum % ID of 2.7% at 30 min.

In contrast, ^{111}In-DTPA-GB reached a maximum blood amount of 21% at 30 min, and declined to <1% by 21 h. The excretory route also differed for this compound, which was present in significant amounts in the GI tract (not shown), liver and spleen at all earlier time points.

The target:background ratios for the inflamed thigh vs. the uninflamed thigh for both complexes are shown in **Figure 8.4**. For the ^{111}In-DTPA-AZAP complex, a ratio of 3.8 is achieved at 30 min. The ratio goes down during the next 2 h and then back up to 3.3 at 21 h. According to Pollak et al., this ratio is probably not significant as they found that non-specific agents in the same animal model gave ratios of 2-3.[93] For the[111] In-DTPA-GB complex, a fairly high target:background ratio of about 4 was observed at 3 h and 5.5 at 21 h. The delay of the specificity may be the result of faster clearance of the compound from the control leg in comparison to the inflamed leg. To examine this further, later sacrifice time with more points with more animals would be required.

Table 8.1 The Average Distribution (%dose/g ± SEM)[a] of ^{111}In-DTPA-GB.

Tissue/Time	30 min	1 h	3 h	21 h
Blood	1.049(0.093)	0.863(0.104)	0.726(0.016)	0.006(0.001)
Heart	0.373(0.031)	0.309(0.011)	0.214(0.030)	0.007(0.000)
Lung	0.496(0.036)	0.424(0.024)	0.259(0.033)	0.0080.001)
Liver	0.287(0.020)	0.200(0.024)	0.209(0.011)	0.025(0.002)
Kidney	1.335(0.060)	1.479(0.194)	1.279(0.311)	0.139(0.021)
Spleen	0.221(0.024)	0.206(0.015)	0.182(0.019)	0.025(0.002)
Control Thigh	0.076(0.006)	0.068(0.004)	0.043(0.004)	0.002(0.000)
Inflamed Thigh	0.141(0.012)	0.135(0.003)	0.158(0.012)	0.011(0.000)

[a] Analyses are on 3 rats.

Table 8.2 The Average Distribution (%dose/g ± SEM)[a] of ^{111}In-DTPA-AZAP.

Tissue/Time	30 min	1 h	3 h	21 h[b]
Blood	0.139(0.063)	0.112(0.024)	0.022(0.004)	0.074
Heart	0.125(0.010)	0.063(0.007)	0.043(0.020)	0.065
Lung	0.124(0.017)	0.053(0.012)	0.021(0.004)	0.084
Liver	0.097(0.009)	0.133(0.064)	0.026(0.002)	0.120
Kidney	0.639(0.084)	0.597(0.011)	0.122(0.034)	1.552
Spleen	0.068(0.018)	0.069(0.034)	0.028(0.005)	0.176
Control Thigh	0.020(0.003)	0.022(0.009)	0.005(0.001)	0.023
Inflamed Thigh	0.073(0.013)	0.029(0.002)	0.011(0.001)	0.076

[a] Most analyses are on 3 rats. [b] Analysis is on 1 rat.

The Average Distribution (% Dose/ g) of
In-111-DTPA-GB

Blood	Heart	Lung	Liver
Kidney	Spleen	Control Thigh	Inflamed Thigh
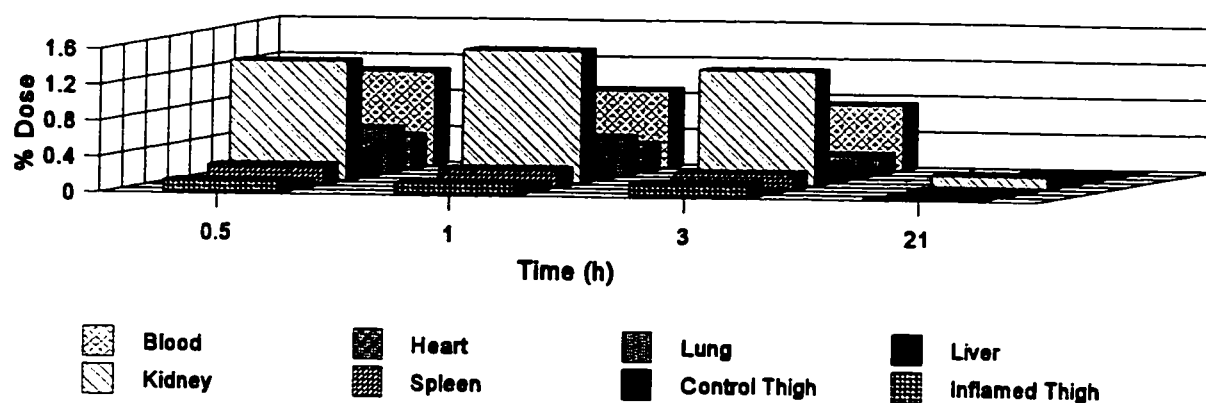
Figure 8.2

The Average Distribution (% Dose/ g) of
In-111-DTPA-AZAP

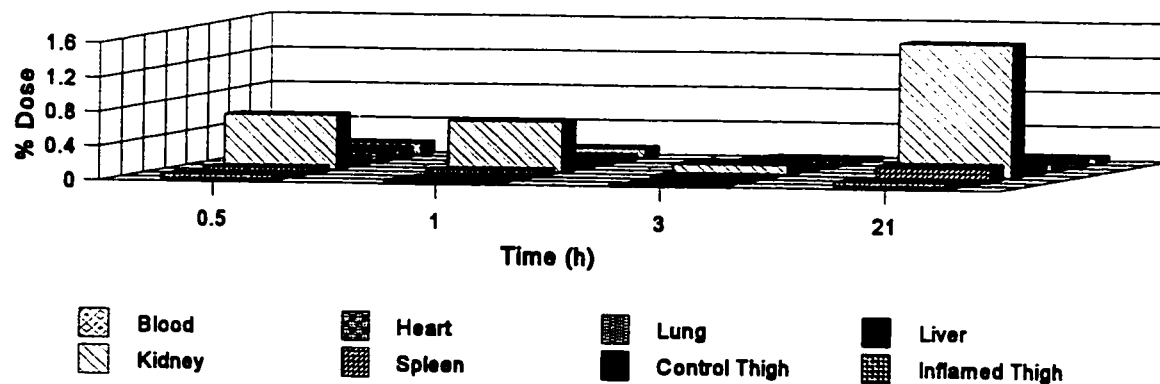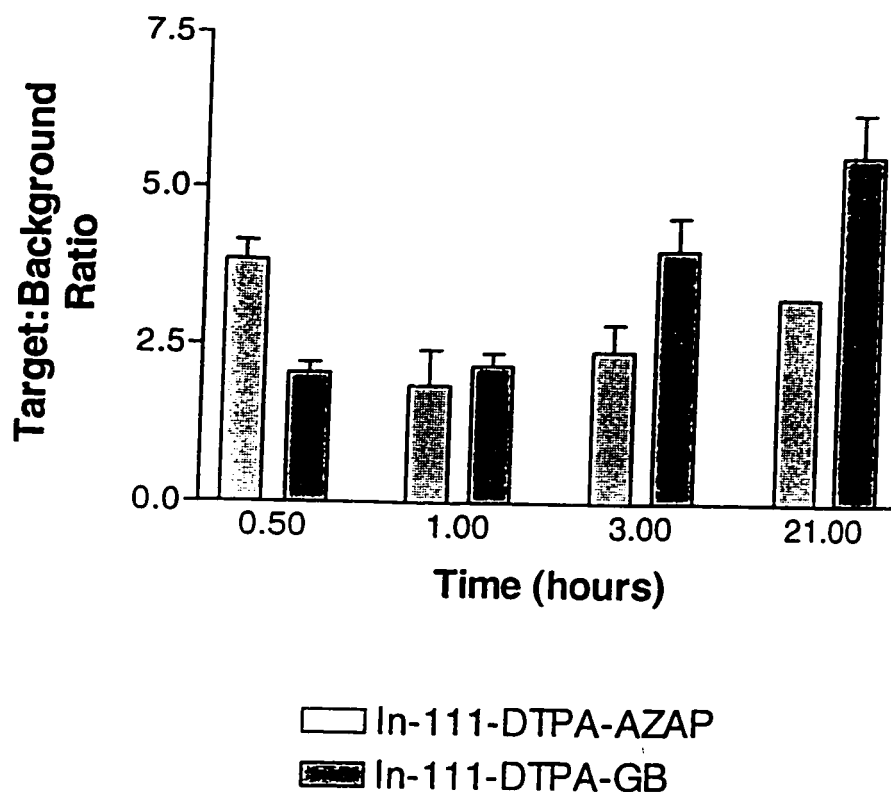|			
Blood	Heart	Lung	Liver
Kidney	Spleen	Control Thigh	Inflamed Thigh

Figure 8.3

Figure 8.4 The Target: Background Ratio of Zymosan-Inflamed Rats.

The SPECT images of the animals gave slightly different results than those indicated by the distribution studies. Images of the same rats were taken at 5 min, 30 min, 60 min, 3 h, and 21 h post injection.

The ^{111}In-DTPA-AZAP complex showed a gathering in the heart and lung area at 5 min (**Figure 8.5a**). At 30 min (**Figure 8.5b**) the complex had gone to the kidneys and bladder. At 21 h (**Figure 8.6b**), the inflamed thigh seemed to be brightening in the image, but it was determined that that particular photograph must be suspect, because both samples show that the bladder had emptied, but that was apparently not the case.
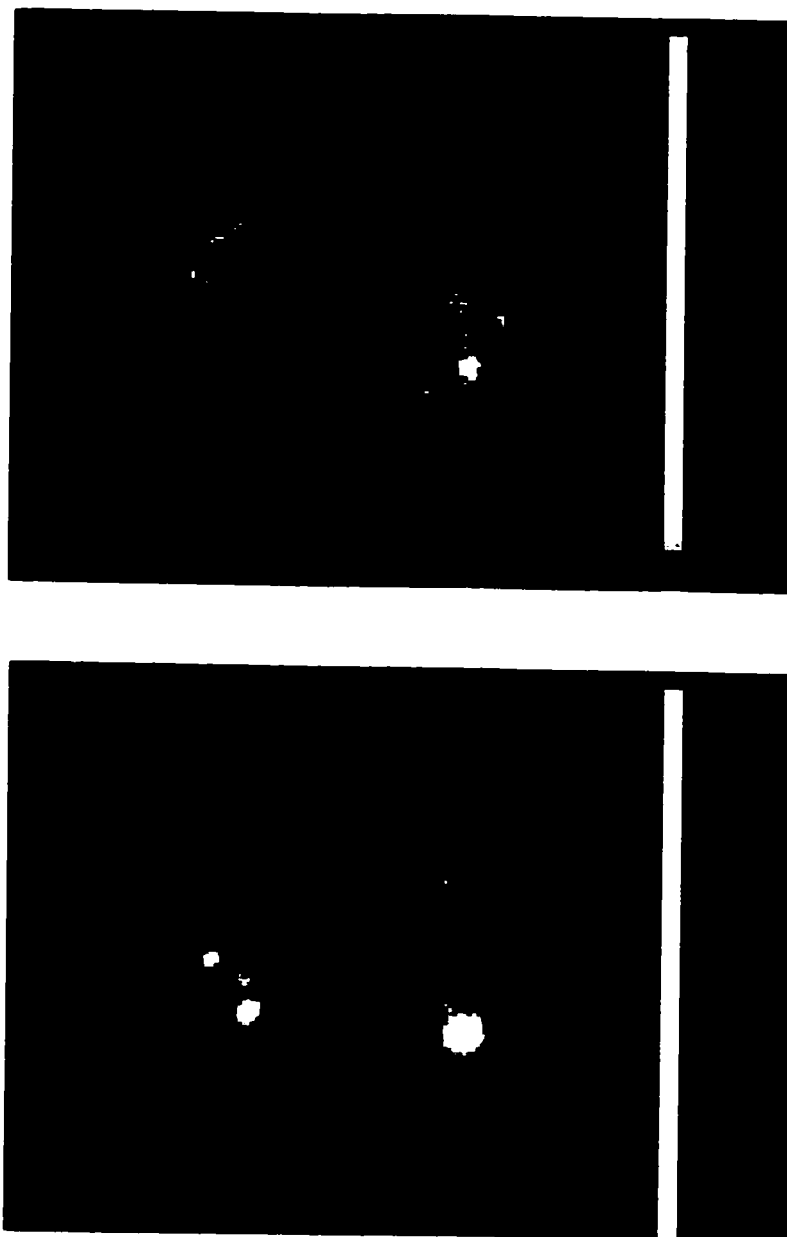
Figure 8.5 The SPECT images of two rats bearing inflammation in the right thigh induced by subcutaneous injection of zymosan. Images are anterior views (i.e. they are on their backs, and the site of inflammation is at the lower left in each image). The rat injected with ^{111}In-DTPA-AZAP is shown on the left, and the rat injected with ^{111}In-DTPA-GB is shown on the right. (a) Top: 5 min post injection. (b) 30 min post injection.
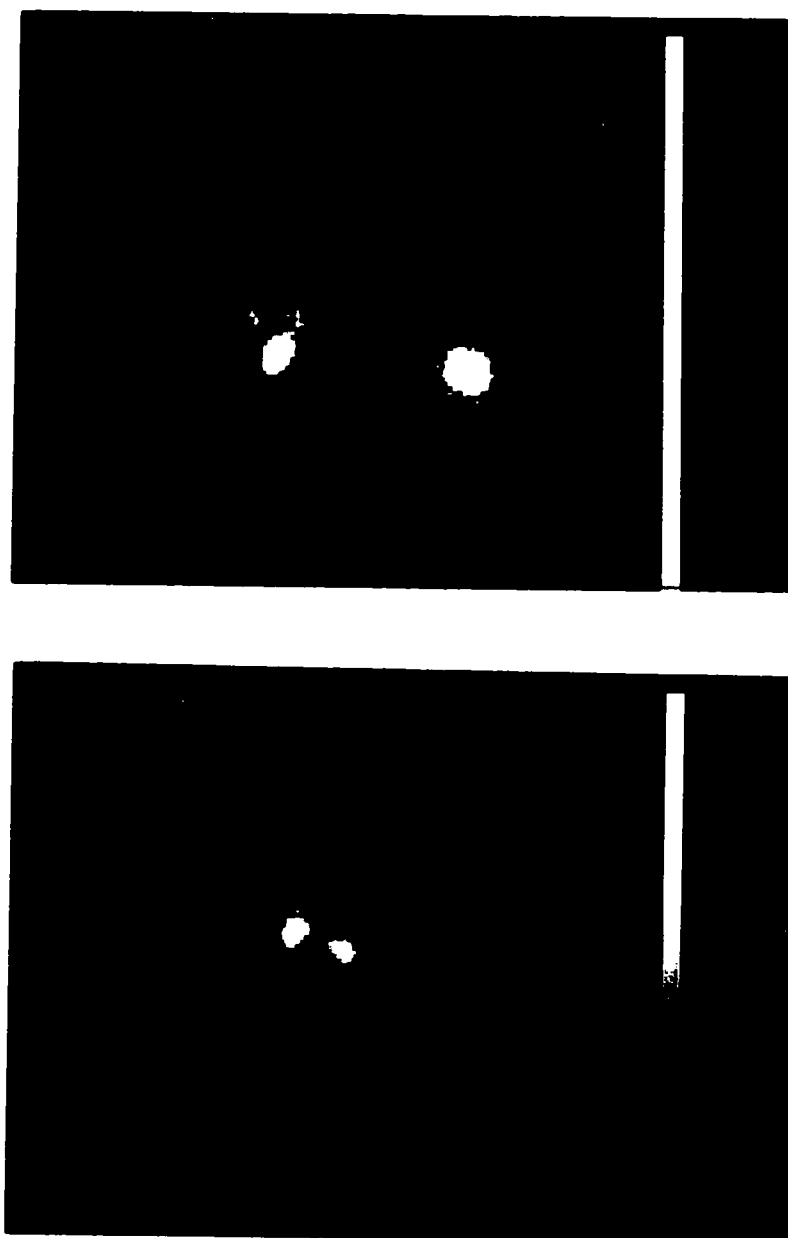
Figure 8.6 The SPECT images of two rats bearing inflammation in the right thigh induced by subcutaneous injection of zymosan. Images are anterior views (i.e. they are on their backs, and the site of inflammation is at the lower left in each image). The rat injected with ^{111}In-DTPA-AZAP is shown on the left, and the rat injected with ^{111}In-DTPA-GB is shown on the right. (a) Top: 3 h post injection. (b) 21 h post injection.

The ^{111}In-DTPA-GB complex shows a brightening of the inflamed thigh at 5 min (**Figure 8.5a**). By 30 min (**Figure 8.5b**) the activity had pooled in the bladder to such an extent that all the other regions appeared dark. This continued at 3 h (**Figure 8.6a**). Again, the bladder appears to be empty at 21 h (**Figure 8.6b**), which cannot be the case.

The interesting results from the SPECT images suggest the possible use of ^{111}In-DTPA-GB as an inflammation imaging agent. The high target:background ratios from the biodistribution studies seem to support this. However, the images imply that most of the complex had gone to the bladder by the 30 min mark, while the biodistribution study suggest that 20% of the complex was still in the blood at that time. Further studies on this complex and related complexes could prove rewarding.

Perhaps more interesting are the results of the ^{111}In-DTPA-AZAP imaging. The retention of the complex in the lungs after 5 min is an effect not seen with the ^{111}In-DTPA-GB complex. Pollak *et al.* also reported a localization of a radiotracer in the heart and lung after 5 min, but made no further comment.[93] Differences between the two complexes studied here may be due to the zwitterionic character of the azapropazone portion of the DTPA-AZAP ligand compared to the less polar DTPA-GB ligand.

It was hoped originally that the ^{111}In-DTPA-AZAP complex would be attracted to the inflammation site because of the COX-1 and/or COX-2 receptors that azapropazone normally inhibits (see **Chapter 1**). However, the inflamed thigh did

not appear in the photographs until 21 h, although the compound cleared out of the blood within 0.5 h. The results warrant further study of this compound and possibly other compounds with zwitterionic moieties.

8.2 Experiments

Labelling Experiments

The labelling experiments were performed at Resolution Pharmaceuticals, Inc. Each of three DTPA derivatives (DTPA-PB, DTPA-TB, and DTPA-AZAP)(0.25 mg in 0.1 mL 50/50 EtOH/H_2O) was mixed with $^{111}InCl_3$ (3mCi) and brought to pH 6.5-7 with 0.1N NaOH. The samples were analyzed for purity by paper chromatography and developed in 10% ammonium acetate in MeOH. The papers were dried with air and analyzed with the Phosphorimager.

Biodistribution Studies

The biodistribution experiments were also performed at Resolution Pharmaceuticals Inc.

Animal Preparation

The procedures for the inflammation model followed Allelix Animal Care Committee Protocol #28-93. Animal preparation began the day prior to experimentation. The animals were weighed and distributed randomly into 8 groups (4 groups per compound, n=3), with each group representing a particular sacrificing time point. The rats were anesthetized with an injection of 30-40 mg/kg Somnotol. Zymosan A (20 mg) was suspended in sterile saline (0.9% NaCl) and was injected (26G 1/2" needle) at a volume of 0.2 mL into the right thigh muscle of each rat. The

animals were then returned to their respective cages and left overnight for the development of inflammation.

Biodistribution

On the day of distribution and imaging, the animals were first anesthetized with Somnotol. The syringes were then filled with 0.2 mL of the radiolabelled compound while the rats were "going under". The amount of activity injected per rat was 5 μCi for biodistribution and 25 μCi for imaging. The test compounds were administered intravenously (i.v.) *via* the tail vein once deep anesthesia was obtained.

The predetermined sacrifice time points were 30 min, 1 h, 3 h, and 21 h, post i.v. injection for each compound. Four of the rats per compound were given 25 μCi for imaging and biodistributionn at the 21 h point. The other animals were given 5 μCi for biodistribution. The animals were maintained under anesthesia on this day with additional Somnotol whenever needed. Prior to euthanasia, a blood sample (1-3 mL) was obtained *via* cardiac puncture (22G 1" needle). The animals were sacrificed by cervical dislocation. Various tissue samples were dissected out, placed in preweighed tubes, weighed and counted in the gamma-counter. The gamma counter was able to back-calculate the counts to the activity at a specific reference time (*i.e.* the time of labelling). The tissues dissected were the heart, bladder and urine (collected with a 1 mL syringe and 26G 3/4" needle), lung, liver, kidney, spleen, brain (for 3 animals), GI tract, control thigh muscle, inflamed thigh muscle with exudate (fluid around inflammation), and tail. Only a sample of the pre-weighed liver was placed into a tube and counted. Note that the GI tract and tail

were placed into plastic bags and counted for radioactivity in the capintec as this was a more efficient method.

SPECT Imaging

A rat with ^{111}In-DTPA-GB and one with ^{111}In-DTPA-AZAP were each imaged at 5 min, 30 min, 1 h, 3 h, and 21 h post injection.

Data Analysis

Biodistribution values were expressed as percentage of the injected dose per gram or organ (%ID/gram or %ID/organ) ± SEM (standard error mean). Included are also the determined ratios of inflamed muscle to control muscle. The initial and residual radioactivity in the syringe, the tail, and the efficiency of the gamma-counter were taken into account for the actual amount of activity administered to each rat.

The measured weights of whole and sample tissue samples and their respective counts (cpm) were entered into the computer program (designed by Jim Ballinger, Ontario Cancer Institute/Department of Nuclear Medicine, Princess Margaret Hospital, Toronto, Ontario). The program calculated the %ID/g and the % ID/organ by calculating the counts/g or the counts/organ and dividing these by the 1% standard cpm (previously determined). The blood mass was calculated to be 6.5% of the body weight.

Chapter 9

Summary, Conclusions, and Future Work

9.1 Summary and Conclusions

This thesis presented work on two different research projects: (i) the structural study of the NSAID azapropazone and its derivatives, and (ii) the evaluation of amino acid and azapropazone derivatives of EDTA and DTPA as potential MR imaging agents.

Azapropazone

The results of the first project were compiled in **Chapters 3** and **4**. Significant advances that were made in the structural chemistry of azapropazone and its derivatives are:

(1) The structure of azapropazone was determined to be nonplanar, which renders the drug chiral, and contradicts the planar structure proposed in the literature. The nonplanarity was found to be caused by the steric interaction between the exocyclic dimethylamino group and the exocyclic carbonly group of the pyrazolidine ring. In addition, the question as to the protonation site of the molecule was answered. The proton resides at N(6), and the molecule is a zwitterion.

(2) The structures of two derivatives of azapropazone, **II** and **III**, were found to be

different than the proposed structures in the literature. The structure of **II** showed that the pyrazolidine ring of azapropazone opened at N(4), not N(11), when the drug was refluxed with formic acid. The structure of **III** showed that refluxing azapropazone with formic acid and acetic anhydride did not cause the dimethylamino group at C(5) to be replaced by a hydrogen atom as previously proposed. Instead, a carbonyl group replaced the dimethylamino group, and the hydrogen atom replaced the carbonyl group at C(3).

(3)   The photodecomposition product, **IV**, was synthesized and characterized. It is planar, and extremely soluble in a variety of solvents. The energy barrier of rotation of the dimethylamino group around the C(5)-N(5) bond was found to be 48 kJ/mol, which is higher than the barrier of 40 kJ/mol found for azapropazone. The rotation of the dimethylamino group of azapropazone is sterically hindered, while the dimethylamino group of **IV** is subjected to an extensive delocalization of electron density throughout the molecule.

Imaging Agents

⌐   The amino acid and azapropazone derivatives of EDTA and DTPA were complexed with paramagnetic Gd(III) and evaluated as potential MR contrast agents by measuring the relaxivity of each complex. The amino acids used were the benzyl esters of glycine, phenylalanine, and tyrosine. The metal complexes of tyrosine and phyenylalanine derivatives were not as soluble in water as those of glycine and azapropazone. Therefore, their relaxivities were determined in a 50/50 mixture of D_2O and MeOD. The biodistribution and imaging capabilities of the azapropazone

and glycine derivatives of DTPA were evaluated by complexing them to $^{111}In(III)$ and injecting the complexes into rats with induced inflammation in one thigh. The work on the imaging agents is found in **Chapters 5** through **8**. The significant results are as follows:

(1) The relaxivities of most of the Gd(III) complexes indicated that two or three water molecules were coordinated to the metal in the EDTA complexes and one water was coordinated to the metal in the DTPA complexes. This result concurs with relaxivity data of similar compounds presented in the current literature.

(2) The relaxivities of the phenylalanine Gd(III) complexes were two to three times higher than related complexes. The reason for this may be the use of $D_2O/MeOD$ as a solvent, which may have increased the outer sphere contribution of the complex to the T_1 relaxation of the bulk solvent.

(3) The animal studies showed that the azapropazone complex gathered in the heart and lungs after 5 min, and cleared the body renally within the hour. The glycine complex localized in the inflamed thigh in preference to the healthy thigh, and was excreted renally after 5 h.

In conclusion, the phenylalanine and tyrosine complexes would probably not be good MR imaging agents based on their solubilities. Concentrations of up to 0.5 M are needed for MRI. The azapropazone derivative of DTPA shows some promise as a heart and lung imaging agent, and its rapid clearance from the body is encouraging. Furthermore, the glycine derivative of DTPA has definite possibilities as an inflammation-site imaging agent.

9.2 Future Work

The structural results of azapropazone and its derivatives shall be used in modelling experiments with the structures of COX-1 and COX-2. The results should indicate the functional groups of the drug and the receptor that are responsible for inhibiting inflammation. Such an experiment can provide information that can be used to design more potent, and possibly safer, anti-inflammatory drugs.

The work on the imaging agents represents preliminary results to help evaluate their potential success in the diagnostic medical field. Much more work is needed to fully characterize the Gd(III) complexes. X-ray crystal structures would determine the number of water molecules directly coordinated to the metal, as well as the distance between the water protons and the paramagnetic center. In addition, relaxivity measurements determined by the technique of NMR dispersion would give more accurate results than those determined here.

Ultimately, the success of the agents as MR imaging agents must be determined on living "volunteers". This is the best way to determine the ability of the agents to enhance proton relaxation in localized areas in vivo. Before this is done, however, stability measurements of the metal complexes are necessary to determine the potential toxicity of the agents.

References

1. Caldwell, J. *Chemistry and Industry,* **1995**, 176.

2. Wechter, W.J., and Jamali, F., (Ed.'s), *J. Clin. Pharmacol.,* **1992**, *32,* 915.

3. Windholz, M., (Ed.), The Merck Index, 10th ed., Merck & Co. Inc., Rahway, N.J., **1983**, 106.

4. Rainsford, K.D., Azapropazone: Over Two Decades of Clinical Use. K.D. Rainsford (Ed.), Kluwer Academic Publishers, Dordrecht, Holland, **1991**, 3-8.

5. Jahn, U., *Arthritis and Rheumatology,* **1985**, *7,* 21.

6. Jahn, U., Reller, J., and Schatz, F., *Drug Res.,* **1973**, *23,* 660.

7. Klatt, C., and Koss, F.W., *Drug Res.,* **1973**, *23,* 913.

8. Stryer, L., Biochemistry, 3rd ed., W.H. Freeman and co., New York, **1988**, 992.

9. Dewitt, D., and Smith, W.L., *Cell,* **1995**, *83,* 345.

10. Morham, S.G., Langenbach, R., Loftin, C.D., Tiano, H.F., Vouloumanos, N., Jennette, J.C., Mahler, J.F., Kluckman, K.D., Ledford, A., Lee, and C.A., Smithies, O., *Cell,* **1995**, *83,* 473.

11. Rainsford, K.D. Azapropazone: Over Two Decades of Clinical Use. K.D. Rainsford (Ed.), Kluwer Academic Publishers, Dordrecht, Holland, **1991**, 41-52.

12. Picot, D., Loll, P.J., and Garavito, R.M., *Nature,* **1994**, *367,* 243.

13. *Personal communication,* Rainsford, K.D., Sheffield-Hallam University, Sheffield, UK.

14. Jackels, S.C., Pharmaceuticals in Medical Imaging, D.P. Swanson, H.M. Chilton, and J.H. Thrall (Ed.'s), Collier Macmillan Publishers, Toronto, Canada, **1990**, 645-661.

15. Morris, P.G., Nuclear Magnetic Resonance Imaging in Medicine and Biology, Claredon Press, Oxford, **1986**.

16. Leach, M.O., The Physics of Medical Imaging, S. Webb. (Ed.), institute of Physics Publishing, Philadelphia, U.S.A., **1988**, 389-487.

17. Webb, S., and Hill, C.R.,. The Physics of Medical Imaging, S. Webb. (Ed.), institute of Physisc Publishing, Philadelphia, U.S.A., **1988**, 389-487.

18. Parker, D., *Chem. In Brit.*, **1994,** 818.

19. (a) Bloembergen, N.J., *Chem. Phys.*, **1957**, 572. (b) Solomon, I. *Phys. Rev.*, **1955**, *99*, 559.

20. Lauffer, R.B., *Chem. Rev.*, **1987**, *87*, 901.

21. Waysbort, D., and Navon, G., *J. Chem. Phys.*, **1978**, *68*, 3074.

22. Tweedle, M.F., Brittain, H.G., and Eckelman, W.C., Magnetic Resonance Imaging, C.L. Partain (Ed.), W.B. Saunders Co., Philadelphia, U.S.A., **1988**, 793-809.

23. Venkatachalam, M.A., and Rennke, H.G., *Circ. Res.*, **1978**, *43*, 337.

24. Klaassen, C.D., and Watkins, J.B., III, *Pharmacol. Rev.*, **1984**, *36*, 1.

25. Smith, R.D., Loo, J.A., Ogorzalek-Loo, R.R., Busman, M., Udseth, H.R., *Mass Spectrometry Rev.*, **1991**, *10*, 359.

26. Sheldrick, G.M., SHELXTL PLUS, Release 5.03, Siemens Analytical X-ray Instruments, Inc., Madison, Wisconsin, 1994.

27. (a) Jones, P.G., *Chem. Brit.*, **1981**, *17*, 222. (b) Orvig, C., *J. Chem. Educ.*, **1985**, *62*, 84.

28. North, A.C.T., Phillips, D.C., and Matthews, F.S., *Acta Crystallogr., Sect. A: Fundam. Crystallogr.*, **1968**, *24*, 517.

29. Walker, N., and Stuart, D., *Acta Crystallogr., Sect. A: Fundam. Crystallogr.*, **1983**, *39*, 158.

30. Cranswick, L.W.D., Silverton, J., and Bickner, T., *Int. Union Crystallogr. Newsletter*, **1995**, *3(1)*, 6.

31. SAINT, Release 4.05, Siemens Energy and Automation Inc., Madison, Winsconsin, 1996.

32. Sheldrick, G.M. SADABS (Siemens Area Detector Absorption Corrections), 1996.

33. Resolution Pharmaceuticals, Inc., John Thornback, General Manager, Mississauga, Ontario.

34. Walker, F.S., <u>Anti-Inflammatory and Anti-Rheumatic Drugs</u>, Vol. II, CRC Press, Boca Raton, Florida, **1985**, 1-32.

35. Dean, F.M., <u>Azapropazone: Over two Decades of Clinical Use</u>, K.D. Rainsford (Ed.), Kluwere Academic Publishers, Dordrecht, Holland, **1991**, 9-19.

36. Windholz, M., (Ed.), <u>The Merck Index</u>, 10th ed., Merck & Co. Inc., Rahway, N.J., **1983**, 106.

37. Fenner, M., and Mixich, G., *Arzneim. Forsch.*, **1973**, *23*, 667.

38. Fauconnier, T.K.F., Bell, Lock, C.J.L. R.A.,Britten, J.F., and Rainsford, K.D., *Can. J. Chem*, **1991**, *72*, 382.

39. *Personal communication*, Bain, A.D., McMaster University, Hamilton, Ontario.

40. Testa, B., Caron, G., Pagliara, P., and Carrupt, P-A. *Helv. Chim. Acta.*, **1996**, *79*, 1683.

41. (a) Tsai, R.S., Carrupt, P-A., El Yayer, N., Testa, B., Giroud, Y., Andrade, P., Brée, F., and Tillement, G., *Helv. Chim. Acta*, **1993**, *76*, 842. (b) Takacs-Novak, K., Kökôski, J., Podanyi, B., Noszal, B., Tsai, R.S., Lisa, G., Carrupt, B., Testa, B., *Helv. Chim. Acta*, **1995**, *78*, 553.

42. Mixich, G., *Helv. Chim. Acta*, **1968**, *51*, 532.

43. Bergerhoff, G., Kigler, B., Witthauer, C., Hundt, R., and Sievers, R., *Inorganic Crystal Structure Database*, Bonn, Germany, **1992**.

44.   Vargas, F., *J. Photochem. Photobiol. B.: Biol.*, **1993**, *17*, 41.

45.   Data was collected by Victor G. Young, Jr., at the X-Ray Crystallographic Laboratory, the University of Minnesota, Minneapolis, Minnesota.

46.   Bain, A.D., Fauconnier, T.K.F., Bell, R.A., Lock, C.J.L., and Hazendonk, P., submitted to *Can. J. Chem.*

47.   Cotton, F.A., and Wilkinson, G., Advanced Inorganic Chemistry, 5th ed., Wiley interscience, New York, **1988**.

48.   Baxter, A.B., Melnikoff, S., Stites, D.P., and Brasch, R.C., *Invest. Radiol.*, **1991**, *26*, 1035.

49.   Carr, D.H., Brown, J., and Bydder, G.M., *Lancet*, **1984**, *1*, 484.

50.   Gries, H., and Miklautz, H., *Physio. Chem. Phys. And Med. NMR*, **1984**, *16*, 105.

51.   Jenkins, B.G., Lauffer, R.B., *Inorg. Chem.*, **1988**, *27*, 4730.

52.   Aime, S., and Botta, M., *Inorg. Chim. Acta*, **1990**, *177*, 101.

53.   Peters, J., *Inorg. Chem.*, **1988**, *27*, 4686.

54.   Moeller, T., Gmelin Handbuch der anorganischen Chemie: Rare Earth Elements, Part 01., Springer Verlag, Berlin, **1980**.

55.   Koenig, S.H., and Brown, R.D., III, *Magnetic Resonance Annual 1987*, H.Y. Kressel, (Ed.), Raven, New York, **1987**.

56.   (a) Cacheris, W.P., Quay, S.C., and Rocklage, S.M., *Magn. Reson. Imaging*, **1990**, *8*, 467. (b) Quay, S.C., Patent WO 86 02,841; *Chem. Abs.*, **1987**, *106*, 340.

57.   Ehnebom, L., and Pedersen, B.F., Acta Chem. Scand., 1992, 46, 340.

58.   Konings, M.S., Dow, W.C., Love, D.B., Raymond, K.N., Quay, S.C., and Rocklage, S.M., *Inorg. Chem.*, **1990**, *29*, 1488.

59.   Shannon, R.D., *Acta Crystallogr., Sect A*, **1976**, *32*, 751.

60. Bligh, S.W.A., Chowdhury, A., McPartlin, M., and Scowen, I.J., *Polyhedron*, **1995**, *14*, 567.

61. Peters, J.A., Geraldes, C., Urbano, A.M., and Hoefnagel, M.A., *Inorg. Chem.*, **1993**, *32*, 2426.

62. Aime, S., Fasano, M., Paoletti, S., and Terreno, E., Gazz. Chim. Ital., **1995**, *125*, 125.

63. Aime, S., Botta, M., Fasano, M., and terreno, E., *Spectrochimica Acta*, **1993**, *49a*, 1315.

64. Aime, S., Botta, M., Dastrú, Fasano, M., and Panero, M., *Inorg. Chem.*, **1993**, *32*, 2068.

65. Cacheris, W.P., Quay, S.C., and Rocklage, S.M., *Magn. Reson. Imaging*, **1990**, *8*, 467.

66. Normann, P.T., and Hals, P-A., *Proceedings of the 12th Annual Meeting of the Society of Magnetic Resonance in Medicine*, Society of Magnetic Resonance in Mediciine, Berkeley, California, **1993**, 790.

67. Koenig, S.H., and Brown, R.D., III, *Prog. NMR Spectrosc.*, **1990**, *22*, 487.

68. Aime, S., Botta, M., Fasano, M., Paoletti, S., Anelli, P.L., Uggeri, F., and Virtuani, M., *Inorg. Chem.*, **1994**, *33*, 4707.

69. Aime, S., Botta, M., and Ermondi, G., J. Magn. Reson., 1991, 92, 572.

70. Tweedle, M.F., <u>Lanthanide Probes in Life, Chemical and Earth Sciences</u>, J.-G. Bünzli, and G.R.Choppin (Ed.'s), Elsevier, Amsterdam, **1985**, Ch. 5.

71. Anelli, P.L., Calabi, L., De Haën, C., Fedeli, F., Losi, P., Murru, M., and Uggeri, F., *Gazz. Chim. Ital.*, **1996**, *126*, 89.

72. Gries, H., and Miklautz, H., *Physiol. Chem. Phys. Med. NMR*, **1984**, *16*, 105.

73. Chang, C.A., *Invest. Radiol.*, **1993**, *28*, S21.

74. Koenig, S.H., Baglin, C., Brown, R.D., III, and Brewer, C.F., *Magn. Reson. Med.*, **1984**, *1*, 496.

75. Geier, G., Karlen, V., Zelewsky, A.G., *Helv. Chim. Acta*, **1969**, *52*, 1967.

76. Hoard, J.L., Lee. B., and Lind, M.D., *J. Am. Chem. Soc.*, **1965**, *87*, 1612.

77. Weinmann, H.J., Brasch, R.C., Press, R.C., and wesbey, G.E., *Am. J. Roentgenol.*, **1984**, *142*, 619.

78. Yeh, S.M., Meares, C.F., and Goodwin, D.A., *J. Radioanal. Nucl. Chem.*, **1979**, *53*, 327.

79. Koenig, S.H., and Brown, R.D., III, *Magn. Reson. Med.*, **1984**, *1*, 478.

80. Aime, S., Botta, M., and Ermondi, G., *J. Magn. Reson.*, **1991**, *92*, 572.

81. James, T.L., Nuclear Magnetic Resonance in Biochemistry, Academic, New York, **1975**, 39.

82. Washylishen, R.E., NMR Spectroscopy, C. Dybowsky and R.L. Lichter (Ed.'s), Dekker, New York/Basle, **1987**.

83. Navon, G., *Chem. Phys. Lett.*, **1970**, *7*, 390.

84. Templeton, L.K., Templeton, D.H., Zalkin, A., and Ruben, H., *Acta Cryst.*, **1982**, *B38*, 2155.

85. Lauffer, R.B., Vincent, A.C., Padmanabhan, S., Villringer, A., Saini, S., Elmaleh, D.R., and Brady, T.J., *Magn. Reson. Med.*, **1987**, *4*, 582.

86. Lauffer, R.B., and Brady, T.J., *Magn. Reson. Imaging*, **1985**, *3*, 11.

87. Lauffer, R.B., Brady, T.J., Brown, R.D., Baglin, C., and Koenig, S.H., *Magn. Reson. Med.*, **1986**, *3*, 541.

88. Weast, R.C.,(Ed.), The Handbook of Chemistry and Physics, 66th ed., CRC Press, Boca Raton, Florida, **1985**, B-295.

89. Geigy, J.R., Fr. Patent 1 548 888, **1968**; *Chemical Abstracts* 71: 81380, **1969**.

90. Takeshita, K., Shimohara, T., and Maeda, S., *J. Am. Oil Chem. Soc.*, **1982**, *59*, 104.

91. Boxen, I., and Ballinger, J.R., *Curr. Opin. Radiol.* **1991**, *3*, 840.

92. Datz, F.L., Anderson, C.E., and Ahluwalia, R., *J. Nucl. Med.*, **1994**, *35*, 74.

93. Pollak, A., Goodbody, A.E., Ballinger, J.R., Duncan, G.S., Tran, L.L., Dunn-default, R., Meghji, K., Lau, F., Andry, T.W., Boxen, I., and Sumner-Smith, M., *Nucl. Med. Comm.*, **1996**, *17*, 132.

IMAGE EVALUATION
TEST TARGET (QA-3)

1.0 1.1 1.25 1.4 1.6 1.8 2.0 2.2 2.5 2.8 3.2 3.6 4.0 4.5 5.0

150mm

6"
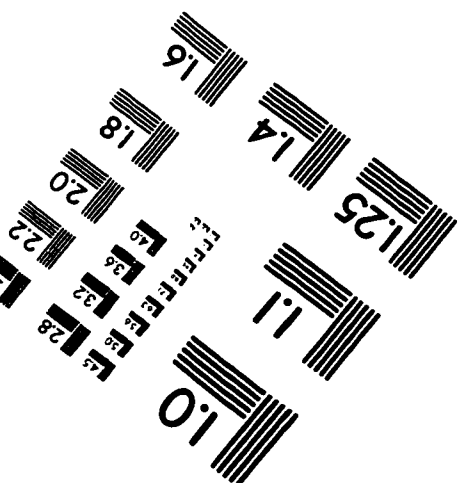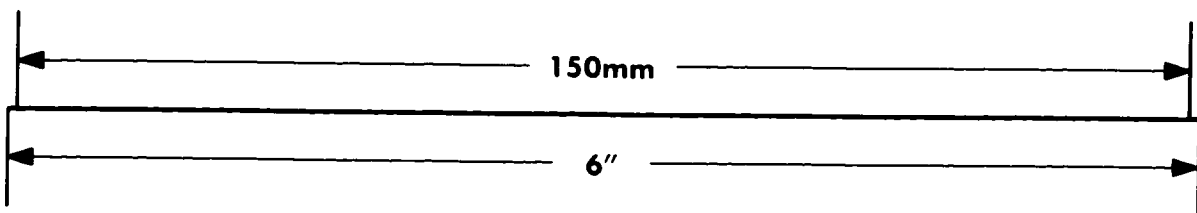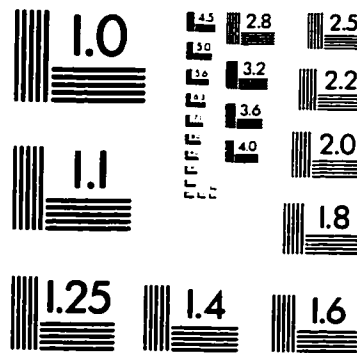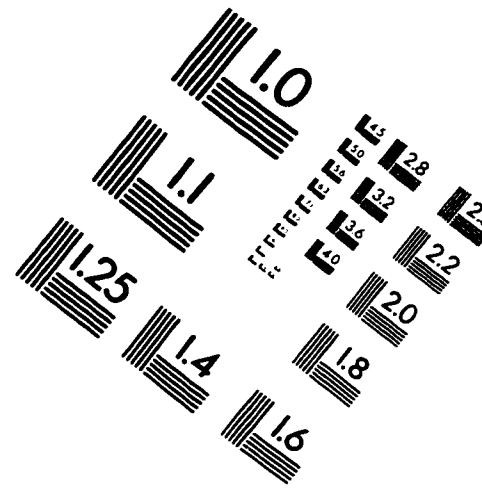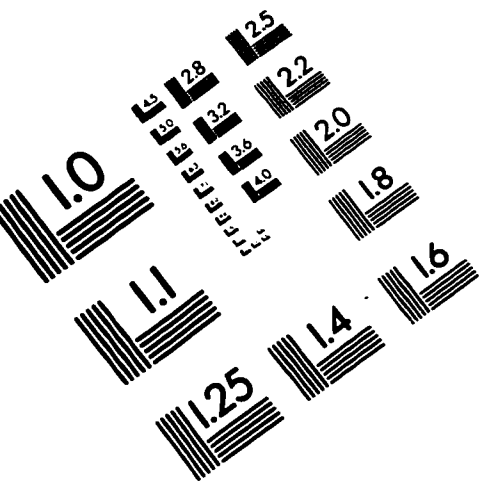
APPLIED IMAGE . Inc
1653 East Main Street
Rochester, NY 14609 USA
Phone: 716/482-0300
Fax: 716/288-5989

© 1993, Applied Image, Inc., All Rights Reserved